This is to certify that the

dissertation entitled

Techniques and Applications of SEM Moire and AFM Moire

presented by

Hua-Tang Chen

has been accepted towards fulfillment
of the requirements for

Ph.D. degree in Materials Science and Engineering

Major professor

Date 02/28/2001

TECHNIQUES AND APPLICATIONS OF SEM MOIRÉ AND AFM MOIRÉ

By

Hua-Tang Chen

A DISSERTATION

Submitted to
Michigan State University
in partial fulfillment of the requirements
for the degree of

DOCTOR OF PHILOSOPHY

Department of Material Science and Mechanics

2001

ABSTRACT

TECHNIQUES AND APPLICATIONS OF SEM MOIRÉ AND AFM MOIRÉ

By

Hua-Tang Chen

The SEM moiré method can obtain deformation measurement and microscopic observation simultaneously. Some drawbacks exist: (1) the requirement of a vacuum environment (2) the reinforcement effect of grating material, and (3) the multiple steps of grating fabrication. To reduce these drawbacks several new techniques were developed. The AFM moiré method allows deformation measurement in a normal laboratory environment. A new grating technique, direct electron beam deposition, was developed. This technique deposits a carbonaceous grating on a specimen surface. The thickness of this carbonaceous grating is reduced to 8 nm instead of 100 nm of PMMA grating, minimizing the reinforcement effect. A total of six SEM moiré methods were produced by combining three viewing techniques with two grating fabrication techniques. The sensitivity of the SEM moiré method is improved from 0.2% to 0.02% or even higher if a higher frequency of grating is used. The SEM moiré method was applied to the deformation measurement of carbon fiber reinforced composites. Another application is the local strain measurement of a two-phase polymer under the stress relaxation experiment. The interface shifting is observed and the local strain is measured by the SEM moiré method simultaneously. Accordingly, an analytical solution of dynamic

mechanical properties based on the rule of mixtures was derived. The dynamic mechanical analysis (DMA) was conducted on two-phase polymer specimens with different volume fractions in parallel and serial loading configurations. It seems that the analytical solution does not predict the experimental data of a two-phase polymer in serial loading configuration. On the other hand, the dynamic mechanical properties of specimens in parallel loading configuration match very well with the analytical solution.

謹以此書
獻給
敬愛的阿公與阿媽
陳福春 先生
陳楊敏 女士
以及
父親與母親
陳武雄 先生
黃秀梅 女士

ACKNOWLEDGMENTS

I wish to express my deepest appreciation to Dr. André Y.-J. Lee for his constant guidance, encouragement, and patience during the course of my graduate study at Michigan State University. Heart felt gratitude goes to Dr. Dahsin Liu for his unlimited stimuli to my professional growth in my field through the many academic challenges he posed to me. Without his recognition of some critical issues in my research, this work could not have been completed. I would like to express my greatest respect toward Dr. K. N. Subramanian for his valuable suggestions in many aspects of my research work. Deeply appreciation to Dr. Stanley Flegler for showing me the beauty of the scanning electron microscope and the valuable discussion on the topics related to the scanning electron microscope. Special thanks go to my friends at Michigan State University for their helpful discussion and inspiration. Appreciation is expressed to Dr. R. D. Bradshaw and Dr. L.C. Brinson at Northwest University for the use of their curve-fitting computer program.

Thanks to Michigan Research Excellence Fund, National Institute of Standards and Technology, Manufacturing Research Consortium, and Semiconductor Research Center for their financial support during my graduate study at Michigan State University. Deeply grateful goes to the Graduate School for awarding me the Dissertation Completion Fellowship.

Last but certain not least, I wish to thank my family for their continuous support and encouragement of pursuing my dream and for having faith in me of completing my dissertation.

TABLE OF CONTENTS

CHAPTER 4

CHAPTER 5

LIST OF TABLES

LIST OF FIGURES

Chapter 1

INTRODUCTION

1.1 METHODS FOR MICROSCOPIC DEFORMATION MEASUREMENT

Deformation measurements of a small specimen or a small area of large specimens are required in the study of microelectronics and composites. Therefore, the methods for whole field microscopic deformation measurement have been under intensive development (grid methods, x-ray diffraction methods, digital image correlation method, microscopic moiré interferometry, speckle interferometry with electron microscopy). These methods are briefly introduced. Their applications and sensitivity are discussed as well.

1.1.1 Grid Method

The grid method relies on the measurement of the distance between small dots on the specimen surface under different loads to determine the deformation of the specimen. An array of small dots is deposited on the specimen before deformation. Then, a series of images is taken before and after loading. These images are analyzed by an image processing system. The horizontal and vertical displacement field of the specimen can be calculated simultaneously by measuring the spacing between dots in each image and correlating the spacing measurement from those images.

Sirkis and Lim[1] developed the automated grid method consisting of a charged coupled device (CCD) video camera and a personal-computer-based image-processing system to measure the displacement and strain of a perforated uniaxial tension aluminum specimen. The sensitivity of their measurement to in-plane and out-of-plane motion is

1.0 and 3.33 microstrain respectively and their accuracy is ± 120 microstrain. The results from this method have a reasonable agreement with the geometric moiré method.

Tian and coworkers[2] used the electron beam of the scanning electron microscope to produce a square array of small dots on the rubber-modified epoxy. The deformation ahead of the crack tip can be measured using an image processing system to correlate the spacing between dots in the pictures and the strain magnitude of the specimen. The strain resolution in their study was 1%. They predicted achieving 0.2% with standard image analysis techniques. Further improvements for spatial resolution are able to achieve 0.5 μm with further spatial refinement of small dots.

The grid method does not require special training to interpret the results. However, it requires a fast image processing system to achieve a real time measurement.

1.1.2 X-ray Methods

X-ray diffraction imaging is used to map deformation in crystals. In deformed crystals, the combined effect of dilation and tilt allows only a small region of the crystal to diffract a given wavelength for a particular sample orientation. From the diffraction images before and after loading, the deformation field can be obtained. There are many x-ray diffraction methods for mapping deformation fields, such as section topographic strain mapping and peak shift/broadening measurement[3].

X-ray diffraction imaging has been used to examine GaAs wafer perfection[4], to investigate the distribution of dilational and tilt components of the plastic deformation around the large β-NbH precipitates in Nb crystals [5] and to characterize cleavage of Mo and Nb [6]. Stock and coworkers are using this technique to map the elastic strain fields around a notch in a silicon crystal that has been deformed by bending[7].

The other x-ray method is x-ray tomographic microscopy (XTM) that can image the damage area in crystals. It is based on the different absorbability of x-ray in the materials. The x-ray absorption of materials depends on their elemental composition, their density, the length of absorbing materials traversed by the beam, and the x-ray wavelength(s). Therefore, the differences either in density or in phases can be determined by mapping differences in x-ray transmission[3].

A unidirectional, continuous fiber SiC/Al composite and SiC/Si3N4 composites [7] and bone and dental enamel[8-10] have been studied using XTM.

Both x-ray methods are suitable for mapping with spatial resolution approaching 1 μm and a field-of-view-millimeters in extent. Sensitivity and resolution of both methods depend on how parallel the x-ray beams are, and the highest precision is obtained if synchrotron radiation is used. In single crystal samples, strains as low as 1 microstrain can be measured by these x-ray diffraction methods. Strain in the 0.01% to 1% ranges of polycrystalline samples can be measured using microbeam diffraction.

X-ray diffraction methods for deformation mapping and x-ray tomographic microscopy for damage mapping are powerful methods for measuring the deformation field and detecting damages inside the materials. However, the collection of data in these methods is time consuming and the instruments required are expensive. In addition the x-ray diffraction method will not be able to measure the deformation of amorphous materials that did not form x-ray diffraction patterns.

1.1.3 Digital Image Correlation (DIC) Method

The measurement of micro-displacement can be made by the digital image correlation method called DISMAP[11]. This method measures the difference of two captured digital images of the same field under different loading by using an imaging processing system. DIC has been used to study the crack growth of various materials in different loading conditions by measuring the crack opening displacement (COD)[12].

This method holds the advantages of the flexibility in designation of the region and the density of measurement. The spatial resolution of this technique depends on the magnification of the photographs and the choice of grid sizes used for measurement. Measurements cannot be made closer than each 1 mm. Thus, for example, from a 4000x photograph it might be possible to measure displacement each 0.25 μm. However, for higher magnification the alignment of two photographs, such as pre-loading and post loading, becomes difficult causing errors.

1.1.4 Microscopic Moiré Interferometry

Based on the concept of moiré interferometry the immersion interferometer was developed to observe the specimen features and to increase the sensitivity of moiré interferometry simultaneously by Han and Post[13]. The light is introduced into a refractive material to decrease its wavelength, which increases the frequency of the virtual reference grating. This reference grating interferes with the specimen grating and forms moiré fringe patterns which contain displacement information of the specimen. With the aid of microscope, the small features on specimen surface also can be identified at the same time with the moiré fringe patterns.

The microscopic moiré interferometry is used to verify the validity of numerical models for microelectronics packaging design[14]. The thermal deformation for flip-chip packages is characterized by this method as well[15].

The sensitivity of moiré interferometry is limited by the frequency of virtual reference grating formed by two coherent laser beams. One way of increasing the frequency of virtual reference grating is to reduce the wavelength of the laser by introducing the laser through a refractive medium. For example, the virtual reference grating is increased from 3890 lines per millimeter to 5910 lines per millimeter by passing a green argon laser (its wavelength is 514 nm) through an optical glass (BK7 with refractive index 1.52) to reduce its wavelength to 338 nm.

1.1.5 Speckle Interferometry with Electron Microscopy (SIEM)

To increase the sensitivity of speckle interferometry, Chiang[17] first introduced the concept of SIEM in 1982. The submicron particles can be created onto a specimen surface by either a vacuum or physical/chemical vapor deposition processes or other surface techniques. The several images of speckle patterns are taken under SEM before and afternoon deformation. Then, an optical filter is used to these SEM images to yield fringes of low contrast and high random noise. According to these fringes, the deformation field can be extracted by trained personal using digital image processing technique.

Chiang and co-workers[18] have developed SIEM combining speckle photography, electron microscopy and digital image processing to measure the localized deformation. They have applied the SIEM to determine the interphase mechanical properties of composites[19], to monitor the mechanical behavior of a single fiber[20], to study the near field phenomenon at the bimaterial interfacial crack tip[21,22], to investigate the effect of adhesive thickness on adhesion[23], and to characterize the deformation at kink band tip in fibrous composite[24].

1.2 STATEMENT OF PROBLEM

A Scanning Electron Microscope (SEM) moiré method for microscopic measurements based on electron beam lithography and a scanning electron microscope has been well developed. Although it has been a reliable method, some drawbacks exist: (1) requirement of a vacuum environment for testing; (2) reinforcement effects induced by lithographic grating, (3) multiple procedures of lithographic grating and (4) low sensitivity of deformation measurement.

SEM moiré method requires a vacuum environment to measure microscopic displacement. A test in a normal laboratory environment will be able to simulate the mechanical response of a material in real application. A friendly testing environment for high sensitivity measurement needs to be developed. For example, the Scanning Probe Microscope (SPM) is currently used for high resolution imaging under normal laboratory environment.

New grating techniques need to be introduced to reduce reinforcement effects induced by lithographic grating. New techniques should be able to reduce reinforcement effects significantly by changing to low modulus materials or reducing the thickness of grating layer without compromising the quality of moiré fringes.

Simplifying the grating fabrication procedures will be helpful while using SEM moiré. The most common technique to cast a specimen grating is electron beam lithography which is well documented in the literature. It takes many steps to cast a grating on specimen.

Currently, the SEM moiré method is based on the specimen grating cast by electron beam lithography and the reference grating generated by viewing scanner of an

SEM. The viewing scanner has a lower scanning rate of 500 lines/mm, which yields the minimum strain of 0.2% for the SEM moiré method. This strain is quite high for many engineering materials. Therefore, new techniques need to be introduced to increase the sensitivity of SEM moiré method.

1.3 ORGANIZATION OF DISSERTATION

In this study, several micro-displacement measurement methods have reviewed in Chapter 1. The SEM moiré method is investigated in Chapter 2. To measure microdisplacement in normal laboratory environment the atomic force microscope (AFM) moiré method is developed in chapter 3. A new grating technique has been introduced in chapter 4 to simplify the grating fabrication procedures and reduce the reinforcement effects. There are several new methods to increase the sensitivity of SEM moiré, which are stated in Chapter 5. Applications of the SEM moiré method to carbon fiber reinforced composites and on the local displacement measurement of two-phase polymers are demonstrated in Chapter 6. Chapter 7 concludes the development and applications of these new grating techniques and SEM moiré methods.

Chapter 2

MOIRÉ IN SCANNING ELECTRON MICROSCOPE

2.1 INTRODUCTION

After its introduction by Well and Shepard in 1948[25], the moiré method for displacement and strain analysis had been improved by introducing new technologies in both grating production and measurement setup. The geometric moiré method had been studied intensively from 1940s to the 1970s. In the 1980s, the most significant development of moiré method was in moiré interferometry where diffraction gratings were produced by interference of two plane beams from a coherent light source, such as a laser[26,27]. The major advance for moiré interferometry was the improvement of the sensitivity due to the increase of the grating frequency from about 50 lines/mm for geometric moiré to 4,800 lines/mm.

However, further increases in the sensitivity of moiré interferometry were limited by the wavelength of light. Kishimoto *et. al.*[28] first introduced the SEM moiré method, which was able to achieve higher sensitivity, to demonstrate its application on the study of microdeformation in 1991. In their studies, the moiré fringe patterns were produced by the interference between the grating on a specimen and the scanning lines of a conventional scanning electron microscope (SEM). Hence, the SEM moiré method shared the same fundamentals of fringe formation with the geometric moiré. The principle of the moiré fringe formation was similar to the fringes of video-scanning moiré introduced by Morimoto et. al.[29] in 1984.

In 1993, Dally and Read[30] achieved a high frequency of 10,000 lines/mm by using high-resolution e-beam lithography. They demonstrated the method for making high frequency gratings[30] and the application of electron-beam moiré method in micromechanics[31,32]. Moreover, they presented a mathematical model to explain the formation of moiré fringe patterns observed at different magnifications[33]. The formulae for analyzing moiré fringe patterns are also available in their study.

To make the SEM moiré method more accessible, an alternative technique to fabricate specimen gratings was developed by using a conventional SEM without having an electron beam lithography facility. Therefore, the SEM parameters (beam current, exposure time, and beam size etc.) were optimized to fabricate specimen gratings. These specimen gratings were able to form moiré fringes in conventional SEM to achieve a real time deformation measurement and a microscopic observation on a specimen surface simultaneously. The discussion included the quality of specimen grating, which affects the quality of the moiré fringe pattern, as well as several restrictions of the SEM moiré method.

2.2 GRATING TECHNIQUE

There are several ways to deposit a high frequency of gratings on specimen surfaces, for example, photolithography, e-beam lithography, and x-ray lithography etc. Usually, a thin film of polymethylmethacrylate (PMMA) was deposited on the specimen by spin coating. This PMMA thin film reduced its molecular weight due to the scission of its main chain by the absorption of energy from photons, electrons, or x-rays. The exposed PMMA thin film, which contained a lower molecular weight of PMMA, was dissolved in a suitable solvent while the unexposed one remained intact and a grating was deposited on the specimen.

In this study, the e-beam lithography was used to deposit a high frequency of grating on the target specimen because both photolithography and x-ray lithography required a grating mask, which was fabricated by e-beam lithography. In e-beam lithography, the electron energy absorbed by the PMMA thin film was from incident electrons, secondary electrons and backscattered electrons, which were generated by the filament, substrate, and conductive layer such as aluminum or gold. The etching rate was controlled by electron energy and etching boundaries were determined by contours of electron energy deposition, which resulted in the different grade of degradation.

Everheart et. al.[34] had demonstrated the electron interaction volume in PMMA for acceleration voltage of 20 keV. The etched structures allow direct visualization of electron penetration and the interaction volume in a low atomic number matrix. The increase of electron energy or etching time increased the width of etched lines, especially for the undercut, which was detrimental to achieving a high frequency of gratings. Hence, to control the desired depth and width of etched lines, these parameters needed to be optimized for each particular substrate: electron energy, electron dosage, the developing time in the solvent, and concentration of the solvent.

To optimize these parameters for grating fabrication, a brass disk, aluminum alloy A5083 strips, rubber-toughened epoxy, and glass/epoxy composites were used as substrates and a PMMA solution (0.4999g of PMMA and 25 ml of toluene) was prepared for spin coating. The PMMA photoresist has a relative molecular weight of 950,000. The rubber-toughened epoxy was a liquid diglycidyl ether of bisphenol A (DGEBA)-based epoxy resin (DER332, Dow Chemical, USA) cured with a diamine-terminated poly(propylene oxide), JEFFAMINE D230 (Huntsman, USA). The rubber particles used for toughening were carboxyl-terminated random copolymer of butadiene and acrylonitrile, Hycar CTBN 1300x8 and 1300x13 (Shell Chemical). The composite material was $[0°/90°]_s$ laminated glass/epoxy composite. Figure 2.1 shows the steps of fabricating gratings schematically. The surfaces of specimens were ground smooth and flat using a series of water-lubricated abrasive-coated paper and the final polish was ended with 0.05 μm alumina particles. After specimens were polished, the surfaces of specimens were cleaned with distilled water in an ultrasonic cleaner for 30 minutes and then were blown dry with clean air.

The specimens were then kept in the desiccator before the PMMA thin film was spun on the specimens at a speed of 3000 rpm for 30 seconds. The electrically non-conductive specimens were coated with a thin layer of Al or Au prior to spin coating. Then the metal and polymer specimens were placed in the vacuum oven for 60 minutes at 160°C and 100°C respectively to remove residual solvent. This application was not performed in a class-100 clean room, which was usually used by the others [30].

Right after the PMMA thin film was coated on the specimen, a single photo scan rate (1250 lines/frame) in CamScan 44FE SEM was used to fabricate gratings on the specimens. SEM was set up with an acceleration voltage of 20 keV, an aperture of 50 μm, a spot size of either 9 or 11, and a working distance of 20 mm. The grating fabrication was performed at different magnifications in order to have a desired frequency of gratings on the specimen. The following equation was used to calculate the needed magnification to fabricate the desired frequency of gratings.

$$f_g = \frac{\text{number of scanning lines per frame}}{\text{hight of scanning area}} M \,, \tag{2.1}$$

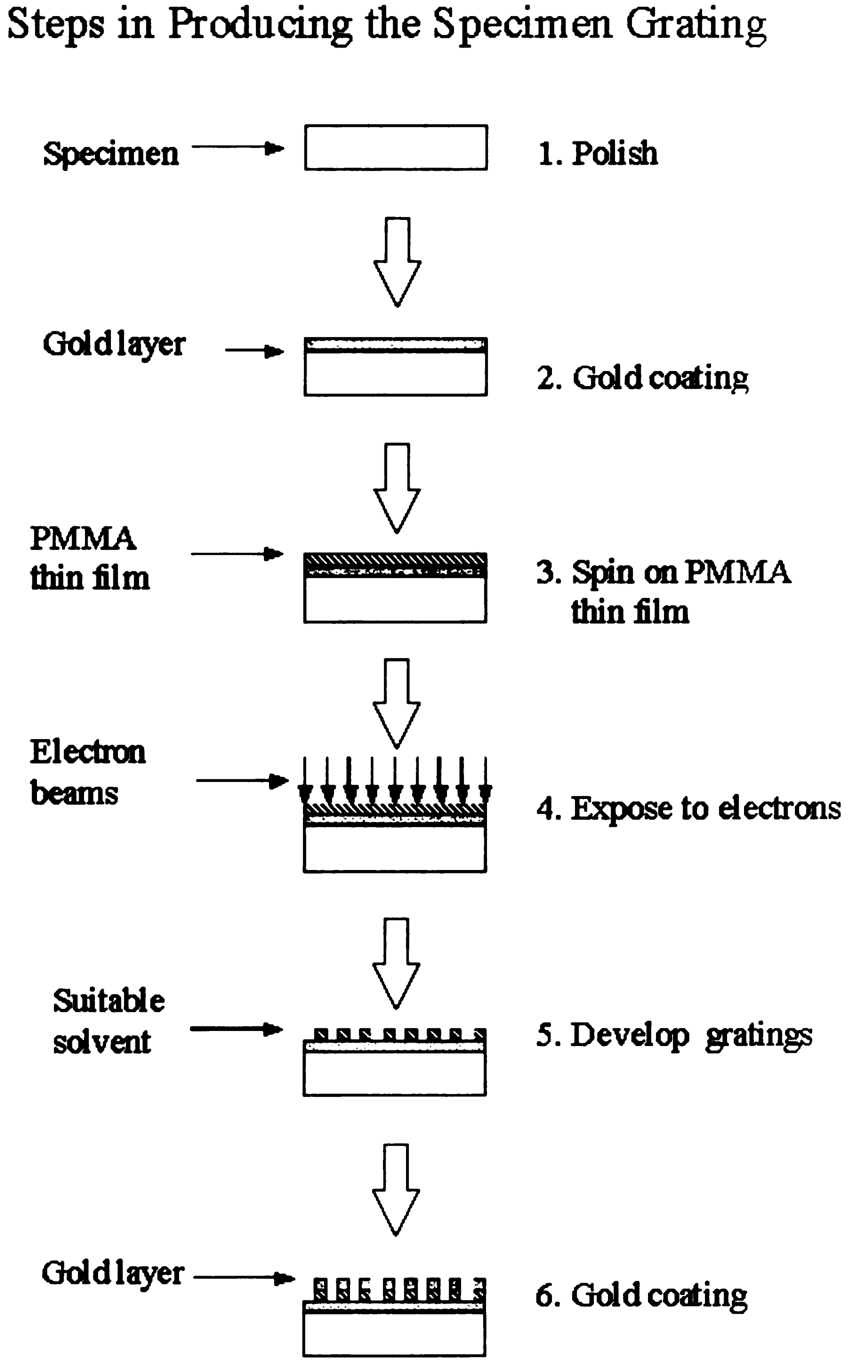

Figure 2.1 Specimen grating preparation procedures.

where M was magnification factor and f_g was desired frequency of specimen grating. The single photo scanning mode in CamScan was 1250 lines per frame with a scanning area of 120 mm x 90 mm at 1:1. Table 2.1 listed the grating areas with their frequency and magnification factor of scanning. The condenser lenses, astigmatism, centering of the aperture and focus were carefully adjusted and tuned in order to obtain the size of the electron beam as small as possible at the position nearby the desired grating area. Then the desired exposure area was positioned under the electron beam, which was blocking by a beam stopper. Four different exposure times were applied to PMMA thin film: 21,42, 85, 171 seconds.

After the exposure, the specimens were developed in a solution consisting of three parts (by volume) of isopropyl alcohol and one part of methyl isobutyl ketone for 40 seconds. The specimen was immediately rinsed in isopropyl alcohol for 20 seconds followed by a second rinse in distilled water for 30 seconds. Next, the specimen was blown dry with clean air. A thin gold layer was coated on top and side of the specimens later to prevent charging problems as well as damaging of the gratings while viewing the specimens in SEM.

Figure 2.2 shows some SEM images of successful gratings that were deposited on the specimens. The linewidth of grating was controlled mainly by beam current and exposure time, assuming the same acceleration voltage and the smallest probe size. The following equation was usually used to calculate the necessary electron dosage to fabricate the desired grating linewidth.

$$D_L = {}^{i_B * t}\!/_{cc}, \qquad (2.2)$$

where D_L was electron line dosage (nC/cm), i_B was beam current (nA), t was total

Table 2.1 Comparison of grating production and fringe formation.

Grating Production (photograph scanner)				Moiré Fringe Formation (monitor viewing)		
Frequency (lines/mm)	Scanning Rate (lines/frame)	Magnification Factor.	Grating Area (μm^2)	Magnification Factor.	Viewing Rate (lines/frame)	Imaging Area (μm^2)
2500	1250	180x	666x500	450x	500	268x200
3750	1250	270x	444x333	675x	500	178x133
5000	1250	360x	333x250	900x	500	133x100
6250	1250	630x	191x143	1575x	500	76x57
10,000	1250	720x	168x125	1800x	500	68x50
20,000	1250	1440x	83x63	3600x	500	33x25

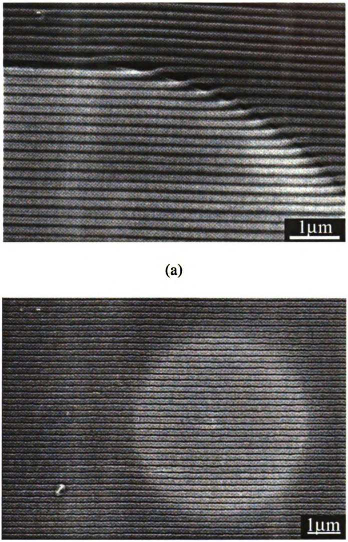

(a)

(b)

Figure 2.2 Two successful lithographic gratings were deposited on (a) Glass/Epoxy composite (b) Glass beads/Polyimide composite.

exposure time (seconds) and 'cc' was total distance of scanning line. Table 2.2 lists the etched width of grating lines associated with their exposure conditions on different substrates. The plot relating electron dosage and etched width of grating line is given in Figure 2.3.

2.3 MOIRÉ FRINGES IN SEM

Figure 2.4 shows the principle of the formation of moiré fringe in an SEM. Three types of moiré fringes (natural, multiplied, and divided moiré fringes) were observed in an SEM. Read and Dally[33] used Fourier series to describe the SEM raster scan lines, the specimen gratings, and the moiré fringes. Their results explained the observation of these three types of moiré fringes in SEM.

The specimen containing gratings was examined in an SEM. The gratings were easily identified at high magnification, and their pitches were measured from the width of the trenches and ridges. The moiré fringes were observed in an SEM when there was a frequency mismatch and/or rotation between the scan raster and the specimen grating. Using the following equation, the magnification factor, *M*, for observing natural moiré fringes was calculated and the results are listed in Table 2.1.

$$M = \frac{f_g * \text{hight of scanning area at } 1:1}{\text{scanning lines per frame}} \tag{2.3}$$

where the TV scanning rate for imaging mode is 500 lines per frame in CamScan and the height of scanning area at 1:1 is 90 mm. There are always carrier fringes in SEM moiré because the discrete magnification of an SEM dose not exactly match the frequency of specimen grating with that of the scan raster.

Table 2.2 Trench width and exposure conditions on different substrates

Substrate	Acceleration Voltage (keV)	Conductive Coating	Mag. Factor	Exposure Time (seconds)	Beam Current (nA)	Line Dosage (nC/cm)	Trench Width (nm)
Brass	25	None	180	42	NA	NA	90
			180	21			60
			180	85			203
Aluminum	25	None	180	21	NA	NA	150
			90	21			85
			90	42			161
			180	21			150
			180	85			54
Epoxy	20	Al	360	21	1.4	0.706	70
			180	85	1.4	1.428	126
			200	85	1.4	1.587	139
			360	21	1.3	0.655	54
Single carbon fiber/Epoxy	20	Al	180	85	1.0	1.020	51
Single glass fiber/Epoxy	20	Al	360	21	1.0	0.504	39
			180	85	0.8	0.816	53
			180	85	1.0	1.020	96
			540	21	1.0	0.756	47
		Au	450	21	1.0	0.630	45
Glass beads /Polyamide	20	Al	180	85	0.8	0.816	113
			360	21	0.8	0.403	70
			200	85	0.8	0.907	89
Rubber particles /Epoxy	20	Al	720	2	0.6	0.144	29
			720	4	0.6	0.288	53
			720	6	0.6	0.432	70
			720	8	0.6	0.576	100
			720	6	0.6	0.432	89
			720	10	0.6	0.720	146
			720	12	0.6	0.864	125
			720	14	0.6	1.008	130
			720	16	0.6	1.152	111
			720	18	0.6	1.296	150
Glass/Epoxy	20	Al	210	85	1.7	1.964	166
			360	21	1.7	0.832	71
			250	85	1.7	2.338	176
			270	85	1.7	2.525	123
			180	85	1.7	1.683	150

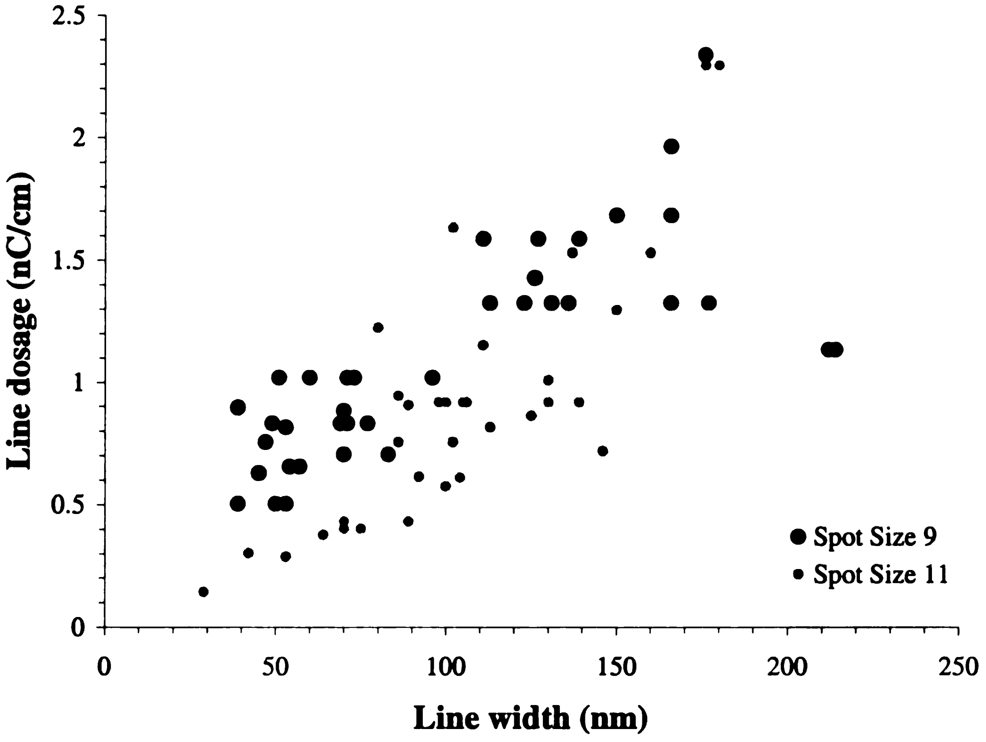

Figure 2.3 Relationship between electron dosage and line width of grating at different spot size modes.

Aligned PMMA gratings with fixed scanning electron beam

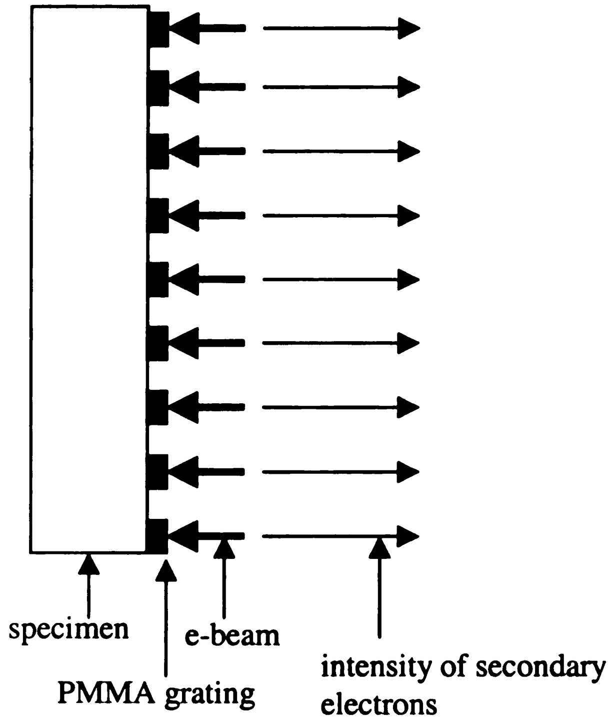

Uniformly deformed specimen with fixed scanning electron beam

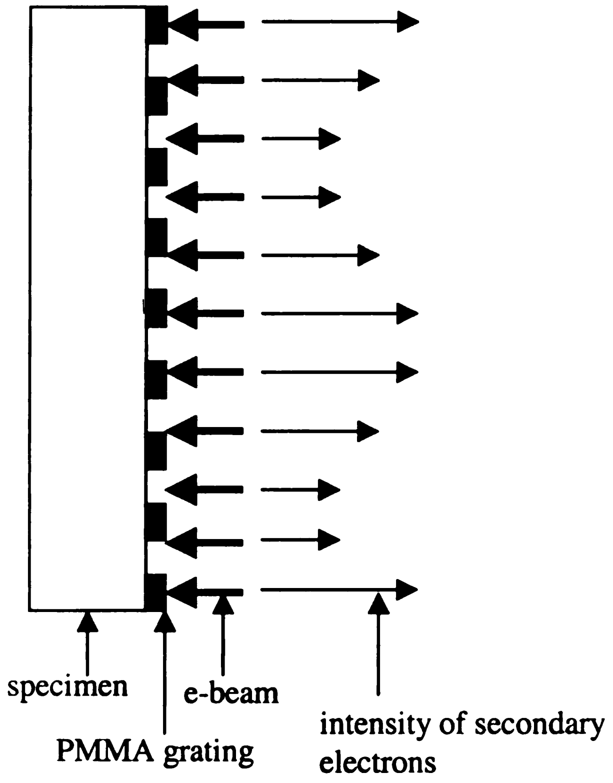

Figure 2.4 The principle of the formation of moiré fringes under SEM

2.4 VERIFICATION

The analysis of the moiré fringe patterns from geometric moiré had been well established. These techniques were also applicable to the moiré fringe patterns observed from SEM moiré. According to the geometry of moiré fringes shown in Figure 2.5, the rotation angle and model grating pitch of a specimen were calculated by the following equations[35]:

$$\tan\theta = \frac{\sin\phi}{\frac{\delta}{p} + \cos\phi}, \text{ and} \tag{2.4}$$

$$p' = \frac{\delta}{\sqrt{1 + \left(\frac{\delta}{p}\right)^2 + 2\left(\frac{\delta}{p}\right)\cos\phi}}, \tag{2.5}$$

where p is the master pitch or raster pitch in the SEM and p' is the specimen grating pitch, or model pitch. The angle θ is defined as the acute angle at any point and in any given state of deformation measured from the fixed master grating lines to the model grating lines. The fringe angle from the fixed master grating lines to a fringe at a point measured in the same direction as θ is designated as ϕ and may be either acute or obtuse. δ is the normal fringe spacing.

The strain at any point is represented by[35]

$$u = N * p, \text{ and} \tag{2.6}$$

$$\varepsilon_x = \frac{\partial u}{\partial x} = \frac{\partial(N * p)}{\partial x} = p\frac{\partial N}{\partial x}, \tag{2.7}$$

where u is the displacement in x direction, N is the fringe number, p is the raster pitch in the SEM, and ε_x is the strain in x direction. Cloud[36] shows a conceptual procedure of moiré strain analysis.

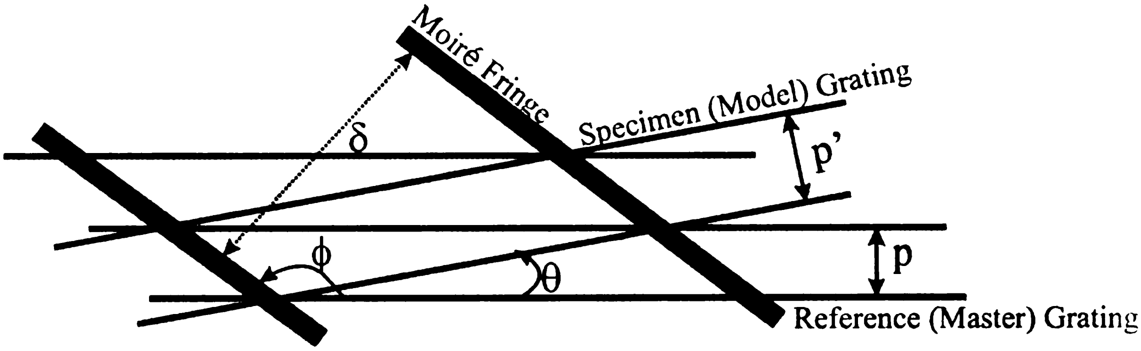

Figure 2.5 Geometry of moiré fringes

To demonstrate the feasibility of SEM moiré to measure deformation, an aluminum strip with a grating of 2558 lines/mm was rotated by small angles with respect to the scanning direction. The moiré fringe patterns associated with different rotation angles of the specimen were recorded and are shown in Figure 2.6. The coordinates of the center of the imaging area after each rotation were recorded as well.

The frequency of moiré fringes and their angles with respect to the scan direction were measured from moiré fringe patterns. By Equation 2.4 the angles between the scan direction and the specimen grating were obtained. On the other hand, based on the coordinates of the center of the image area, the rotation angles were obtained by the following formula.

$$\cos\theta = \frac{\vec{a} \bullet \vec{b}}{|a||b|} \tag{2.8}$$

where a and b were two vectors from the origin to two different coordinates. Table 2.3 listed the calculated results from the coordinate method and the SEM moiré method. The comparisons of these two methods are shown in Figure 2.7. Rotation angles from the coordinate method and the SEM moiré method show 0.14° difference in average.

2.5 DISCUSSION

A. Grating Materials

In this study, a nonconductive photoresist, PMMA, was used for grating fabrication. However, some conductive metal could be another choice as grating material. Attwood and Hazzledine[37] deposited a gold grid pattern consisting of gold lines 0.3 μm wide spaced at 10 μm intervals. The advantage of using metal as a grating

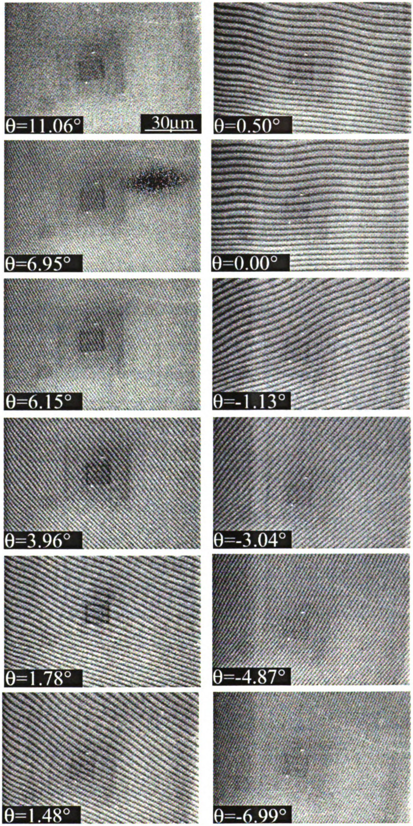

Figure 2.6 SEM moiré fringe patterns with different rotation angles.

Table 2.3 Results of rotation angle calculated from the coordinate method and the SEM moiré method.

Rotation Angle (stage)	Coordinate Method (Degree)	R (mm)	x (mm)	y (mm)	Master Pitch (nm)	Fringe Angle (Degree)	Fringe Pitch (nm)	SEM Moiré (Degree)
11.0	6.95	9.1706	6.1866	6.7695	183.67	119.5	1428.57	6.81
10.0	6.15	9.1713	6.2815	6.6825	183.67	122.0	1578.96	6.00
7.5	3.96	9.1739	6.5332	6.4403	183.67	134.0	2142.84	3.75
5.0	1.48	9.1651	6.7996	6.1453	183.67	161.5	3055.58	1.16
5.0	1.78	9.1666	6.7680	6.1823	183.67	155.0	3157.86	1.49
3.0	0.50	9.1654	6.9042	6.0280	183.67	173.5	3618.99	0.35
2.5	0.00	9.1651	6.9561	5.9676	183.67	179.5	3666.63	0.03
1.0	1.13	9.1672	7.0736	5.8311	183.67	161.5	3365.08	1.05
0.0	3.04	9.1675	7.2649	5.5915	183.67	137.5	2555.58	2.94
-2.5	4.87	9.1738	7.4450	5.3601	183.67	125.0	1904.76	4.78
-5.0	6.99	9.1820	7.6450	5.0856	183.67	117.0	1418.44	6.99

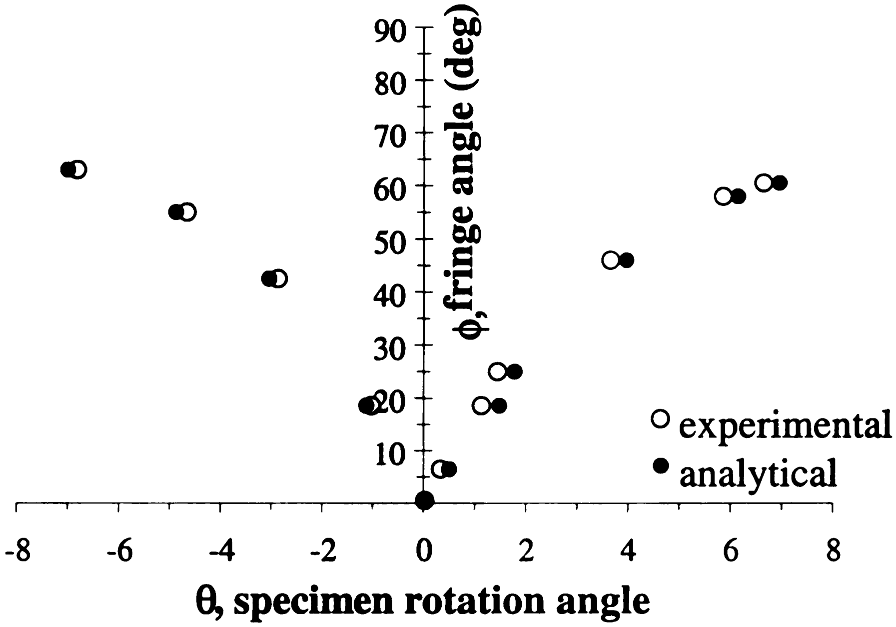

Figure 2.7 Comparison between analytical calculations and experimental measurements.

material is that the testing temperature will not be limited by the melting temperature of PMMA, especially for thermomechanical test.

B. Quality of Specimen Grating

The quality of fabricated specimen grating depends on (1) the roughness and cleanness of specimen surface, (2) the thickness of PMMA thin film and the width of its molecular weight distribution, (3) the exposure and energy of electrons, and (4) the conductive coatings such as Au or Al. These variations affect grating deposition, the width of the trench, and the aspect ratio of specimen grating.

a. Contaminated surface

Surfaces of the specimens were prepared by polishing with 0.05 μm of alumina paste. They were then cleaned with the use of ultrasonic cleaner with a distilled water bath. The cleaned specimens were stored in a desiccator before use. If these steps were not exercised carefully, there might be scratches, dusts, or grease on the specimen surface, which affected the quality of specimen gratings as shown in Figure 2.8 and Figure 2.9. In addition, while containing different hardness of components, the specimen usually had an uneven surface after being polished. This uneven surface could cause a non-uniform coating of PMMA thin film, resulting in an useless specimen grating for future application as shown in Figures 2.10(a) and (b).

b. PMMA thin film

The thickness of PMMA layer could affect the aspect ratio of gratings, then the quality of moiré fringes: the higher the aspect ratio of gratings, the higher contrast of moiré fringes, but the lower image quality of substrate. Figures 2.11(a)-(c) show the effect of thickness on the image quality of substrate. However, as thickness increased,

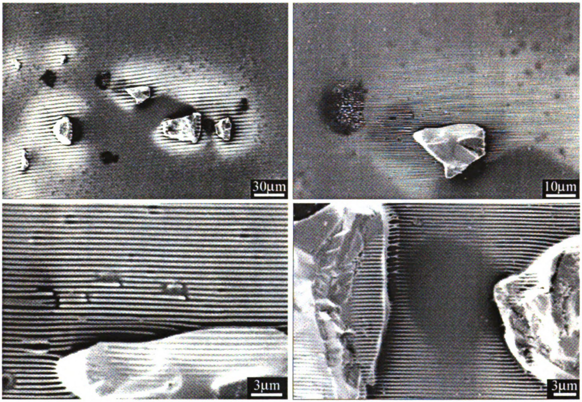

Figure 2.8 The gratings were partially deposited on specimen surface because of the non-uniform PMMA coating.

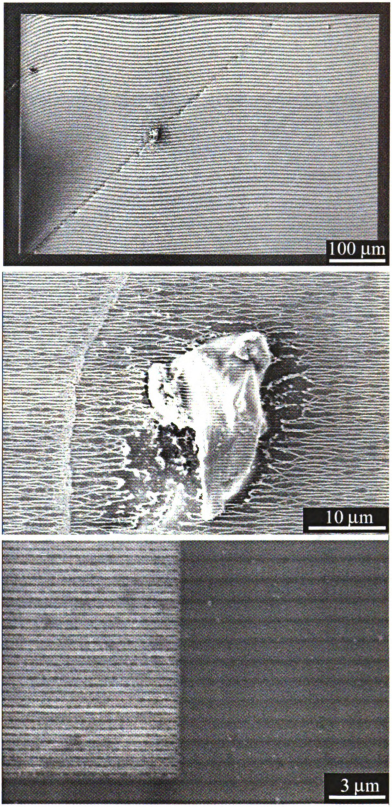

Figure 2.9 Contaminated specimen surfaces resulted in low quality of PMMA gratings and moiré fringe patterns. Carbonaceous gratings were deposited on specimen surfaces as well.

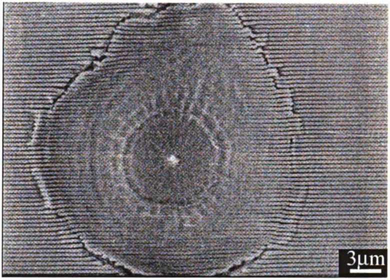

(a)

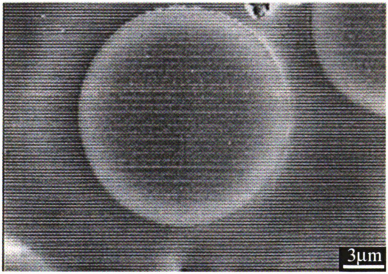

(b)

Figure 2.10 (a) and (b) show no grating at the center of either rubber particle or glass fiber because the specimen surfaces were uneven after polishing.

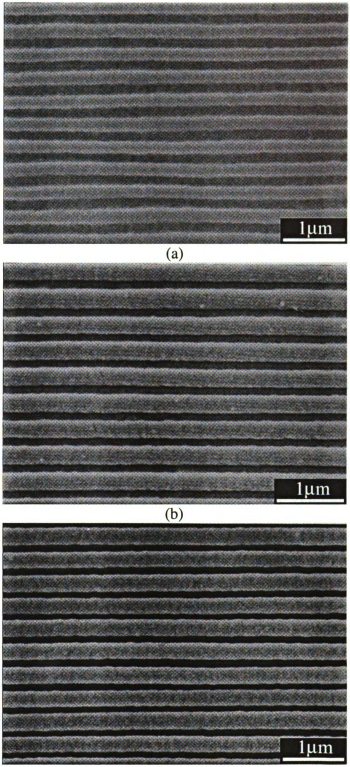

(a)

(b)

(c)

Figure 2.11 The effect of thickness on the image quality of substrate. (a) one layer (b) two layers (c) three layers of PMMA coatings.

the proximity effect became more prominent, as shown in Figure 2.12. Therefore, an optimal thickness needed to be determined.

c. Beam current and exposure time

Beam current and exposure time were key parameters in grating fabrication. Especially, these parameters affected the width of the trench, which eventually affected the frequency of the specimen grating. Equation 2.2 was used to calculate the electron dosage that was absorbed by the specimen. Some gratings were overdosed and underdosed as shown in Figure 2.13(a) and (b), respectively. During the electron beam scanning procedure, the scan raster in CamScan usually stayed at the edge of scanning area longer, which caused over exposure as shown in Figure 2.14.

To fabricate a crossed specimen grating, two perpendicular directions were scanned at the same area by rotating the scan raster 90°. The stigmatism and focusing then were readjusted after rotating the scan raster to assure that the electron beam was as small as possible. Figures 2.15(a) and (b) exhibit two gratings at 15° and 90°, respectively. The latter does not have any grating in the cross-section area because the PMMA layer was overdosed.

d. Conductive coating

Prior to PMMA coating, a conductive layer consisting of Au or Al was coated onto the specimen. Al coating was better than Au coating because the Al coating yielded fewer backscattered and secondary electrons due to its lower atomic number. The lower the interaction volume resulting from these electrons, the fewer proximity effects on fabricating the grating. Two Glass/Epoxy composite specimens were coated with Al and Au respectively prior to PMMA coating. Both specimens were then subjected to the

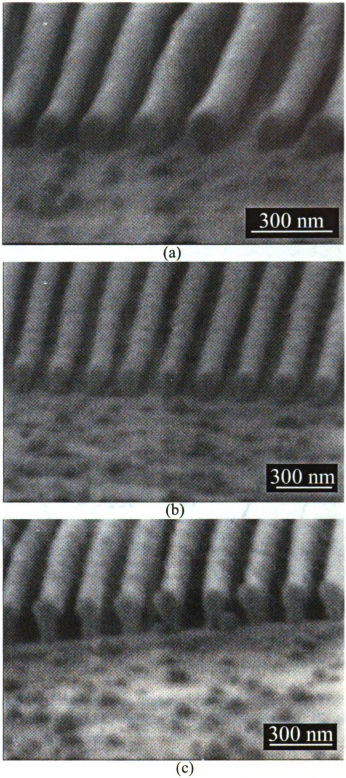

Figure 2.12 The proximity effect with different thicknesses of PMMA coating. (a) 75 nm, (b) 113 nm, and (c) 150 nm.

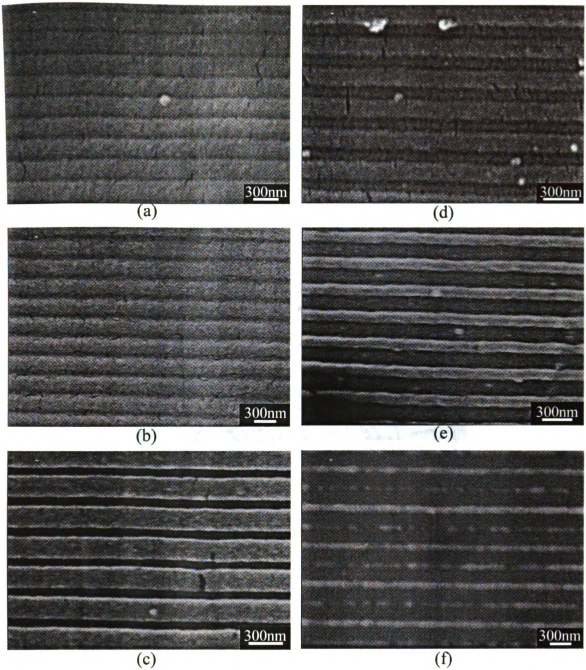

(a) (d)
(b) (e)
(c) (f)

Figure 2.13 The width of trenches at various electron dosages. The line dosage is (a) 0.156 nC/cm (b) 0.312 nC/cm (c) 0.468 nC/cm (d) 0.624 nC/cm (e) 0.780 nC/cm (f) 2.338 nC/cm.

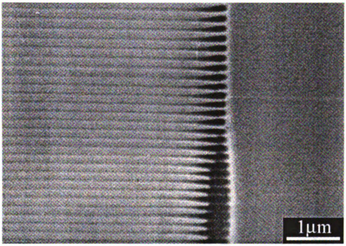

Figure 2.14 The over exposed edge of a specimen grating.

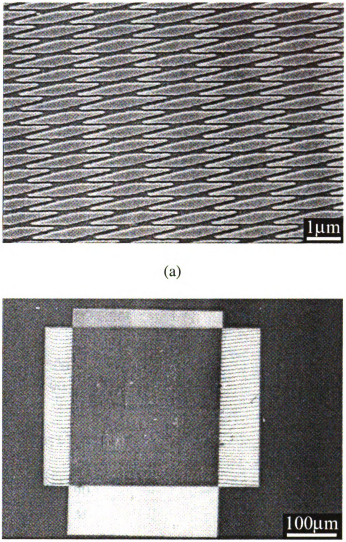

(a)

(b)

Figure 2.15 Two specimen gratings intersected at (a) 15° and (b) 90°. The middle area in (b) was overdosed.

same exposure conditions. The Al coated specimen had a more distinguished grating than the Au coated specimen did as shown in Figures 2.16(a) and (b).

a. Thermal damage

Due to the nonconductive nature of PMMA thin film, the specimen grating experienced thermal damage during SEM observation because the incident electrons were accumulated at the PMMA layer, even with a conductive layer of gold on its surface. Figures 2.17(a) and (b) showed severe thermal damage to gratings such as distortion and burst bubble respectively.

A. Sensitivity

The sensitivity of displacement measurement of the moiré method is determined by the number of moiré fringes per unit displacement. To obtain one additional moiré fringe from the SEM moiré method, the deformed strain needs to be at least 0.2% (1/500). For example,

in a null field, $f_s = f_r = \dfrac{500}{\dfrac{90}{M}}$;

one additional moire fringe observed on TV monitor,

$$F = \frac{\pm 1}{\dfrac{90}{M}} = f_r - f_s', f_s' = f_r - \frac{\pm 1}{\dfrac{90}{M}};$$

strain needed,

$$\varepsilon = \frac{p_s' - p_s}{p_s} = \frac{p_s'}{p_s} - 1 = \frac{f_s}{f_s'} - 1 = \frac{f_s - f_s'}{f_s'} = \frac{\dfrac{1}{\dfrac{90}{M}}}{\dfrac{500}{\dfrac{90}{M}} - \dfrac{\pm 1}{\dfrac{90}{M}}} = \frac{1}{500 \mp 1} \approx 0.2\%,$$

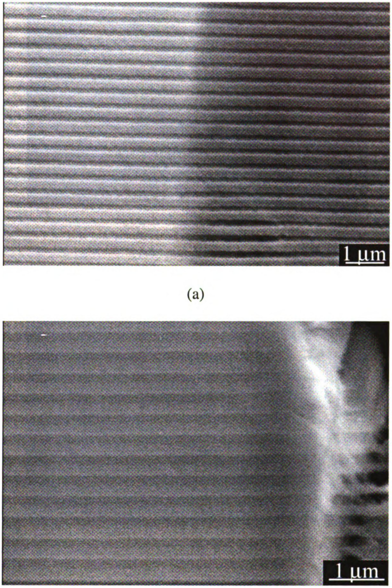

(a)

(b)

Figure 2.16 (a) A PMMA grating on Glass/Epoxy substrate with Al coating. (b) A PMMA grating on Glass/Epoxy substrate with Au coating.

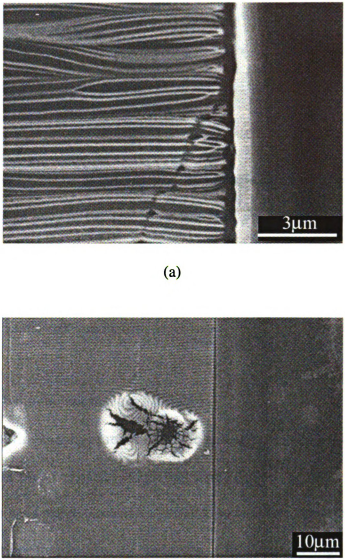

(a)

(b)

Figure 2.17(a) The specimen grating was distorted due to the thermal damage caused by the electron beam. (b) A burst-bubble-like specimen grating was observed due to the localized poor adhesion between the substrate and the grating after thermal damaged by the electron beam.

where f_s: frequency of initial specimen grating
f'_s: frequency of deformed specimen grating
f_r: frequency of reference grating
F: frequency of moiré fringe
M: magnification factor
ε: strain
p_s: pitch of initial specimen grating
p'_s: pitch of deformed specimen grating.

D. Image Quality

A higher aspect ratio of grating as well as a sharp corner of edge will result in a higher contrast of fringe patterns because the intensity of secondary electrons between the trench and edge will higher. Furthermore, the backscattered electrons are also another way of imaging fringe patterns as long as the grating exhibits a periodic difference in atomic number such as diblock copolymer.

E. Restrictions

a. Specimen has to be in the vacuum environment.

b. The PMMA thin film coating is reinforcing the testing specimen to some extent since the specimens that need be studied are getting smaller.

c. It is important to have stable electronics in SEM, such as for stable magnification and scanning raster, since they control the frequency of reference grating.

d. The grating area produced from regular SEM such as CamScan is limited by the manufacturer's pre-set parameters; for instance, scanning area (120 mm by 90 mm at 1x), scanning lines per frame (1250 lines/frame), and exposure time (21, 42, 85, 171 seconds). Due to these pre-set parameters, it is difficult to control the precise electron dosage to fabricate high frequency of specimen gratings.

e. To form moiré fringes, the reference grating, which is produced by raster scanning, has to match the frequency of specimen gratings. The magnification for moiré fringe formation can be calculated using Equation 2.3. The TV scanning rate for imaging mode is 500 lines/frame in CamScan and the height of scanning area at 1:1 is 90 mm. Therefore, the applied strain to observe one extra fringe is 0.2%. Increasing scanning lines/frame in the TV scanning mode will result in a larger imaging area and higher sensitivity but will reduce the details of imaging area.

Chapter 3
MOIRÉ IN ATOMIC FORCE MICROSCOPE

3.1 INTRODUCTION

Purely based on interference, geometric moiré was once commonly used in engineering measurements. With the use of lasers, optical diffraction was integrated with optical interference to form a more refined moiré technique, namely moiré interferometry. The technique of moiré interferometry has been well documented by Post, Han and Ifju [16] and widely demonstrated by them and many other researchers. It is well recognized that moiré interferometry is a very powerful and accurate technique for strain measurements in engineering applications.

By integrating a moiré interferometer with an optical microscope, Han [38] extended moiré interferometry to microscopic strain measurements. With the introduction of a transparent moiré grating, Liu and Shakour [39] further demonstrated the feasibility of simultaneous viewing and measuring microscopic deformation of composite materials by a microscopic moiré interferometry. The capability of combining observation and measurement together accelerated the study of micromechanics. In fact, this capability had also been demonstrated in electron beam moiré by Dally and Read [30].

The electron beam moiré [40] is a geometric moiré technique in the microscopic sense. It utilizes both electron beam lithography to generate moiré grating on specimen surface, i.e. specimen grating, and the scan raster of SEM (Scanning Electron Microscope) as reference grating. As a result of interference between the specimen grating and reference grating, moiré fringes are formed. Hence, both microscopic observations based on SEM and microscopic measurements based on electron beam moiré could be obtained simultaneously. The electron beam moiré has proved useful for many applications which require microscopic measurements.

As an advanced step for microscopic and even nanoscopic observations, scanning probe microscopes are commonly used for atomic-level investigations. The current study uses an atomic force microscope (AFM) for microscopic measurements, besides the conventional use for microscopic observations. The primary goal is to demonstrate the feasibility of forming moiré fringes in AFM. Further developments similar to that in electron beam moiré are anticipated.

3.2 GRATING TECHNIQUE

A epoxy specimen material was coated with a 14 nm thick of Al and spin-coated with a layer of polymethylmethacrylate, PMMA, about 110 nm thick. E-beam lithography was used for fabricating specimen grating. A thin film of PMMA was scanned by an SEM for generating a moiré grating [41] of 3,103 lines per millimeter, which is a specimen grating. Then the specimen with the PMMA thin film was developed in an organic solvent and coated with gold to protect the PMMA grating even though such as coating is not required for studies in AFM.

3.3 MOIRÉ FRINGES IN AFM

The atomic Force Microscope is essentially used for measuring surface topography with sensitivity in nanometer or even sub-nanometer levels. It is essentially based on atomic force, i.e. the Coulombic force between the electron shells of two approaching atoms. As a common practice, constant force is used in an AFM system. A probe with a nano-scale tip attached to a cantilevered beam is then used to detect a target. If the target is too far or too close from a designated distance, the probe will be bent convex or concave to keep the right distance and maintain the constant atomic force. A laser beam is usually used to detect the deflection of the cantilevered beam. The information is then fed to a piezoelectric actuator located beneath the specimen to move it up and down to level the probe.

In order to collect the topography of a domain, the probe is kept stationary; whereas the specimen is moved from one side to the other followed by a constant advancement. As a consequence, the scanning lines can be used as reference grating. Once they are superposed on the moiré grating on the specimen surface, a moiré fringe pattern will be formed and called AFM moiré.

An area of 38.4 μm by 38.4μm was chosen for investigation. In order to match the frequency of the specimen grating, a scanning frequency of 128 lines was selected with a scanning rate of 1 Hz. Hence, the reference grating has a frequency of 3,333 lines per millimeter. Moiré fringes were clearly recorded, accordingly.

3.4 VERIFICATION

In order to verify that the obtained fringes were really due to the interference between the specimen grating and the reference grating (for instance from the geometric moiré), the specimen was rotated with small angles with respect to the scanning lines. Figure 3.1 shows the fringe pattern changes with the rotation angle. As the angle increases, the frequency of the moiré fringe increases. The result from a careful

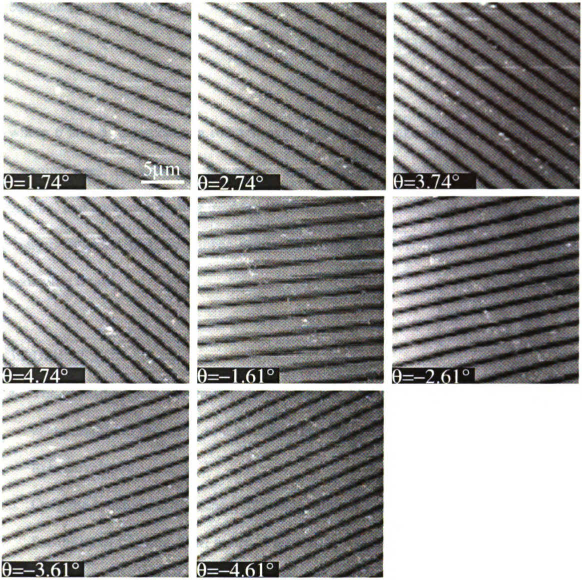

Figure 3.1 Moiré fringe patterns at various specimen rotation angles.

measurement is presented in Figure 3.2 along with the prediction from the analytical equation [35] given below:

$$\tan\theta = \frac{\sin\phi}{\cos\phi + \dfrac{p_f}{p_r}} \tag{2.4}$$

where θ and ϕ are specimen rotation angle and moiré fringe angle with respect to the scanning lines, respectively, and p_f , p_r, and p_s are pitches of moiré fringe, reference grating, and specimen grating, respectively. The agreement between the experiment and analysis suggests that the fringes shown in AFM do follow the predictions based on geometric moiré.

3.5 DISCUSSION

a. The specimen grating in this study was produced by electron beam lithography. It is also possible to use AFM to a generate specimen grating though the technique needs to be developed.

b. Only the rotation between the two grating systems was performed to demonstrate the feasibility of forming AFM moiré. Presumably a testing fixture could also be built to perform moiré studies based on mechanical loading.

c. The moiré fringe pattern at the initial stage (undeformed condition) is not necessary to be of a null field, due not only to the mismatch of frequency between the reference grating and the specimen grating but also to the misalignment between them. The initial fringe pattern can always be subtracted from that of deformed one in deformation analysis.

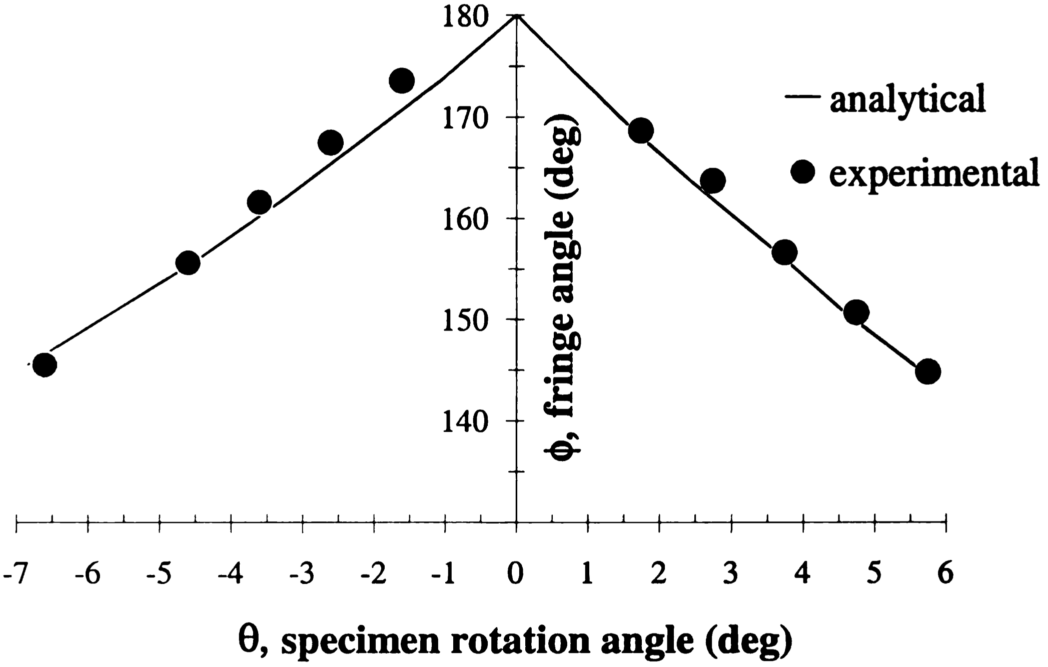

Figure 3.2 Comparisons between experimental and analytical results of moiré fringe angle with respect to specimen rotation angle.

d. AFM moiré is more convenient and economical than the electron beam moiré since the latter requires a vacuum environment for investigation and a conductive layer not only for preventing thermal damage to non-conductive specimens but also for avoiding possible contamination to the electron gun.

e. Electron beam moiré is able to provide both microscopic measurements and observations simultaneously. As a surface topography technique, the AFM moiré cannot provide microscopic measurements simultaneously with microscopic observations since the target specimen is coated with moiré grating, as shown in Figure 3.3.

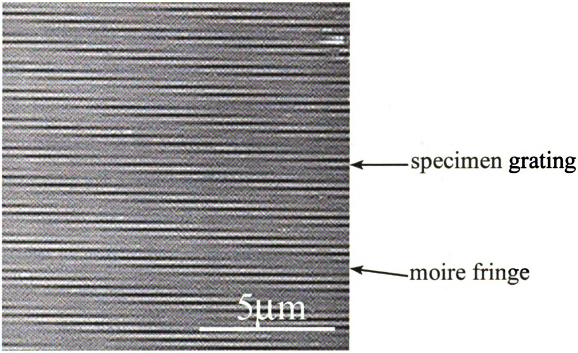

Figure 3.3 Coexistence of a specimen grating and moiré fringes.

Chapter 4

NEW GRATING TECHNIQUE FOR AFM MOIRÉ AND SEM MOIRÉ

4.1 INTRODUCTION

A moiré technique based on an atomic force microscope (AFM), namely AFM moiré, has been introduced in a previous study [42]. The technique utilizes electron beam lithography to cast a moiré grating on a specimen surface, i.e. specimen grating, and utilizes the viewing scanner of the AFM to provide a reference grating. As a result of interference between these two gratings, moiré fringes are formed and can be viewed instantaneously on the monitor. A demonstration has been presented in the previous study along with a careful verification showing a good agreement between experimental investigation and theoretical calculation. It has been concluded that AFM moiré is feasible for measurements of microscopic or even nanoscopic deformations. Since an AFM does not require a vacuum environment, as needed in an SEM (scanning electron microscope), AFM moiré is more convenient than SEM moiré [30] in microscopic measurements.

The electron beam lithography used in preparing specimen grating for AFM moiré and SEM moiré requires multiple procedures of coating and developing. Usually, a specimen is coated with a conductive layer before being coated with a photoresist material such as PMMA. The photoresist layer is then subjected to preset electron beam scanning for lithography. It then needs to be developed, fixed and rinsed before being used as moiré grating. These procedures are time-consuming and labor-intensive. Since the specimen or the area of interest for microscopic measurements is usually very small, the reinforcement effect of the grating on the specimen should not be neglected. In other words, the grating layer could reinforce the specimen, at least locally, to some extent and cause measurement error. Hence, a grating technique capable of reducing the reinforcement effect to a minimum, such as using a low-modulus material and a thin coating, should be developed. This chapter presents such a new grating technique.

4.2 GRATING TECHNIQUES

The moiré phenomenon observed in SEM has long been recognized by SEM users. The undesired moiré fringes in SEM are attributed to specimen topography and SEM related sources. To reduce, if not to eliminate, the moiré phenomenon has been an important issue in research related to SEM. Besides the specimen topography, there are two main sources responsible for SEM moiré phenomenon, namely the voltage contrast [43] and the contamination [44]. The former usually occurs in specimens with poor electrical conductivity. Under direct electron beam scanning, the incident electrons tend to accumulate along the scanning lines, resulting in non-uniform voltage potential in the scanned zone. When the electron-rich specimen is further scanned under a different magnification factor or angle, a moiré fringe pattern can be formed. In that pattern, those lines consisting of high-density electrons form the specimen grating while the scanning lines of viewing provide the reference grating. Although the moiré fringe pattern can be viewed instantaneously on the monitor, it is really a dynamic phenomenon. When the lines of accumulated electrons change, the moiré fringe pattern changes. When the accumulated electrons fade away, so do the moiré fringes. Thus, the moiré grating based on the voltage contrast may be considered as temporary grating. Figure 4.1 shows the

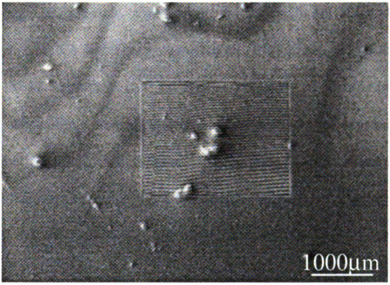

Figure 4.1 Moiré fringe pattern in an alumina specimen with grating based on voltage contrast.

moiré fringes in an alumina specimen. The specimen grating, not shown in the diagram, was created by exposing the specimen to a stable beam current of 2 nA, an acceleration voltage of 4keV and a scanning time of 30 seconds with a working distance of 12 mm.

The other SEM-related moiré grating is relatively permanent. It is the deposition of carbonaceous products derived from the polymerization of contaminated organic molecules under electron irradiation inside SEM vacuum chambers. The following sources of contamination are commonly encountered in SEM practices: the vacuum pump oil, the organic molecules adsorbed on the specimen surface and the specimen itself. Although cautions have been exercised in SEM practices [44-48], there is no warranty that SEM chambers can be kept completely contamination free. The backstreaming of vacuum pump oil into SEM chambers and the organic molecules on specimens cannot be completely avoided. Because a vacuum is required for SEM operations, residual vacuum pump oil and organic molecules could be easily vaporized, polymerized by electron irradiation, and then deposited on the specimen surface. A schematic diagram shows this process is presented in Figure 4.2. Once the carbonaceous products are deposited on the specimen surface, carbonaceous lines following the scanning pattern are built up. If the carbonaceous lines are well arranged, they can be used as moiré grating lines, i.e. carbonaceous grating.

An application of the carbonaceous grating for microscopic measurements has been mentioned [49]. Compared to the grating based on voltage contrast, the carbonaceous grating is more durable, if not permanent. Figure 4.3 shows the carbonaceous grating in an epoxy specimen coated with gold. The grating was cast by exposing the specimen to an electron beam with a current of 2 nA, an acceleration

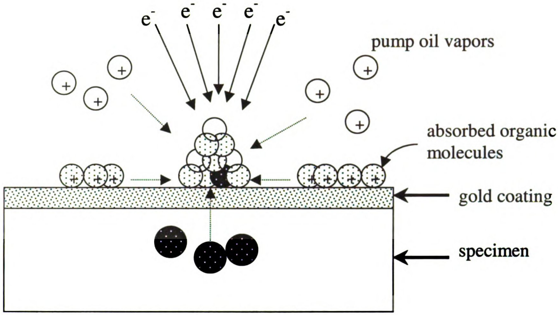

Figure 4.2 The formation of carbonaceous grating.

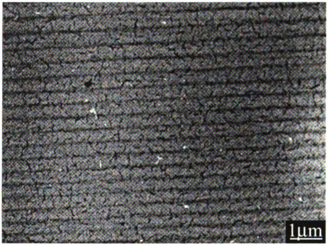

Figure 4.3 Carbonaceous grating in an epoxy specimen coated with gold.

voltage of 20keV, a scanning time of 30 seconds and a working distance of 20 mm.

4.3 CARBONACEOUS GRATING

The thickness of PMMA coating used in the electron beam lithography is usually around 100 nm. However, the carbonaceous grating based on contamination in SEM chamber and testing specimen can be as thin as 4 nm. Accordingly, the carbonaceous grating is superior to the lithographic grating for AFM moiré and SEM moiré because the former produces less significant effect of reinforcement on specimens than the latter. The thickness of carbonaceous grating is dependent on beam current, acceleration voltage and scanning time. If all of them are well adjusted, it is possible to have grating lines with a sufficient thickness [50,51]. The thickness can strongly affect the quality of moiré fringe pattern; i.e. the higher the thickness the better the image quality. Experiments have shown SEM moiré requires a thickness greater than AFM moiré. Figure 4.4 shows an AFM image of carbonaceous grating. The ridges and trenches can be clearly identified. However, it should be noted that it is a very delicate process to obtain grating lines with sufficient thickness. If the resultant electron dose based on beam current, acceleration voltage and scanning time is not sufficient, the thickness may be too low. However, if the carbonaceous deposition is overdone, the ridges may overlap one another and result in an unrecognizable moiré grating. Figure 4.5 shows an outline of a cross-section of carbonaceous grating. The outline is of mountainous shape with an average height of 8 nm and pitch of 250 nm.

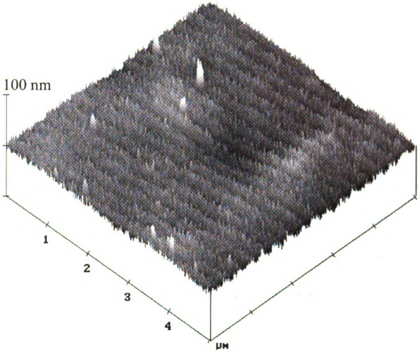

Figure 4.4 AFM image of carbonaceous grating.

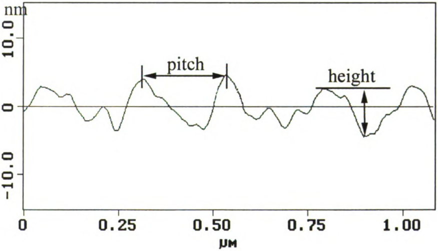

Figure 4.5 Outline of a cross-section of carbonaceous grating.

4.4 MOIRÉ FRINGES

The carbonaceous grating can be used for both AFM moiré and SEM moiré. Shown in Figure 4.6 are the moiré fringe patterns from SEM. The specimen was identical to the one used in Figure 4.3. The scan coil of the SEM was rotated by various angles with respect to the specimen for moiré analysis. Equation 2.4 can be used for analytical calculation. Both results from the experimental measurements and the theoretical calculations are shown in Figure 4.7 and seem to agree very well.

A similar study was performed in AFM for the epoxy specimen. Figure 4.8 shows the moiré fringes formed by rotating the specimen with respect to the scanning lines for several angles. Figure 4.9 again suggests a good agreement between the experimental results and corresponding theoretical calculations.

4.5 CONCLUSION

A careful study of carbonaceous grating based on contamination in SEM chamber and testing specimen is presented. The new technique is more convenient than that based on electron beam lithography. Good agreements between experimental results and theoretical calculations have verified the feasibility of using the carbonaceous grating for the AFM moiré and the SEM moiré.

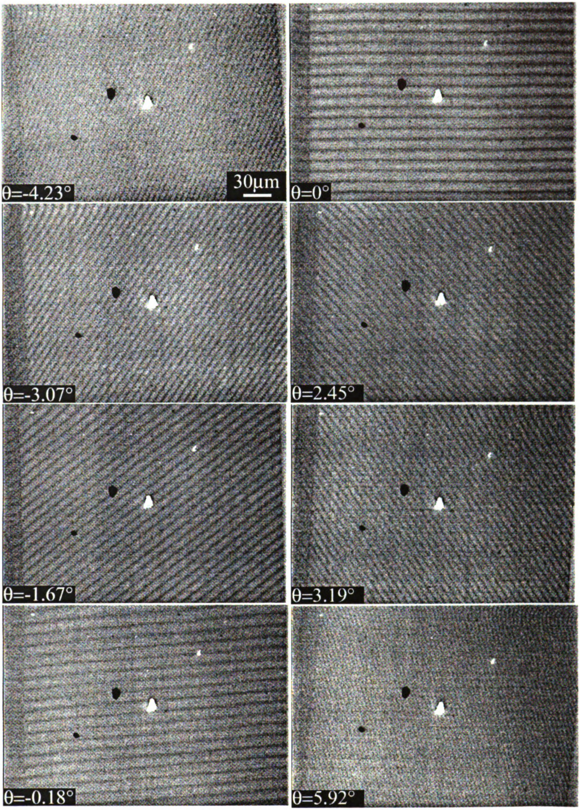

Figure 4.6 SEM moiré fringes.

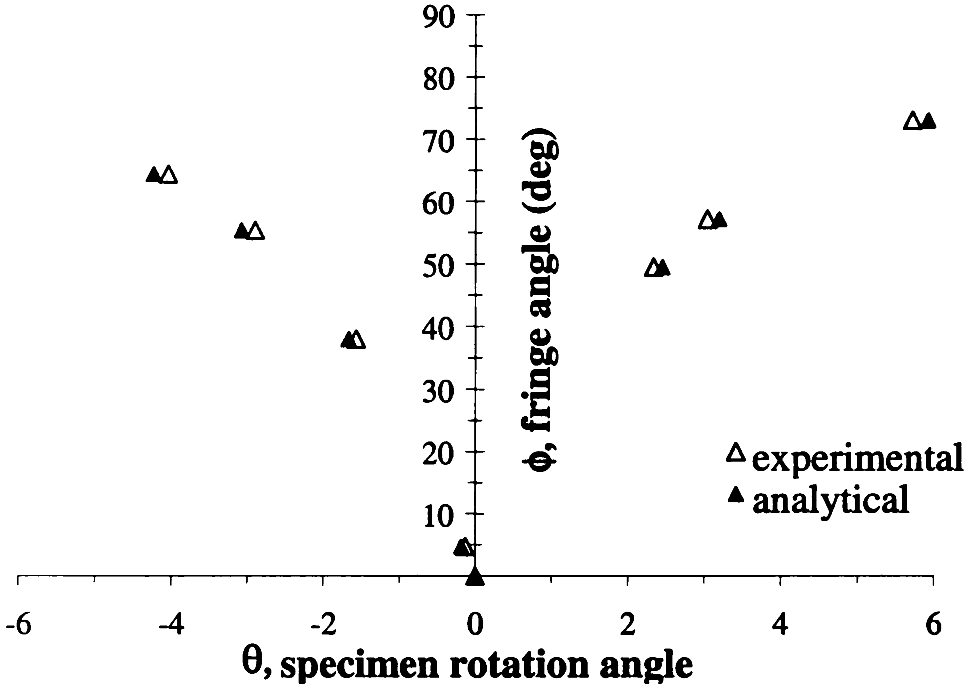

Figure 4.7 Comparisons between theoretical calculations and experimental measurements for SEM moiré fringes.

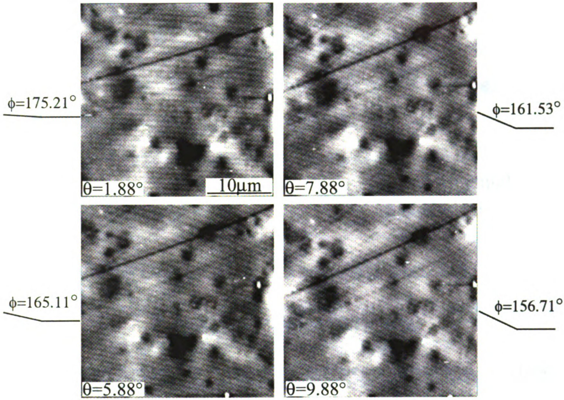

Figure 4.8 AFM moiré fringes.

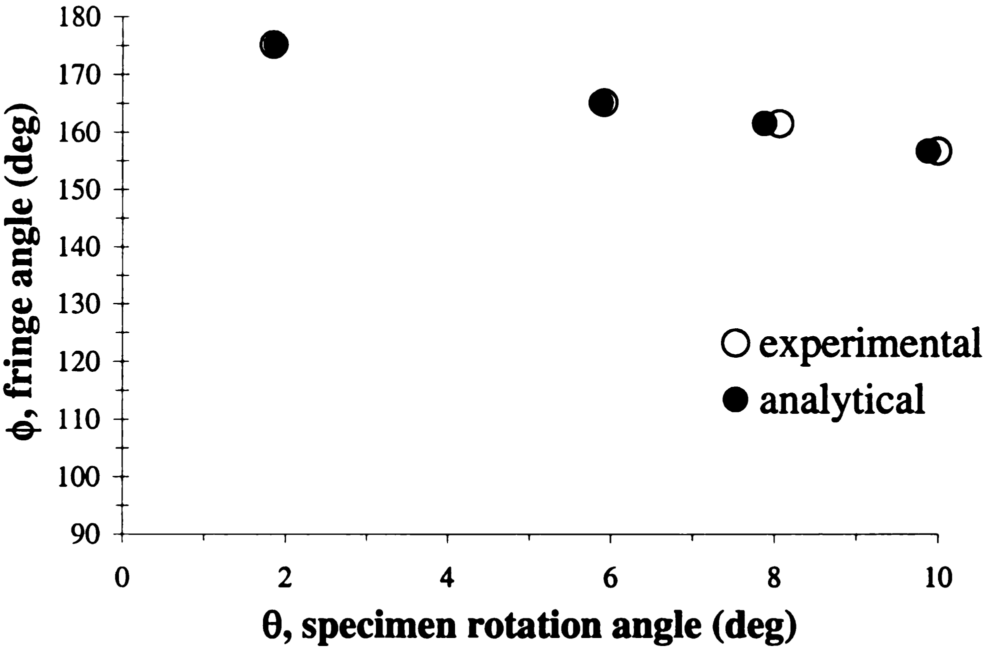

Figure 4.9 Comparisons between theoretical calculations and experimental measurements for AFM moiré fringes.

Chapter 5

NEW VIEWING TECHNIQUES FOR SEM MOIRÉ

5.1 INTRODUCTION

Based on interference of two sets of grating (lines with periodic spacing), the geometric moiré method [52] has been an useful tool for displacement measurements. As technologies advance, new experimental methods and grating producing techniques have been introduced. These technologies have been integrated into the moiré method to fundamentally change it. One significant development in the moiré method has been the use of laser light, and this eventually has led to a completely new method called the moiré interferometry method. Post, Han and Ifju [16] have summarized the method comprehensively.

The moiré interferometry method utilizes the interference of two laser beams to form a moiré grating [26,27,53,54]. Being attached to the surface of a specimen, a moiré grating is subjected to loading or deformation identical to that exerted on the specimen. When the moiré grating is illuminated by two laser beams with special incident angles, diffracted beams will interfere with each other and form a moiré fringe pattern. The major advancement of the moiré interferometry method over the geometrical moiré method is the increase of frequency from about 50 lines/mm to 2400 lines/mm. Accordingly, the moiré interferometry method is useful for measurements requiring high accuracy. Its applications have also been proved feasible for microscopic measurement [13].

By using a medium of high index of refraction, Han [13] has pushed the frequency of moiré grating up to 4800 lines/mm. However, further increase in grating frequency is hindered by the wavelength of laser light. In order to increase the frequency, hence the sensitivity of the moiré method, a technique independent of light source is preferred. Based on electron beam lithography, Smith, Chinn and DeGraff [40] have demonstrated the feasibility of casting grating on specimens and viewing moiré fringes by a scanning electron microscope (SEM). Kishimoto, Egashira, Shinya and Carolan [55] have named the technique electron beam moiré method by combining electron beam lithography and scanning electron microscope and used it for microscopic measurements.

Besides the moiré interferometry method, the electron beam moiré (or SEM moiré) method is another significant development in moiré methods. It is especially useful for measurements of microscopic deformation and has been proved to be a reliable technique. Dally and Read [30] have further investigated the details of the technique and established the fundamental theory of SEM moiré method [33]. They have demonstrated that a frequency of 10,000 lines/mm or higher is feasible [30]. They and other researchers have used the SEM moiré method to measure microscopic deformation of fiber-reinforced composite materials [31,32,56]. The extension of its applications to electronic packaging has also been reported [57-60].

5.2 ELECTION BEAM LITHOGRAPHY

Electron beam lithography is a commonly used technique. Similar to the Smith group, the Kishimoto group and the Dally-Read group have used electron beam lithography to cast a moiré grating, namely lithographic grating. The technique, in fact, has been primarily used in semiconductor processes and MEMS (microelectromechanical systems) fabrication. It is a technique based on spin-coating a thin PMMA (polymethylmethacrylate) layer on the surface of a well-polished and gold-coated (especially for non-conductive materials) specimen. Once the polymer coating layer is cured, the specimen is then subjected to electron beam scanning for lithography.

After being scanned by an electron beam, the molecular chains of PMMA are scissored. The specimen is then submerged in a chemical for etching. In that process, degraded PMMA molecules are dissolved away and removed; whereas the non-degraded (unscanned) ones remain intact. A solvent (isopropanol mixed with methyl isobutyl ketone (MIBK) in a 3:1 volume ratio) is usually used for chemical etching. The specimen is usually etched for 40 seconds. It is then rinsed in a 100% isopropanol fixer for 20 seconds and followed by a second rinse in distilled water for 30 seconds.

The scanning trajectory of the electron beam in an SEM is controllable. It is possible to achieve any kind of two-dimensional scanning pattern by adjusting the magnetic field of the scan coil, scanner, to deflect the electron beam. A periodic scanning pattern consisting of straight lines with constant spacing can be achieved by advancing a constant movement after each line scan. Hence, a moiré grating with a desired frequency can be obtained. Figure 5.1(a) shows trenches and ridges of a moiré grating based on electron beam lithography. Figure 5.1(b) is a schematic diagram of the cross section of Figure 5.1(a). The grating has a frequency of 5539 lines/mm or a pitch of 181 nm.

Both the quality and the frequency of a moiré grating are important in applications of the SEM moiré method. The quality can affect the resolution of the moiré fringe pattern while the frequency of a grating is responsible for the sensitivity of the

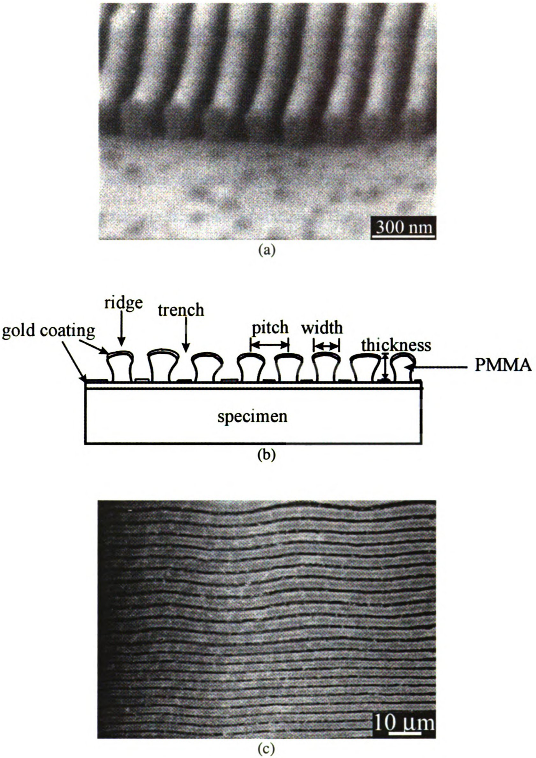

Figure 5.1(a) SEM image of lithographic grating (b) Schematic diagram of cross-section of grating (c) Moiré fringes.

SEM moiré method. The quality of moiré grating involves many features. The aspect ratio of thickness-to-width of ridge seems to be the most important element. According to Figure 5.1(b), the moiré grating shown in Figure 5.1(a) has an aspect ratio (thickness/width) of 1.14 and is able to give a high-quality moiré fringe pattern, such as the one shown in Figure 5.1(c).

In order to achieve a desired aspect ratio of the moiré grating, both electron dosage and etching rate are important parameters. The electron dosage is a resultant strength of incident electron beam bombarded on the specimen and includes many parameters, depending on the SEM used. For the SEM used in this study, the electron dosage combines effects due to acceleration voltage, beam current, scanning time and working distance of the electron beam. The etching rate, however, depends upon the concentration of the solvent and the developing time. Apparently, it requires significant efforts to facilitate a set of parameters for operating the SEM to achieve a desired aspect ratio. The SEM and its parameters used in casting the moiré grating are given in Appendix A.

The frequency of a moiré grating, f_g, is dependent on the scanning rate and scanning area per scanning frame. It is given by

$$f_g = \frac{\text{number of scanning lines}}{\text{height of scanning area}} \mathrm{M} \tag{5.1}$$

where M is a magnification factor. For example, for a scanner with a scanning rate of 1250 lines/frame and a scanning area of 120 mm-by-90 mm (length x height), the SEM requires a magnification factor of 360 to achieve a 5000 lines/mm of moiré grating. The corresponding scanning area is then reduced to only 333 μm x 250 μm. Accordingly, as the magnification factor increases, the frequency of moiré grating increases; whereas the scanning area decreases. However, the magnification factor displayed on the SEM console changes in discrete numbers while the control of magnification factor changes continuously for the SEM used in this study. Therefore, the frequency of specimen grating varies even at the same magnification factor displayed on the SEM console. Although a frequency of 10,000 lines/mm or higher is possible, according to Equation 5.1, a careful control of scanning and etching processes is required. If the electron dosage is too high, the roots of grating lines could be very narrow, resulting in a phenomenon called proximity effect. Figure 5.2(a) shows a grating due to overdosage of electrons and the corresponding schematic diagram. The overlapping of neighboring scans destroys the surface integrity of the PMMA layer, leaving a very thin, ambiguous grating. Conversely, if the dosage is insufficient, the aspect ratio may be too small and the quality of moiré fringe pattern may become too poor to recognize. Figure 5.2(b) shows a grating due to underdosage of electrons and the corresponding schematic diagram of the cross section. A useful grating is shown in Figure 5.1(b) for comparison. Experiments have shown that a moiré grating with a frequency around 5000 lines/mm can be repeated consistently based on the facilities used in this study.

5.3 FORMATION OF MOIRÉ FRINGES

Moiré methods are aimed at forming moiré fringe patterns for deformation measurements. Forming a moiré fringe pattern requires two gratings: the specimen grating and the reference grating. The grating mentioned earlier is made of PMMA and deposited on the specimen surface; it is the specimen grating. The second grating is formed by the scanning lines during fringe-viewing stage, and is the reference grating.

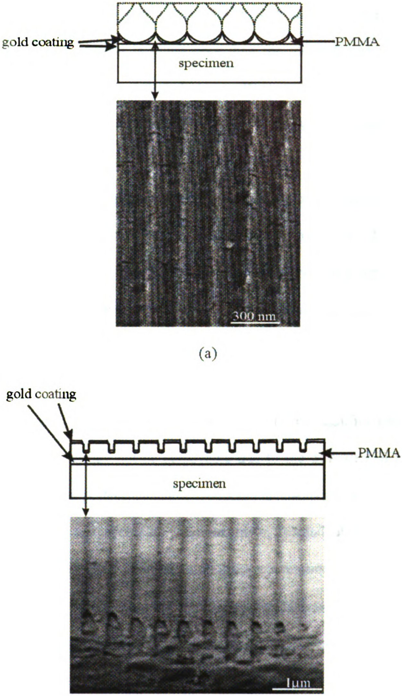

(a)

(b)

Figure 5.2(a) Moiré grating due to overdosage of electrons and corresponding schematic diagram. (b) Moiré grating due to underdosage of electrons and corresponding schematic diagram.

The interference of these two gratings results in a moiré fringe pattern. Since the resolution of the moiré gratings is much poor than the moiré fringe pattern under the fringe-viewing stage, only the moiré fringe pattern and the microstructure of the specimen surface can appear in the SEM image. The moiré grating are usually not visible.

The frequency of reference grating is dependent on the features of the viewing scanner (see Appendix A) and is also governed by Equation 5.1. For example, if a viewing scanner has a viewing rate of 500 lines/frame for a viewing area of 120 mm x 90 mm, the frequency of reference grating will be dependent on the magnification factor *M* only. In other words, the frequency of the reference grating can be changed by adjusting the viewing area. Matching the frequency of the reference grating with that of 5539 lines/mm of specimen grating requires an adjustment of the magnification factor to 997. However, this odd factor may not be achievable due to the difficulty in fine tuning the magnification. In fact, a perfect match of frequency between the specimen grating and the reference grating is not necessary. For example, instead of 997, a magnification factor of 1000 may be selected. This selection gives a reference grating with a frequency of 5556 lines/mm and a reduction of the viewing area to 120 μm x 90 μm. In addition, it should be noted that there is a difference of 17 lines/mm between these two gratings. The difference will appear in the SEM image as 17 moiré fringes per millimeter and is usually taken as initial fringes in deformation analysis.

In SEM moiré method practices, both the scanning rate for lithography (e.g. 1250 lines/frame) and the viewing rate for imaging (e.g. 500 lines/frame) are features of the SEM used in this study. They are usually fixed values. As the magnification factor increases, the frequencies of the specimen grating and the reference grating increase; however, the scanning area and the viewing area decrease while the sensitivity of the SEM moiré method remains the same. The sensitivity is tied only to the fixed value of the scanning rate or the viewing rate. Since the viewing rate is smaller than the scanning rate, the former determines the sensitivity of the SEM moiré method. Accordingly, no matter how small or how large the magnification factor is, there are only 500 viewing lines per frame. Since at least one moiré fringe should be generated in a scanning frame for the image to be qualified as a moiré fringe pattern, a strain of 1/500 (0.2%) is the minimum requirement. This value is quite high for many engineering materials.

The current SEM moiré method is based on electron beam lithography and scanning electron microscope. Both of them have been well developed and many details of the techniques are available in literature. However, as mentioned earlier, the electron beam lithography relies on a layer of PMMA coating. Although the thickness of the PMMA layer in the trenches can be dissolved away as shown in Figure 5.1(a), it still poses a concern of reinforcing the specimen by the thickness of ridges. The reinforcement effect of grating, the complicated processing of lithographic grating and the low sensitivity - the minimum strain (0.2%) required for generating a moiré fringe - are drawbacks of the existing SEM moiré method. In order to reduce the effects of these drawbacks, the following developments are required:

(1) a convenient technique for casting moiré grating,

(2) a specimen grating with insignificant reinforcement effect,

(3) a viewing technique with a higher sensitivity.

5.4 NEW TECHNIQUES

Based on the requirements listed above, a new grating-casting technique and a new fringe-viewing technique are developed.

5.4.1 Carbonaceous Grating

This grating producing technique is based on the well-known contamination in SEM chambers. It turns the negative defect of SEM to a positive application. This technique relies on the deposition of carbonaceous products derived from the polymerization of contaminated organic molecules under electron irradiation inside evacuated SEM chambers.

The following sources of contamination are commonly encountered in SEM practices: the vacuum pump oil, the organic molecules adsorbed on the specimen surface and the specimen itself. Although cautions have been exercised in SEM practices, there is no warranty that SEM chambers can be kept completely contamination free [44-48]. The backstreaming of vacuum pump oil into SEM chambers and the organic molecules on specimens cannot be completely avoided. Because a vacuum is required in SEM operations, residual vacuum pump oil and organic molecules can be easily vaporized, polymerized by electron irradiation, and then deposited on the specimen surface. Once the carbonaceous products are deposited on the specimen surface, carbonaceous lines are built up following the scanning pattern. If the carbonaceous lines are well arranged, they can be used as moiré grating lines, i.e. carbonaceous grating. Nshaninan, Dove, and Rajan [49] were the first to explore the use of the carbonaceous grating for a microscopic investigation. Figure 4.3 shows the carbonaceous grating in an epoxy specimen coated with gold. The grating was cast by exposing the specimen to an electron beam with a current of 2 nA, an acceleration voltage of 20 keV, a scanning time of 30 seconds and a working distance of 20 mm.

The thickness of PMMA coating used in the electron beam lithography is usually around 100 nm. However, the carbonaceous grating based on contamination in the SEM chamber and testing specimen can be as thin as 4 nm. Accordingly, the carbonaceous grating should give a less reinforcing effect on a specimen than the lithographic grating does. The thickness of carbonaceous grating is dependent on electron dosage. If it is well adjusted, grating lines with a sufficient thickness can be achieved [50,51].

The grating thickness can strongly affect the quality of moiré fringe pattern, i.e. the greater the thickness the better the image quality. Figure 4.4 shows an AFM image of carbonaceous grating. The ridges and trenches can be clearly identified. Figure 4.5 shows the outline of a cross-section of the carbonaceous grating. The outline has mountainous shape with an average thickness of 7.5 nm and a pitch of 246 nm. However, one need to note that a careful control of scanning is required to produce sufficiently thick grating lines. As in the casting of lithographic grating, if the resultant electron dosage is not sufficient, the thickness may be too small. On the other hand, if the carbonaceous deposition is overdone, the ridges may overlap one on another and result in an unrecognizable moiré grating.

5.4.2 Total Imaging

In order to prepare a specimen grating, a high magnification factor is preferred as long as the scanning area for grating-casting is larger than that of interest. In the fringe-viewing stage, however, the magnification factor needs to be adjusted so that the reference grating matches the specimen grating as closely as possible. For the SEM used in this study, there are two types of scanning/viewing scanner: the monitor scanner and the photograph scanner. The fundamental techniques of the two scanners are similar. Both of them can be used as scanners for lithographic grating and as viewers for reference grating. However, the monitor scanner presents an instantaneous image on the SEM monitor while the photograph scanner presents a hardcopy image after a photographic process.

Besides the difference of image presentations, another difference between the two scanners is the scanning/viewing rate. For example, for the SEM used in this study, the monitor scanner has a frequency of 500 lines/frame while the photograph scanner has a frequency of 1250 lines/frame. Thus, the photograph scanner has a sensitivity higher than twice of the monitor scanner.

Through the use of the photograph scanner for fringe-viewing, the sensitivity of the SEM moiré method is more than doubled as compared to that using the monitor scanner since the minimum strain required to form one moiré fringe is reduced to a level well below half, i.e. from 0.2% (1/500) to 0.08% (1/1250). Because the sensitivity is dependent on the viewing rate, which is a fixed value depending on the SEM used, the sensitivity cannot be increased according to needs. For example, when the specimen or the area of interest becomes smaller, it makes more sense to use a smaller strain. However, with the fixed value of viewing rate, it is impossible to reduce the required minimum strain to form a single moiré fringe. In order to improve the sensitivity, a possible approach is to record the total image of gratings and moiré fringe pattern, instead of only the moiré fringe pattern.

When a specimen is under deformation and is scanned by an SEM, a grating for the deformed specimen can be created. This grating, called the deformed specimen grating, is similar to the specimen grating initially cast on the specimen, i.e. the initial specimen grating. A moiré fringe pattern based on the interference between the deformed specimen grating and the initial specimen grating can be identified by viewing these two specimen gratings by an SEM. The technique used to view both moiré grating and moiré fringe patterns is called total imaging.

A moiré fringe pattern obtained from total imaging is of a real image; whereas that obtained from either monitor viewing or photograph viewing is of a virtual image. However, it should be noted that the real image is not as distinct as the virtual image since the former is embedded in the gratings and is an implicit pattern while the latter stands out of the gratings and is an explicit pattern. Figure 5.3(a) shows a moiré fringe pattern and the corresponding initial specimen grating and deformed specimen grating of lithographic type. Figure 5.3(b) shows a moiré fringe pattern and the corresponding initial specimen grating of carbonaceous type. The deformed specimen grating is not visible though sometimes it is traceable around the boundary of an SEM image.

5.5 SIX SEM MOIRÉ METHODS

Based on the new techniques mentioned above, there are two grating producing techniques, i.e. lithographic grating and carbonaceous grating, and three viewing techniques, i.e. monitor viewing, photograph viewing, and total imaging. A total of six SEM moiré methods can be available by combining one technique from each of the two groups.

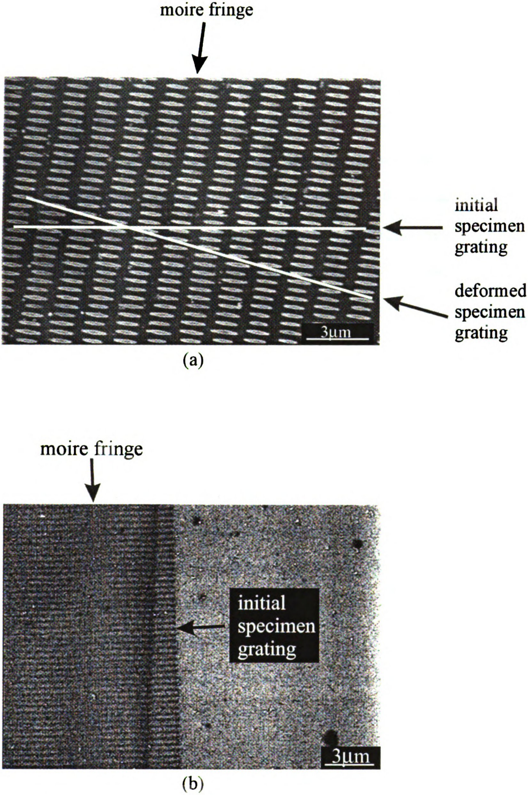

Figure 5.3(a) Total imaging of lithographic grating. (b) Total imaging of carbonaceous grating.

5.5.1 Lithographic Grating and Monitor Viewing (LM)

This is the SEM moiré method currently used by many researchers. It utilizes a photograph scanner, instead of the monitor scanner, to cast lithographic grating on the specimen surface because the photograph scanner has a frequency of 1250 lines/frame, which is higher than the monitor scanner that has a frequency of 500 lines/frame. The moiré fringe pattern is formed when the specimen is subjected to loading or deformation and viewed by the monitor scanner. The image of fringe pattern on the monitor is synchronized with the monitor scanner. Hence, instantaneous or even dynamic measurements are possible.

5.5.2 Lithographic Grating and Photograph Viewing (LP)

This method is very similar to LM. While very similar to LM, this technique utilizes the photograph scanner for both electron beam lithography and moiré fringe formation. Although it has a higher sensitivity than LM, LP is not an instantaneous technique because it takes a photographic process to obtain the moiré fringe image. In addition, because the magnification factor used in the LP during the fringe-viewing stage is lower than that used in the LM, the microstructure of specimen surface from the LP is not as clear as that from the LM.

5.5.3 Lithographic Grating and Total Imaging (LT)

In this method, a specimen is scanned twice, one under no loading and the other under loading or deformation, by the photograph scanner. The specimen then is subjected to etching. Both the initial specimen grating and the deformed specimen grating are created on the specimen surface. The total imaging, which is focused on the two specimen gratings - hence the moiré fringes generated by them - is used in the viewing stage. There is no limit on the magnification factor for the total imaging. The moiré fringes are, in fact, organized by the trenches (because of double scanning) located on the intersecting points of the trenches of these two gratings, as shown in Figure 5.3(a). The two possible moiré fringe patterns due to interference between these two gratings and the scanning for total imaging are not visible because the frequencies of these two gratings and the scanning rate for the total imaging are very different.

5.5.4 Carbonaceous Grating and Monitor Viewing (CM)

In this technique, a specimen is first scanned by the monitor scanner to produce carbonaceous gratings. In order to have a specimen grating with a high aspect ratio, the electron dosage should be carefully controlled. Based on the carbonaceous grating, the moiré fringe pattern can be formed when the specimen is subjected to loading or deformation and viewed by the monitor scanner. Again, an instantaneous or even dynamic image can be seen on the SEM monitor.

5.5.5 Carbonaceous Grating and Photograph Viewing (CP)

This method is based on forming a carbonaceous grating on the specimen by the monitor scanner of the SEM. Both the microstructure of the specimen surface and a moiré fringe pattern due to interference between the moiré grating and the photographic scanning can be obtained on a photograph. This method offers a higher sensitivity than the CM. However, it is not an instantaneous technique as the CM. Besides, the CP gives a poorer resolution of the microstructure of the specimen surface than the CM due to the smaller magnification factor used in photograph viewing. As in the LM, the LP and the CM, only a virtual moiré fringe pattern appears on the final image (on either an SEM monitor or a photograph). The moiré grating is not visible.

5.5.6 Carbonaceous Grating and Total Imaging (CT)

Two carbonaceous gratings are deposited on the specimen by scanning the specimen twice with the monitor scanner: one is the initial specimen grating and the other is the deformed specimen grating. The specimen is then subjected to SEM scanning for total imaging. Again, there is no magnification limit during the viewing stage. The image can be enlarged as much as possible. Besides, as in the LT, the real moiré fringe pattern is implicit. It is organized by the intersecting points of the two specimen gratings and requires a careful tracing for identification, as shown in Figure 5.3(b). However, one needs to note that the deformed specimen grating is not visible; neither are the fringes based on the interference between the two specimen gratings and the SEM viewing.

5.6 COMPARISON OF THE SIX SEM MOIRÉ METHODS

Based on grating producing techniques, the six SEM moiré methods can be divided into two groups: the lithographic grating group and the carbonaceous grating group. The former is based on the well-developed electron beam lithography. However, the lithographic technique is time-consuming and labor-intensive and can cause local reinforcement of testing specimens. The carbonaceous technique is newly developed and requires further research to become a well-controlled technique. However, it is more convenient than the lithographic technique.

Based on scanning/viewing techniques, the six SEM moiré methods can be divided into two groups, the monitor viewing and the photograph viewing. The total imaging is based on either monitor viewing or photograph viewing. Although there are some differences between the two viewing techniques, such as frequency, the primary difference is that the monitor viewing is of an instantaneous technique while the photograph viewing is a photographic technique. Since the photograph viewing has a higher scanning rate than the monitor viewing, it requires a smaller magnification to achieve an identical frequency. Accordingly, it gives a poorer resolution on the microstructure of specimen surface.

Based on the image of moiré fringes, the six SEM moiré methods can be divided into two groups, the fringe viewing and the total imaging, which include both speicmen gratings and moiré fringe patterns. Because of the significant difference in resolution between specimen gratings and moiré fringe pattern, the images based on monitor viewing and photograph viewing give only moiré fringe patterns. However, in total imaging, which is based on recording both the initial specimen grating and the deformation specimen grating, the moiré fringes must be identified by tracing the intersecting points of the two specimen gratings. Although the fringe-tracing procedure is not as simple as that based on fringe viewing, it provides an opportunity to increase sensitivity.

Based on the differences due to grating producing technique, scanning/viewing technique, and imaging technique, details of the six SEM moiré methods are given in Appendix B for comparisons.

5.7 DEMONSTRATIONS

Experiments based on the six SEM moiré methods were performed. The specimens used in the studies were either made of aluminum or epoxy. The aluminum specimens were coated with a PMMA layer and were used for the LM and LT cases.

specimens were first coated with a gold layer and then a PMMA layer. They were used in the LP, CM, CP and CT cases. Experimental results of moiré fringe patterns based on specimen rotation are given in figures 5.4-5.9. The comparison between the experimental results and analytical calculations based on Equation 2.4 are also presented:

$$\tan\theta = \frac{\sin\phi}{\cos\phi + \dfrac{p_f}{p_r}} \qquad (2.4)$$

where θ and ϕ are angles of specimen and moiré fringes with respect to the scanning lines, respectively, and p_f and p_r are pitches of moiré fringes and reference grating, respectively. The angles θ and ϕ are also shown in each figure. In all cases, the experiment results seem to agree very well with the analytical calculations.

5.8 CONCLUSIONS

The carbonaceous grating is much easier to prepare on testing specimens than the lithographic grating. In casting carbonaceous grating, there is no need to remove the specimens from SEM chambers as needed in the lithographic grating technique for chemical etching. Besides, the thickness of carbonaceous grating can be as thin as 4 nm, compared to the 100 nm usually used in the lithographic grating. Hence, the reinforcement effect on the specimens can be negligible. Although the carbonaceous grating has been verified to be a feasible technique, more studies are needed to improve its quality and increase its frequency.

Unlike the conventional moiré methods that only record moiré fringe patterns, the total imaging technique records both moire fringes patterns and moiré gratings. If two real moiré gratings, such as the initial specimen grating and the deformed specimen

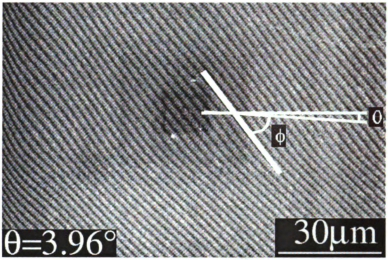

(a)

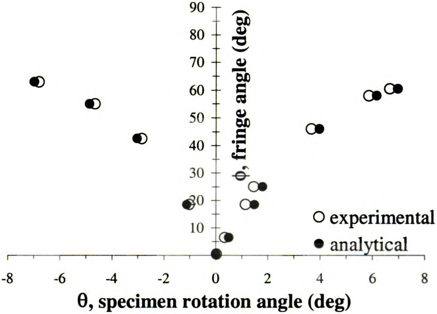

(b)

Figure 5.4(a) Moiré fringe pattern based on LM method. (b) Comparisons between analytical calculations and experimental measurements.

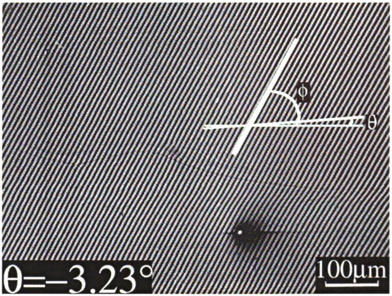

(a)

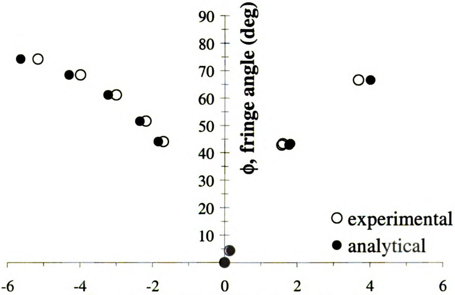

(b)

Figure 5.5(a) Moiré fringe pattern based on LP method. (b) Comparisons between analytical calculations and experimental measurements.

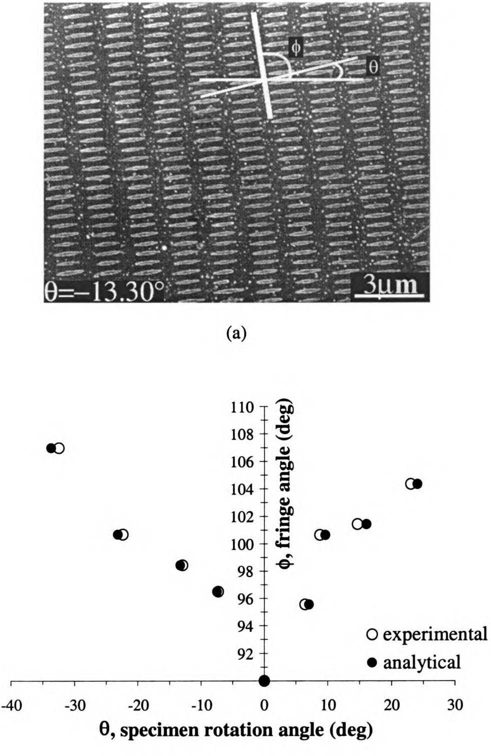

(a)

(b)

Figure 5.6(a) Moiré fringe pattern based on LT method. (b) Comparisons between analytical calculations and experimental measurements.

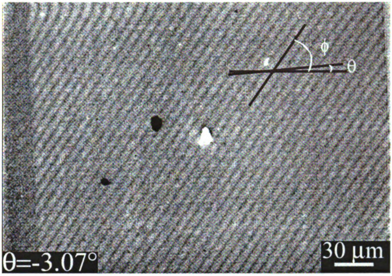

(a)

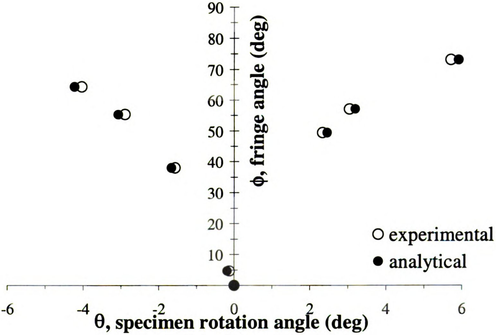

(b)

Figure 5.7(a) Moiré fringe pattern based on CM method. (b) Comparisons between analytical calculations and experimental measurements.

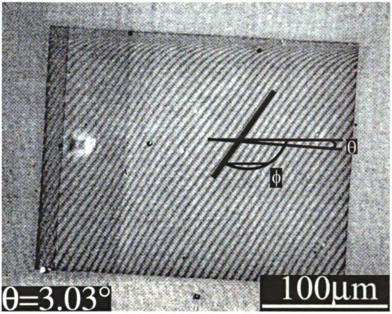

(a)

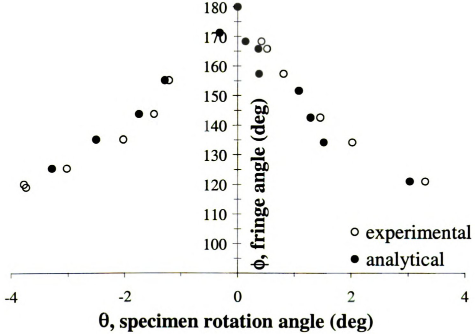

(b)

Figure 5.8(a) Moiré fringe pattern based on CP method. (b) Comparisons between analytical calculations and experimental measurements.

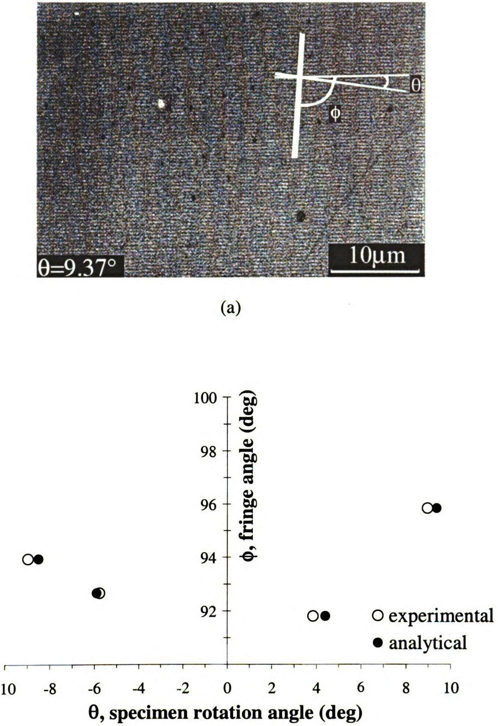

(a)

(b)

Figure 5.9(a) Moiré fringe pattern based on LT method. (b) Comparisons between analytical calculations and experimental measurements.

grating are cast on a specimen, a real moiré fringe pattern can be identified from tracing the intersecting points of two moiré gratings. Since the moiré fringe pattern is also a real image, there is no limit on magnification in total imaging. Hence, the sensitivity of a moiré method based on total imaging is only dependent on the frequency of the specimen grating. Since the frequency of the specimen grating can be made very high, such as 10,000 lines/mm, the moiré method based on total imaging can thus have a very high sensitivity.

Chapter 6

APPLICATIONS OF SEM MOIRÉ

6.1 INTRODUCTION

Carbon fiber composites and two-phase polymers served as model materials to demonstrate the applicability of newly developed SEM moiré methods to measure microscopic deformation. Two SEM moiré methods, carbonaceous grating and monitor viewing (CM) and carbonaceous grating and total imaging (CT), were applied to rotation angle measurements on carbon fiber reinforced composites. The composite specimens were able to carry carbonaceous gratings on their surface. The moiré fringe patterns and carbon fibers were observed simultaneously, which showed the feasibility of the SEM moiré methods for the investigation of micromechanics. The other application of the SEM moiré methods was the local strain measurement of each component in a two-phase polymer material. The interface shifting was observed during the stress relaxation experiment. The strain of the individual phase of this specimen did not remain constant when the global strain did. An energy loss may occur due to this interface shifting, which results in the deviation of the analytical calculation from the experimental data. Therefore, the viscoelastic response of the two-phase polymer specimens was investigated. The dynamic mechanical tests were conducted on the specimens with different volume fractions in parallel and serial loading configurations. The analytical calculations based on the rule of mixtures do not predict the dynamic experimental testing data of two-phase polymers in serial loading configuration. On the other hand, the dynamic experimental testing data of specimens in parallel loading configuration match very well with the analytical calculation.

The above applications of the SEM moiré method reveal the importance of getting the microscopic observation and deformation measurement simultaneously.

6.2 CARBON FIBER REINFORCED COMPOSITES

6.2.1 Experimental Procedures

A. Materials and Specimen Preparation

The material used in this study was a $[0^\circ/90^\circ]_s$ laminated carbon fiber/epoxy composite. The composite material was cut into several 5mm by 5mm specimens. They were polished culminating with 0.05 μm alumina particles and then coated with a thin layer of gold on the polished surfaces. Specimens were kept in the normal laboratory environment prior to the deposition of carbonaceous gratings.

B. Grating Deposition and Verification

Two SEM moiré methods, carbonaceous grating and monitor viewing (CM) and carbonaceous grating and total imaging (CT), were applied to composite specimens. Direct carbonaceous grating deposition was carried out under a CamScan 44FE scanning electron microscope. After gun alignment and focusing, a desired electron beam current of 1.7 nA was obtained. The SEM settings were the following:

Acceleration voltage:	15 keV	Beam aperture:	50 μm
First condenser lens (C1):	6.24 mV	Spot size:	9
Second condenser lens (C2):	1.48 mA	Working distance:	23 mm
Objective lens (C3):	0.71 mA	Electron beam current:	1.7 nA

Then, composite specimens used for SEM moiré CM method were under direct electron beam scanning for 8 minutes at the magnification factor 500 to deposit carbonaceous grating with a frequency of 2774 lines/mm on specimen surfaces.

After deposition, scan coils were rotated an angle with respect to composite specimens while the magnification factor remained unchanged, and the moiré fringe patterns were recorded accordingly. Since the SEM settings were not altered before and after the grating deposition, a null field of a moiré fringe pattern was observed before scan coils were rotated. If the magnification factor changed to 480, carrier fringes would be observed. Based on this magnification factor, another set of moiré fringe patterns, with carrier fringes as initial fringes, was recorded as well at various rotation angles.

For the SEM moiré CT method, five gratings were deposited onto the surface of composite specimens with same grating orientation first. Then, the second grating was deposited on one of the five previous gratings areas after the scan coils were rotated an angle with respect to specimens. Five rotations were made during this experiment.

6.2.2 Analytical Calculation

The Equation 2.4 was used for analytical calculation in both CM and CT methods:

$$\tan\theta = \frac{\sin\phi}{\cos\phi + \frac{p_f}{p_r}} \tag{2.4}$$

where θ and ϕ are angles of specimen and moiré fringes with respect to the scanning lines, respectively, and p_f and p_r are pitches of moiré fringes and reference grating, respectively.

6.2.3 Discussion

Figure 6.1 and 6.2 show the moiré fringe patterns along with rotation angles from CM method at two different frequencies of reference grating: 2778 lines/mm and 2667 lines/mm respectively. Figure 6.3 shows the moiré fringe patterns from CT method with a frequency of 2774 lines/mm as a reference grating. In all cases, the experiment results

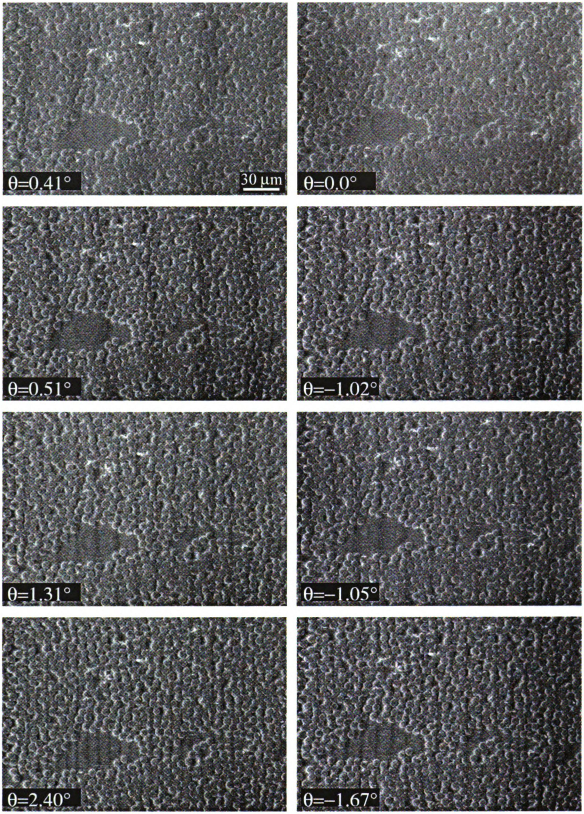

Figure 6.1 Moiré fringe patterns at various rotation angles on carbon fiber reinforced composite based on CM method. The frequency of reference grating is 2778 lines/mm.

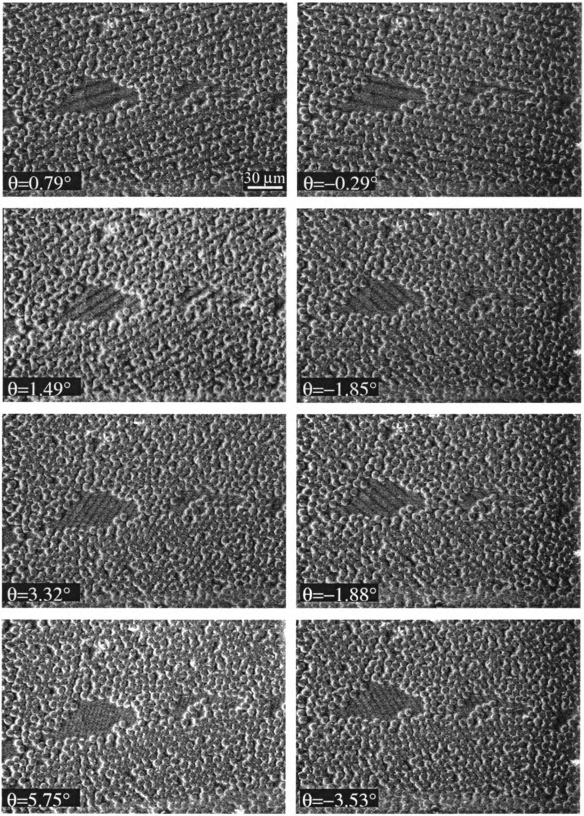

Figure 6.2 Moiré fringe patterns at various rotation angles on carbon fiber reinforced composite based on CM method. The frequency of reference grating is 2667 lines/mm.

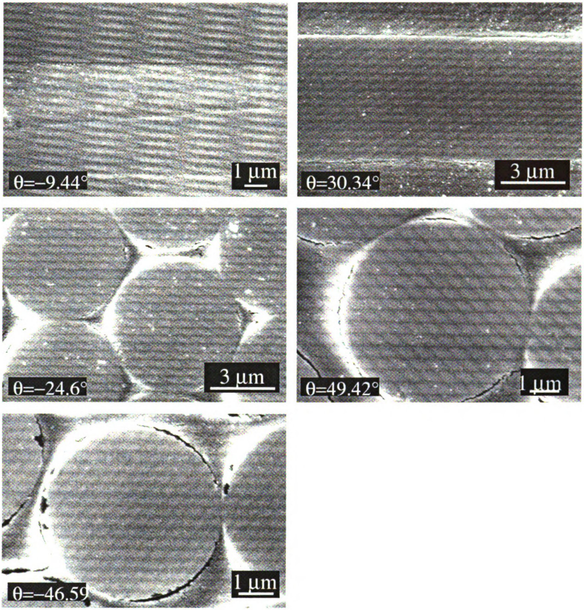

Figure 6.3 Moiré fringe patterns at various rotation angles on carbon fiber reinforced composite based on CT method. The frequency of reference grating is 2774 lines/mm.

seem to agree very well with the analytical calculations as shown in Figure 6.4 and Figure 6.5 for CM and CT methods respectively. Based on the above demonstration, this carbonaceous grating technique can be applied to polymer matrix composite materials. The deformation measurement of composite materials under loading is feasible but needs further investigation.

6.3 INTERFACE SHIFTING OF TWO-PHASE POLYMERS

6.3.1 Experimental Procedures

A. Materials and Specimen Preparation

The epoxy resin for this application was di-functional pure diglycidyl ether of bisphenol A (DGEBA) (DER332, Dow Chemical USA). Amine terminated poly(propylene oxide) with two different molecular weights, i.e. JEFFAMINE D230 and JEFFAMINE D400 (Huntsman, USA), were used to crosslink epoxy resin, DGEBA. Their chemical structures are shown in Figure 6.6.

The molar ratio of epoxide to amine was stoichiometric when mixing DGEBA with the JEFFAMINE D series. The weight fraction of epoxy and diamines were the following: DGEBA:D230 = 0.7473:0.2527 and DGEBA:D400 = 0.6734:0.2266. DGEBA (366.9g) was first mixed with JEFFAMINE D230 (124.1g) and cured at 100°C for 24 hours and then kept in the oven for slow cooling to room temperature. This cured DGEBA/D230 epoxy (Material E) was immersed into a mixture of DGEBA (133.6g) and JEFFAMINE D400 (78.6g) (Material F). Then Material E and F were cured in an oven at 100°C for 24 hours and kept in the oven to cool down to room temperature.

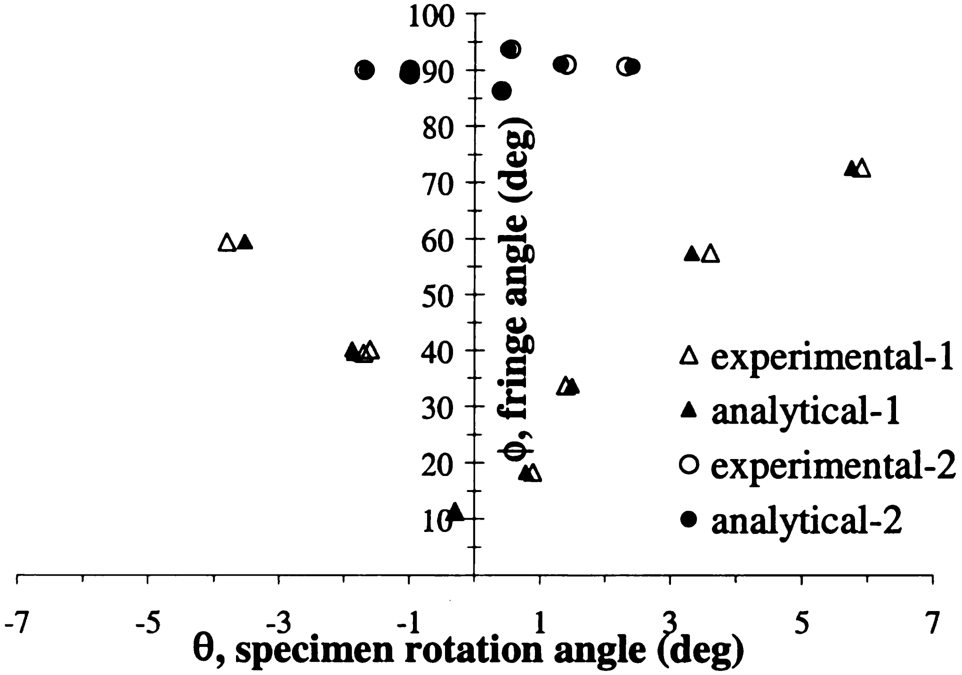

Figure 6.4 Comparisons between analytical calculations and experimental measurements based on CM method. Specimen is carbon fiber reinforced composite.

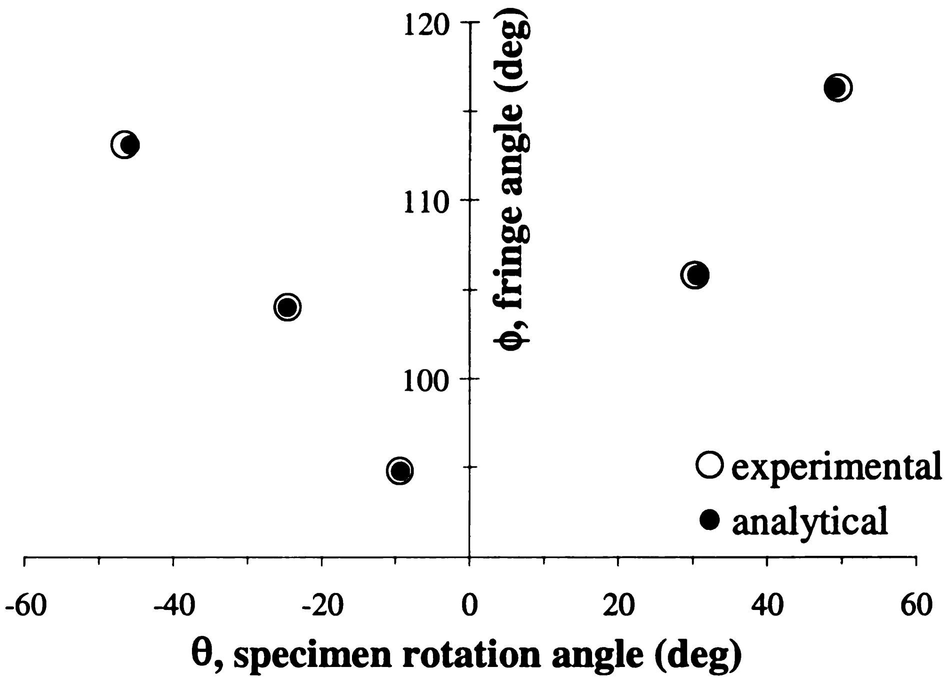

Figure 6.5 Comparisons between analytical calculations and experimental measurements based on CT method. Specimen is carbon fiber reinforced composite.

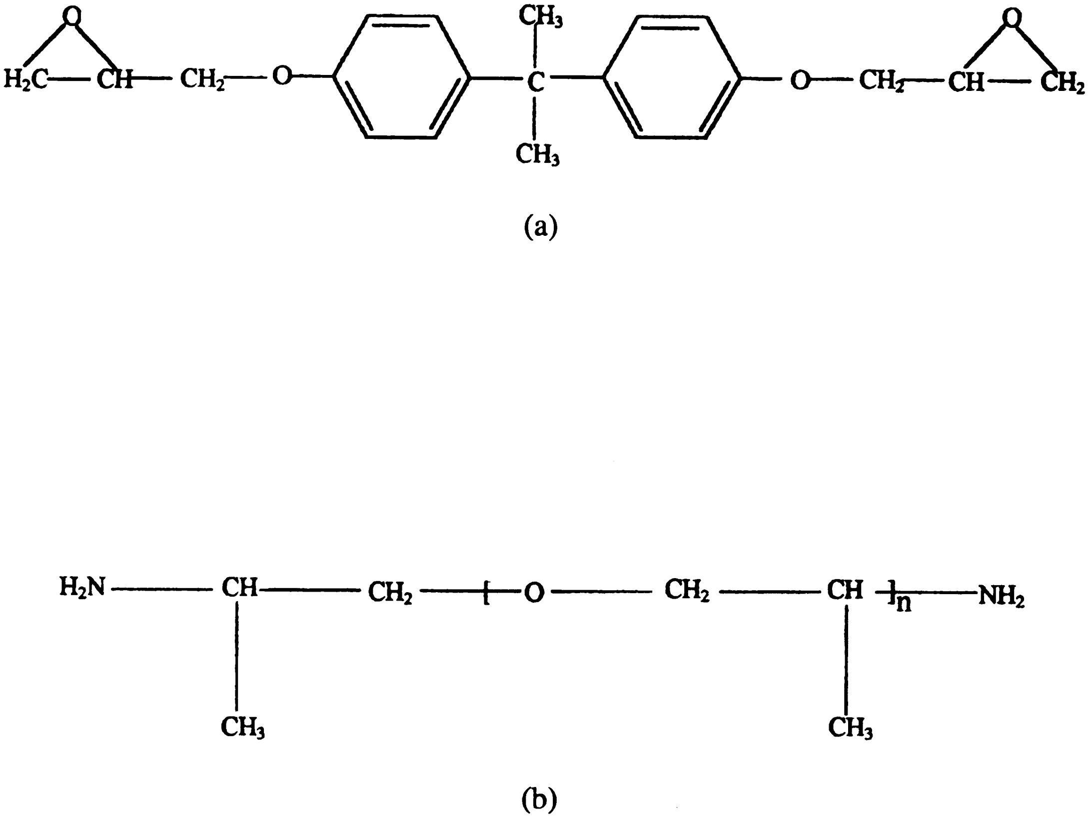

Figure 6.6 Molecular structure of (a) diglycidyl ether of bisphenol A (DGEBA) and (b) polyoxypropylenediamine (JEFFAMINE D-230 where n=2.6, JEFFAMINE D-400 where n=5.6).

This two-phase polymer was milled into a dog-bone-shaped specimen and was drilled one hole with 3/32 inch in diameter at each end. The specimen consisted of 50.30% volume fraction of Material E and 49.70% volume fraction of Material F in serial loading configuration. The cross section area of the specimen was 6.41 mm^2 (1.75 mm by 3.37 mm) with the gage length of 10.64 mm. The interface of Material E and F was around the middle of the gage section.

The specimen was polished culminating with 0.05 μm alumna particles. It was immersed in distilled water subjected to ultrasonic cleaning for 30 minutes and was blown dry with clean air. Then the specimen was annealed at 100°C for 1 hour and kept in the oven to cool down to room temperature before being coated with a thin layer of gold. The specimens were kept in the normal laboratory environment prior to grating deposition.

B. Testing Method

An SEM testing stage (Fullmam USA) was installed in the SEM chamber, and the specimen was held at each end by two pins with diameter of 3/32 inch. The specimen grips were controlled by a screw-driven motor with a resolution of 0.001 inch. The force was measured by a load cell with a resolution of 0.1 lb.

For local displacement measurement, the SEM moiré CM method was used in this application. The carbonaceous grating with a frequency of 2778 lines/mm was deposited onto the specimen surface at the interface of Material E and F.

A stress relaxation experiment was conducted in the SEM chamber. A constant grip distance of 0.031 inch was applied to the specimen, which yielded to a strain of 7.40% resulting in a loading of 29.5 lb, which was a stress of 2969 psi (20.47 MPa).

Then, moiré fringe patterns as well as the forces were recorded accordingly.

C. Results

The local displacement was measured both from the shifting distance of the interface and moiré fringe patterns while the grip distance was kept constant during the stress relaxation experiment. The shifting distance of the interface was measured from the interface position based on the SEM images. Figure 6.7 shows the strain of Material E and F measured from the shifting distance of interface and the moiré fringe patterns during the stress relaxation experiment. Accordingly, the local strain did not remain constant on either Material E or Material F. Even though the global strain was kept constant for the stress relaxation experiment.

6.3.2 Analytical Calculation

Since the local strain of Material E and F had changed during the stress relaxation experiment for the two-phase polymer specimen in serial loading configuration, quasi-elastic analysis was not valid. Therefore, by assuming that the linear viscoelastic theory holds, the Boltzmann superposition integral was utilized to analyze this two-phase polymer specimen. For this specimen the local strain of Material E and of Material F was presented in terms of individual relaxation modulus and volume fractions. The detailed derivation is shown in Appendix C.

The individual relaxation modulus of Material E and F was obtained from the dynamic experimental data by a computer program [61]. This computer program written by Bradshaw and Brinson utilized a Prony exponential series to curve fit the dynamic experimental data (storage and loss modulus) within the frequency domain. Then, inverse Fourier transformed the Prony exponential series to the relaxation modulus. Both relaxation moduli of Material E and F were used to calculate their local strain for this two-phase polymer specimen. The results are plotted in Figure 6.7.

6.3.3 Discussion

The measurements from the SEM moiré method and the interface shifting show the similar results. Accordingly, the SEM moiré method was a useful and reliable tool to measure local deformation.

This interface shifting of the specimen during the stress relaxation experiment might result in additional energy loss for the specimen. A simple analytical calculation, such as the rule of mixtures, did not encounter this energy loss. It is of interest to study the effect of this additional energy loss due to the mismatch of the viscoelastic response of two linear viscoelastic materials.

6.4 MISMATCH OF VISCOELASTIC RESPONSE OF TWO-PHASE POLYMERS

6.4.1 Experimental Procedures

A. Materials and Specimen Preparation

The material used in this study was identical to the one in previous application. This two-phase epoxy material was cut to several 6 mm x 25 mm x 2 mm strips consisting of different volume fractions of Material E and F. The specimens were grouped into parallel and serial specimens depending on their loading direction. Both 100 percent of Material E and F were also cut from the same two-phase epoxy material. Therefore, there were nine different specimens for dynamic mechanical testing. Each specimen was polished with #1200 sand paper on both sides, annealed at 100°C for one hour, and cooled down to room temperature in an oven. Each specimen was kept at room

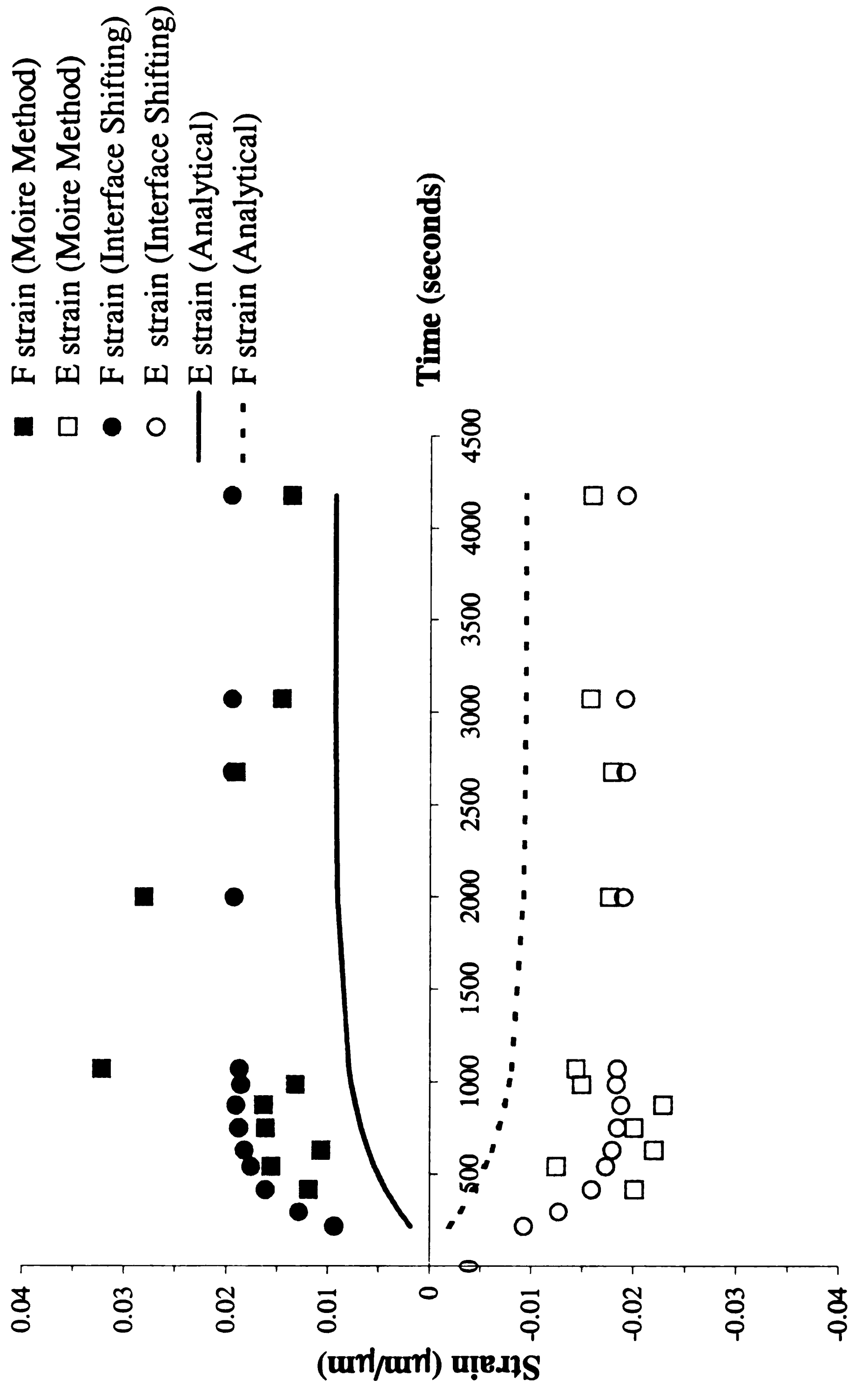

Figure 6.7 Comparisons of strain obtained from the SEM moiré method, from interface position, and from analytical calculation.

temperature for about two hours to maintain a similar initial aging condition prior to the dynamic mechanical thermal analysis (DMTA).

B. Testing Method

TA Instrument DMTA 2980 was used to carry out frequency sweep experiments at each different temperature with displacement amplitude of 10 μm. The data were collected at 61Hz, 37Hz, 23Hz, 14Hz, 8.5Hz, 5Hz, 3Hz, 2Hz, 1Hz, 0.7Hz, and 0.45Hz. The temperature steps were from 20°C to 115°C with 5°C intervals. The forces, amplitudes of deformation and phase angles were measured during the experiments. Along with calibration constants, forces and amplitudes were used with the phase angles to calculate the storage and loss modulus.

C. Results

Frequency-temperature superposition was applied to dynamic experimental data to construct a master curve for each specimen at the reference temperature of 25°C. Figures 6.8 and 6.9 represent the master curves of storage modulus of specimens in parallel and serial loading configurations, respectively. Figures 6.10 and 6.11 represent the master curves of tanδ of specimens in parallel and serial loading configurations, respectively. The shift factor is plotted in Figure 6.12.

Frequency-temperature superposition was still applicable to the dynamic mechanical testing data with different loading configurations and different volume fractions of these two-phase polymer specimens. Therefore, these specimens were thermorheologically simple materials, so that the linear viscoelastic theory was applicable to them.

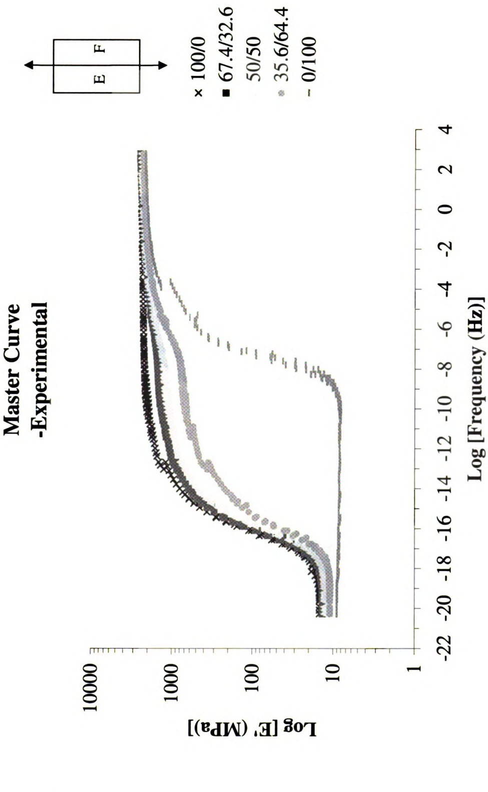

Figure 6.8 Master curves of storage modulus from experimental data. Specimens are in parallel loading configuration with various volume fractions.

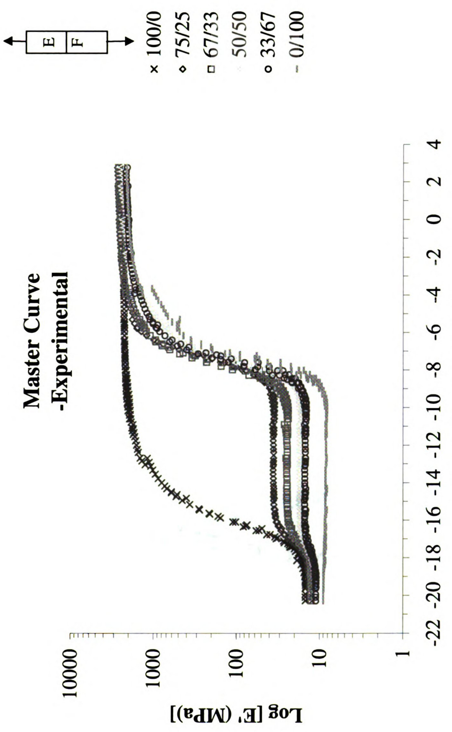

Figure 6.9 Master curves of storage modulus from experimental data. Specimens are in serial loading configuration with various volume fractions.

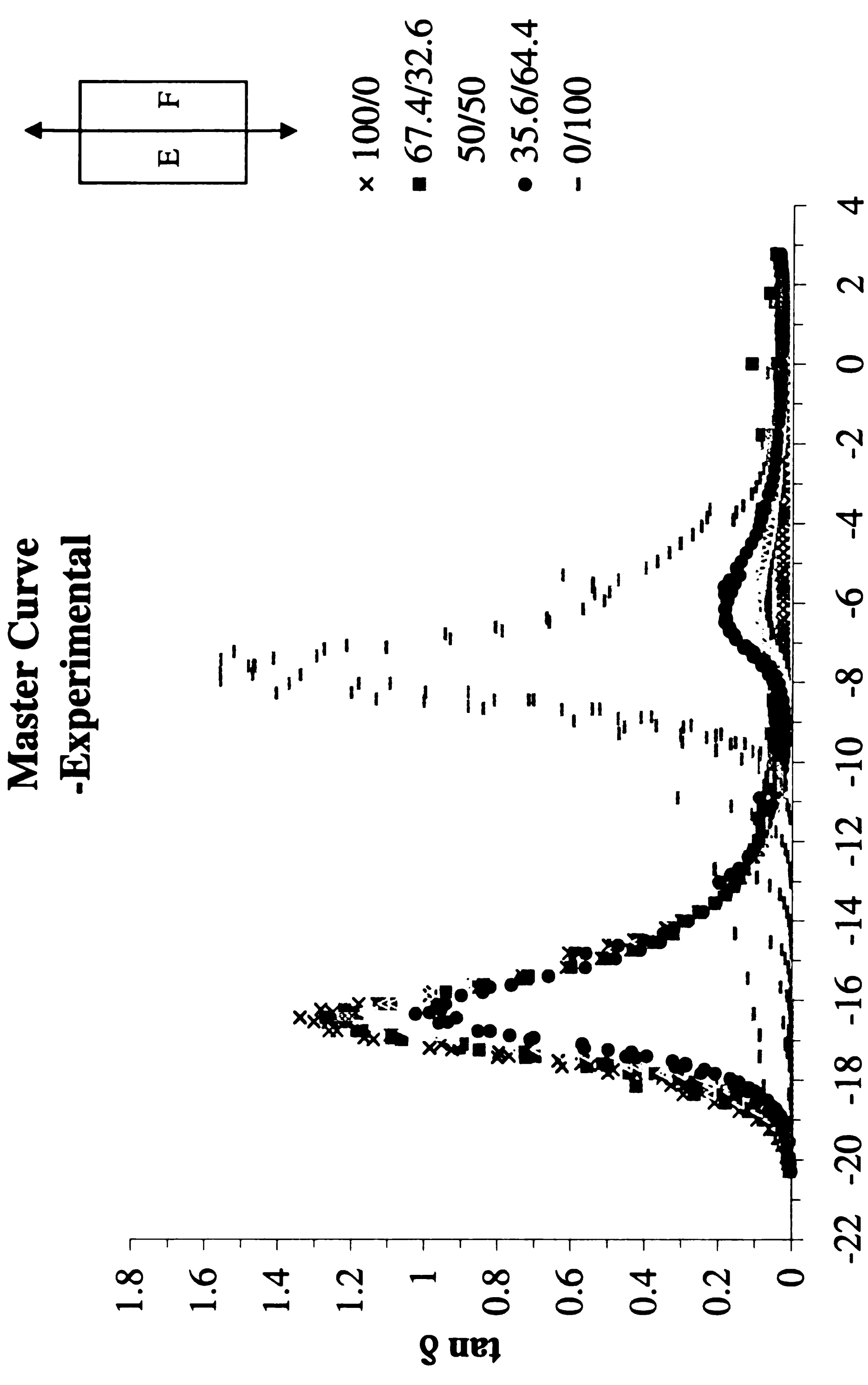

Figure 6.10 Master curves of tanδ from experimental data. Specimens are in parallel loading configuration with various volume fractions.

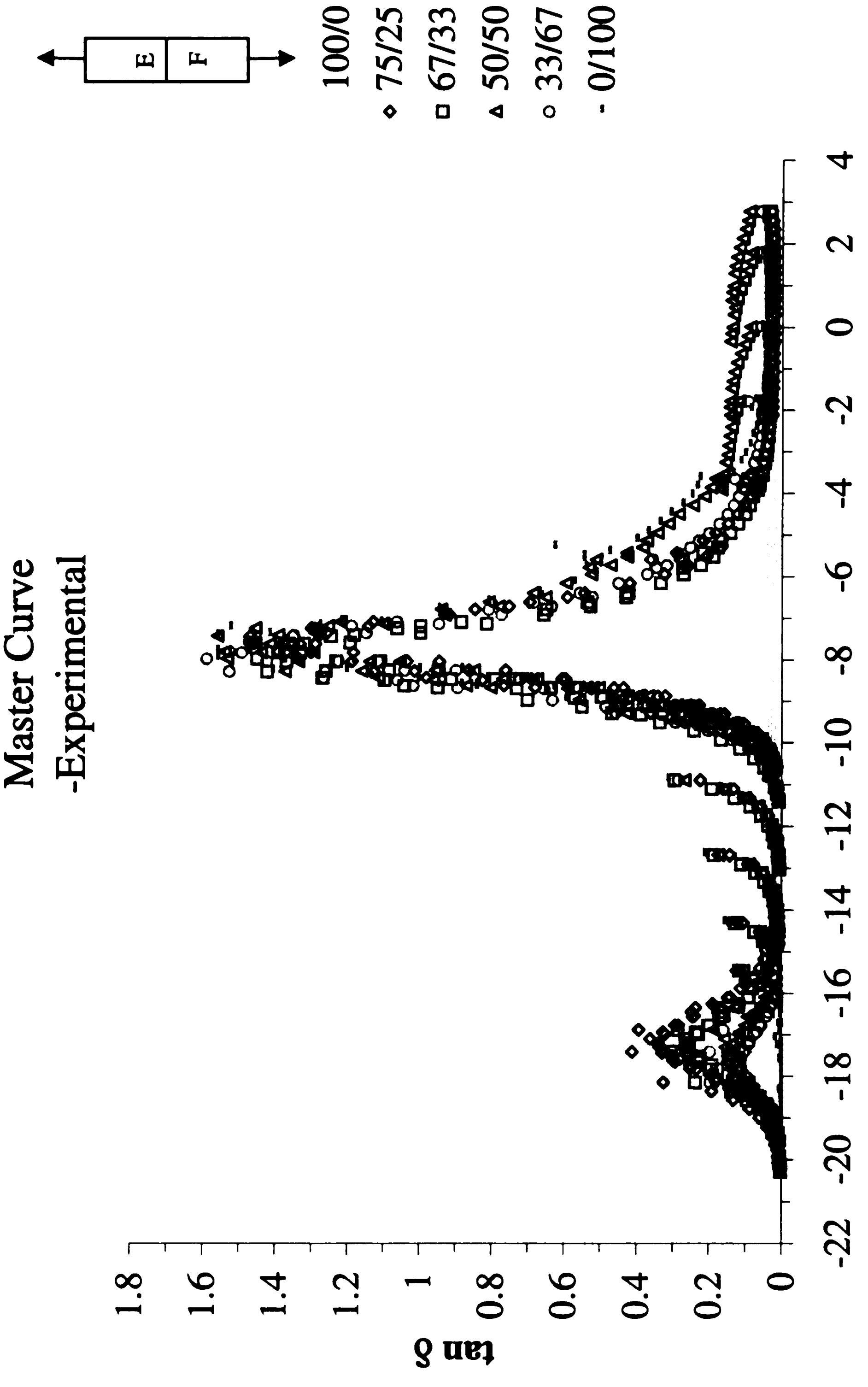

Figure 6.11 Master curves of tanδ from experimental data. Specimens are in serial loading configuration with various volume fractions.

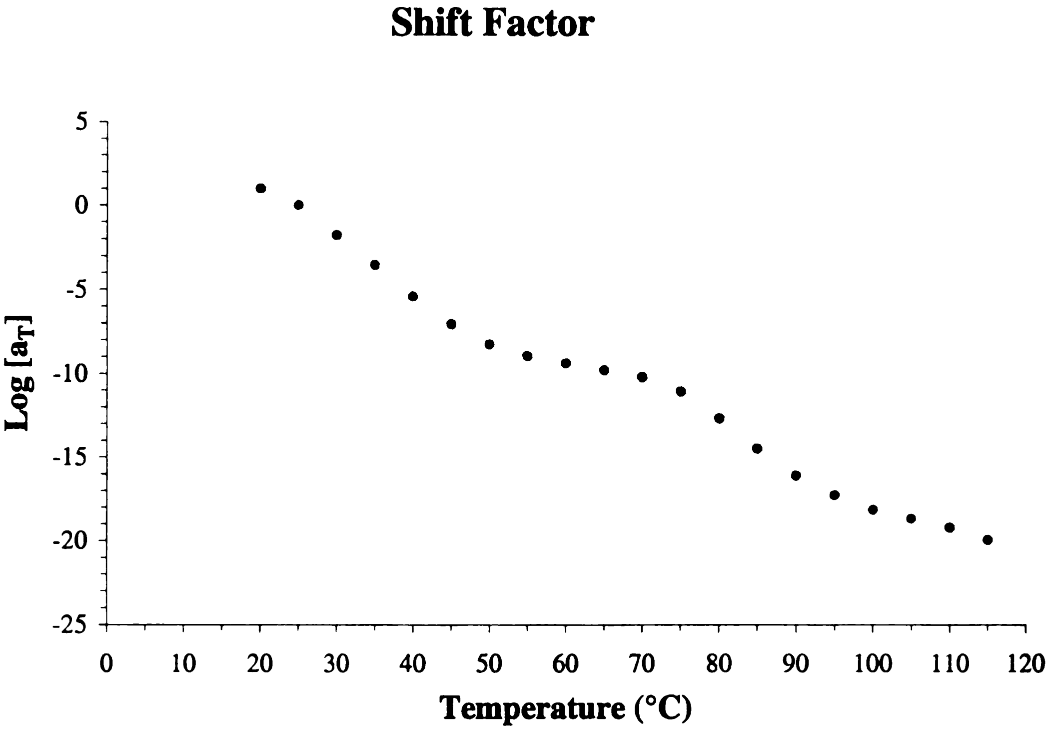

Figure 6.12 Shift factor at the reference temperature of 25°C.

However, the tanδ peak of Material E in the specimens in serial loading configuration was shifted toward a lower frequency compared with 100 percent of Material E. For those specimens in parallel loading configuration, tanδ peak of Material F shifted toward a higher frequency.

The area under tanδ peak in dynamic experimental data is usually considered as the damping energy of the material. Apparently, Material F dominated the energy absorption during the dynamic mechanical test of the specimens in serial loading configuration regardless of their volume fractions. Similarly, the volume fractions of Material E do not alter the energy absorption of the specimens in parallel loading configuration.

6.4.2 Analytical Calculation

The rule of mixtures was applied to calculate the analytical solution of these two-phase polymer specimens at various volume fractions based on the dynamic mechanical testing data of 100 percent of Material E and F. The detailed derivation is shown in Appendix D. The storage modulus, loss modulus, and tanδ of these two-phase polymer specimens in serial and parallel loading configuration could be calculated based on the experimental data of 100% Materials E and F and their volume fractions from the following equations:

$$\begin{aligned} E^{P}{'} &= V^{E}E^{E}{'} + V^{F}E^{F}{'} \\ E^{P}{''} &= V^{E}E^{E}{''} + V^{F}E^{F}{''} \\ \tan\delta^{P} &= \frac{V^{E}E^{E}{''} + V^{F}E^{F}{''}}{V^{E}E^{E}{'} + V^{F}E^{F}{'}} \end{aligned} \tag{6.1}$$

$$\begin{aligned}
\frac{E^{S\prime}}{\left|E^{S^*}\right|} &= V^E \frac{E^{E\prime}}{\left|E^{E^*}\right|} + V^F \frac{E^{F\prime}}{\left|E^{F^*}\right|} \\
\frac{E^{S\prime\prime}}{\left|E^{S^*}\right|} &= V^E \frac{E^{E\prime\prime}}{\left|E^{E^*}\right|} + V^F \frac{E^{F\prime\prime}}{\left|E^{F^*}\right|} \\
\tan\delta^S = \frac{E^{S\prime\prime}}{E^{S\prime}} &= \frac{V^E \dfrac{E^{E\prime\prime}}{\left|E^{E^*}\right|} + V^F \dfrac{E^{F\prime\prime}}{\left|E^{F^*}\right|}}{V^E \dfrac{E^{E\prime}}{\left|E^{E^*}\right|} + V^F \dfrac{E^{F\prime}}{\left|E^{F^*}\right|}}
\end{aligned} \tag{6.2}$$

where E', E'', and $\tan\delta$ represented the dynamic mechanical properties of two-phase polymer specimens. The superscript "p" and "s" represent the specimens in parallel and serial loading configuration, respectively. The superscript "E" and "F" represent the specimens of Materials E and F, respectively. V^E and V^F are the volume fraction of Material E and F in these two-phase polymer specimens, respectively.

The storage modulus and tanδ for each specimen with different volume fractions in parallel and serial loading configurations are calculated from those of 100 percent of Materials E and F by using Equation 6.2 and 6.3 and the calculated results are plotted in figures 6.13-6.16.

6.4.3 Discussion

The comparisons of the experimental data and the analytical calculation for each specimen are shown in figures 6.17-6.30. These figures show that the analytical calculation is in a good agreement with experimental data of storage modulus, loss modulus, and tanδ in parallel loading configuration as well as storage modulus in serial loading configuration. The rule of mixtures does not predict well the experimental data of loss modulus and tanδ in a serial loading configuration.

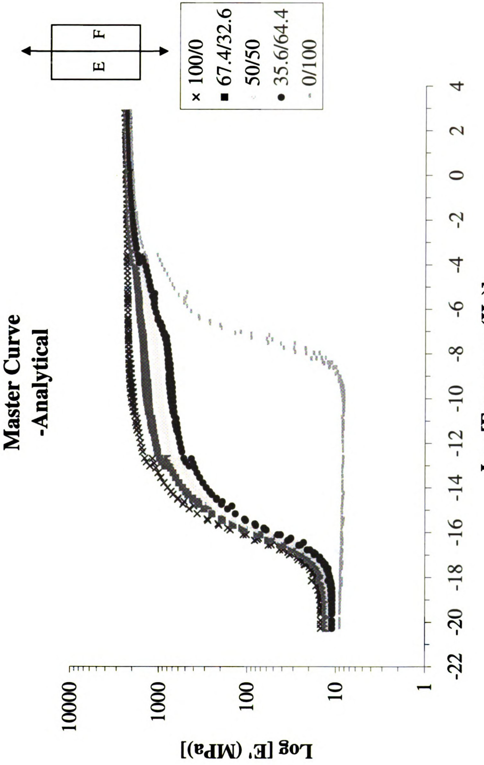

Figure 6.13 Master curves of storage modulus from analytical calculation based on parallel loading configuration and various volume fractions.

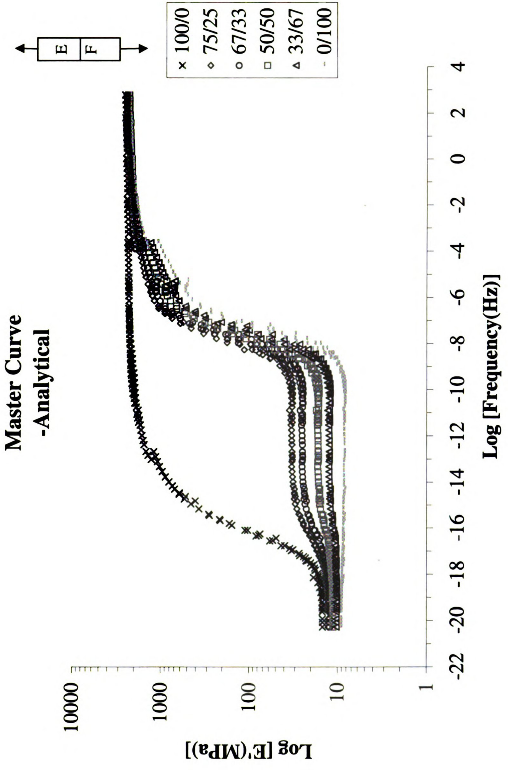

Figure 6.14 Master curves of storage modulus from analytical calculation based on serial loading configuration and various volume fractions.

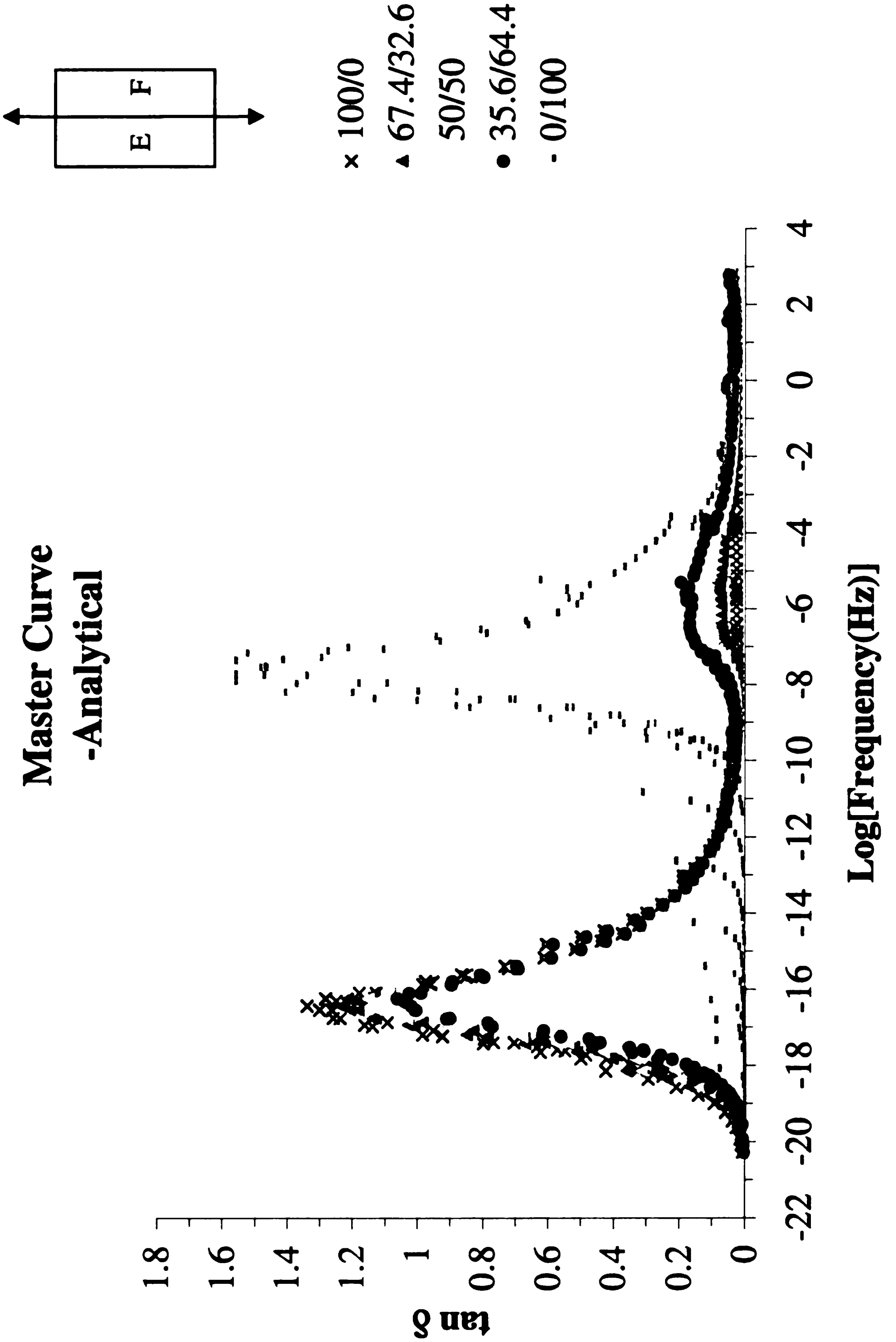

Figure 6.15 Master curves of tanδ from analytical calculation based on parallel loading configuration and various volume fractions.

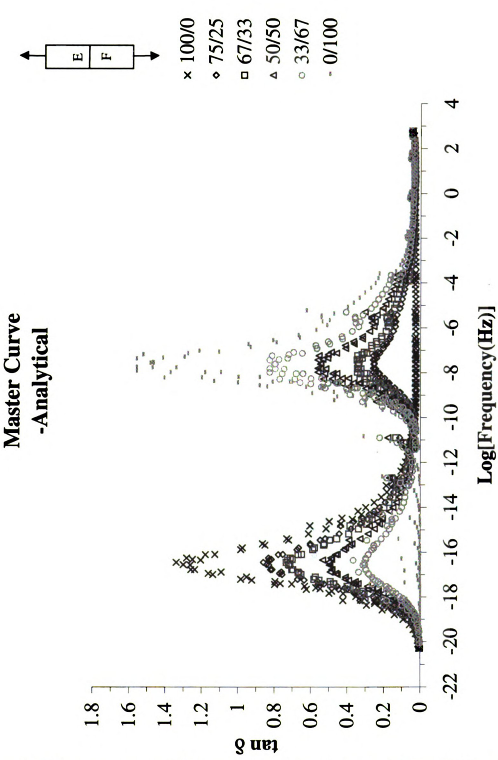

Figure 6.16 Master curves of tanδ from analytical calculation based on serial loading configuration and various volume fractions.

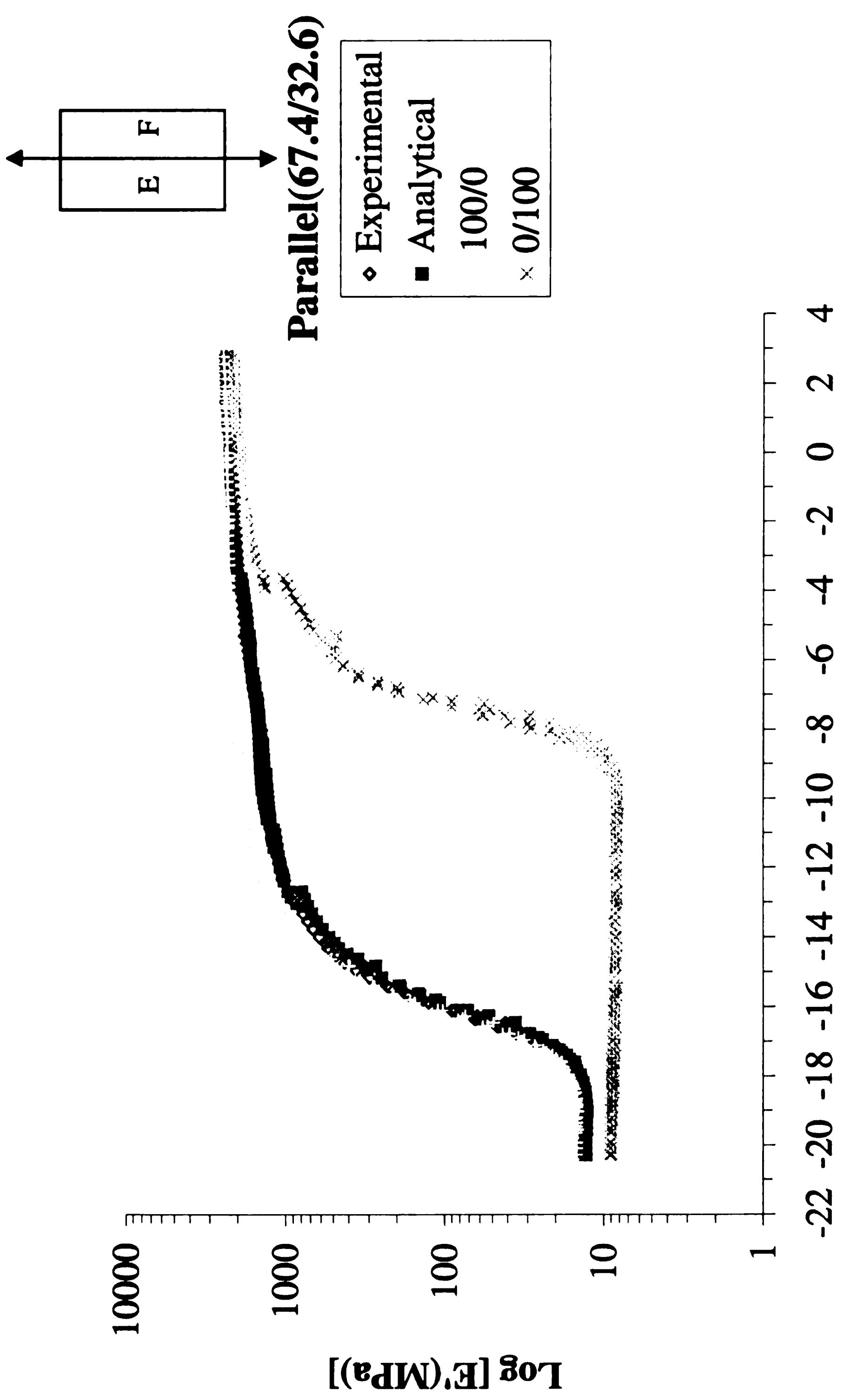

Figure 6.17 Comparison of experimental data and analytical calculation in master curve of storage modulus. Specimen is in parallel loading with volume fraction (E/F)= 67.4/32.6.

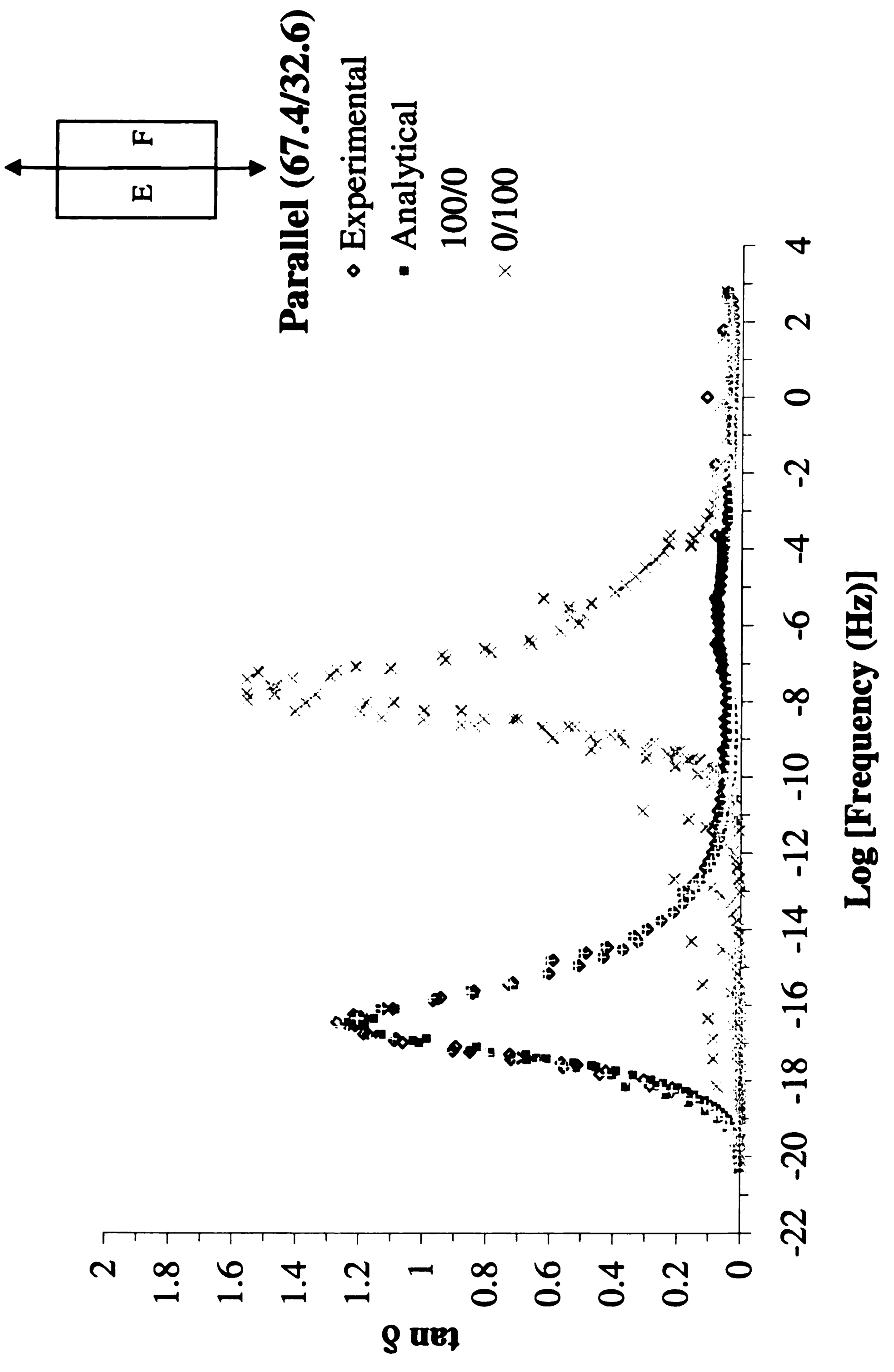

Figure 6.18 Comparison of experimental data and analytical calculation in master curve of tanδ. Specimen is in parallel loading with volume fraction (E/F)= 67.4/32.6.

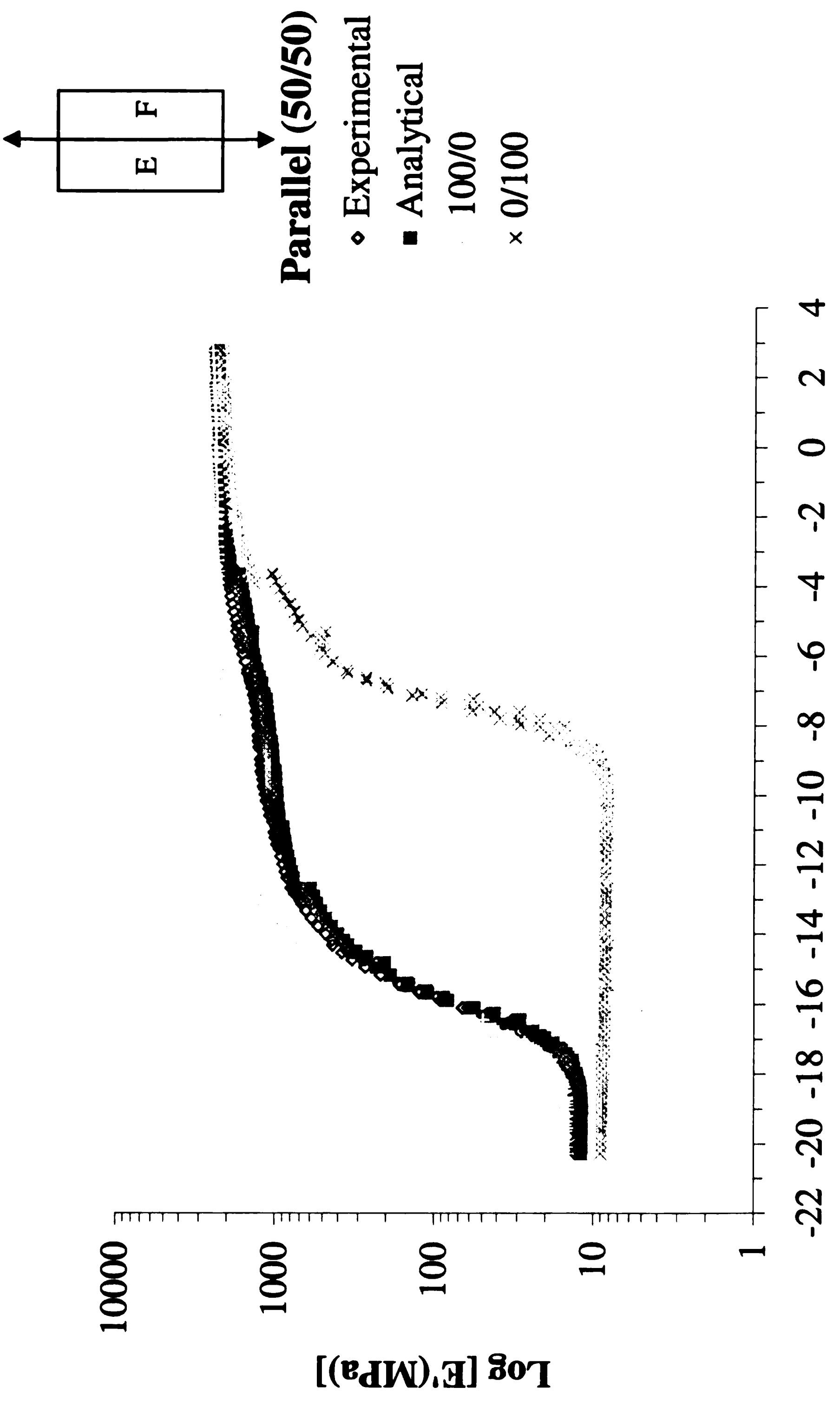

Figure 6.19 Comparison of experimental data and analytical calculation in master curve of storage modulus. Specimen is in parallel loading with volume fraction (E/F)=50/50.

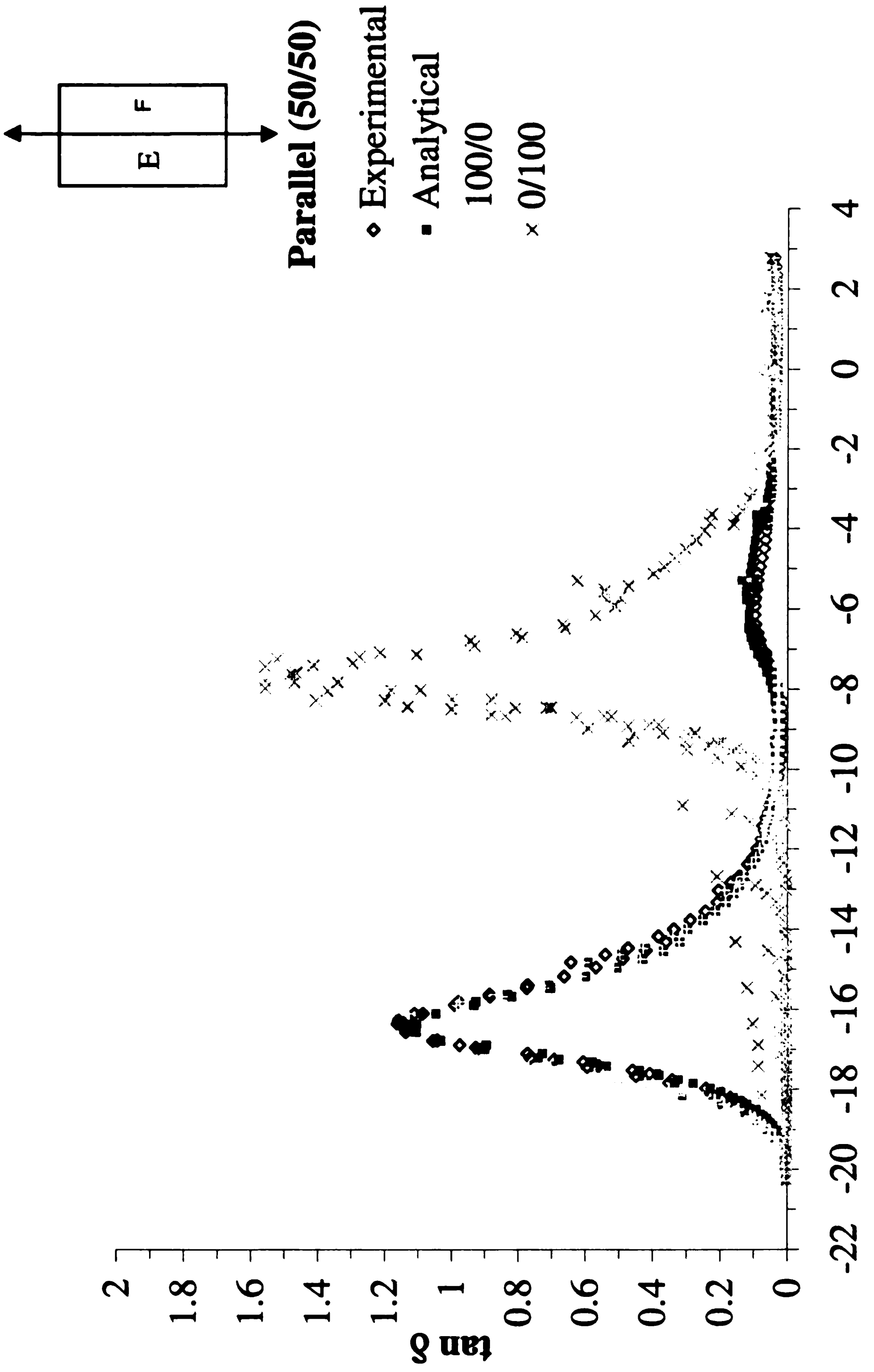

Figure 6.20 Comparison of experimental data and analytical calculation in master curve of tanδ. Specimen is in parallel loading with volume fraction (E/F)=50/50.

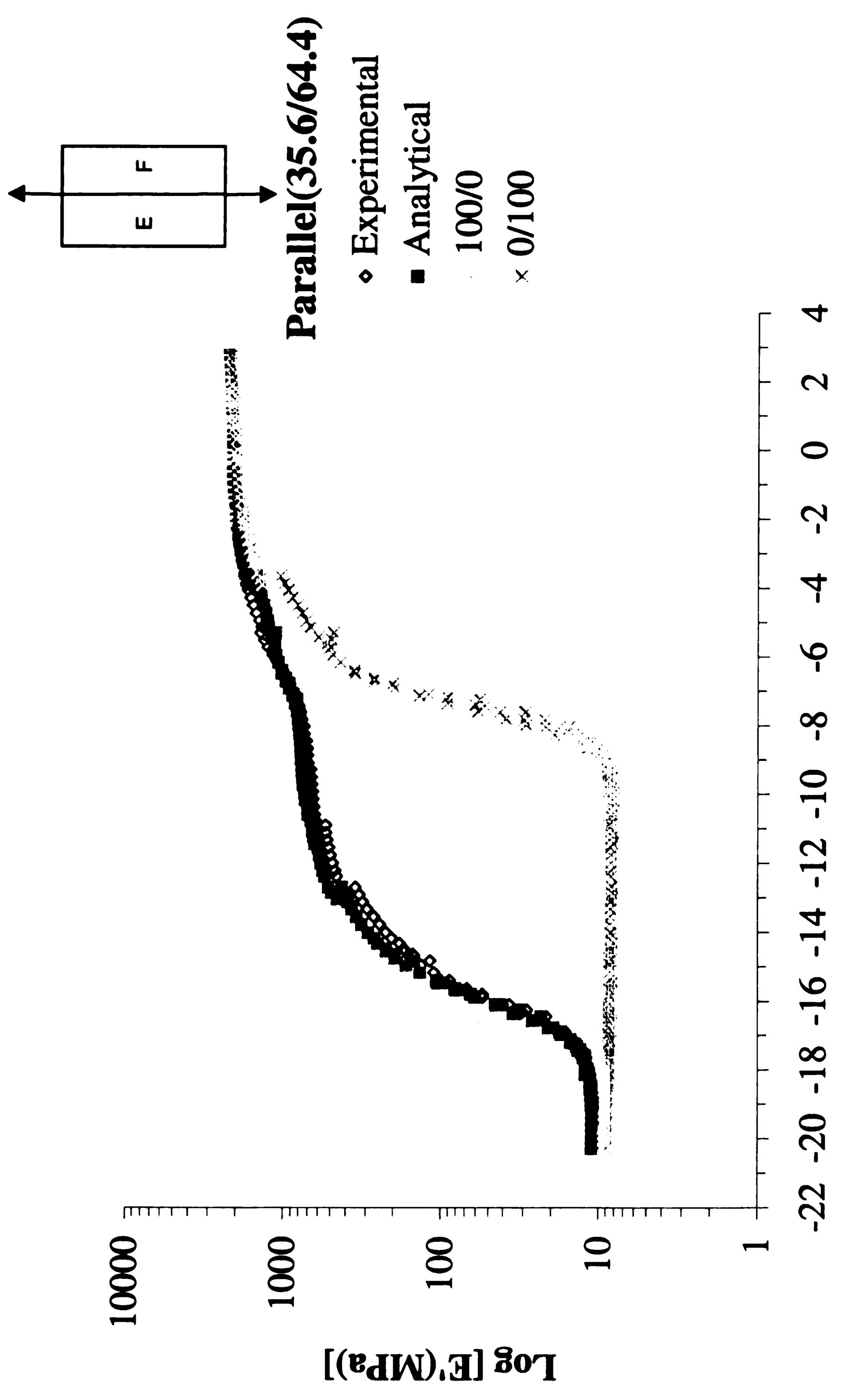

Figure 6.21 Comparison of experimental data and analytical calculation in master curve of storage modulus. Specimen is in parallel loading with volume fraction (E/F)=35.6/64.4.

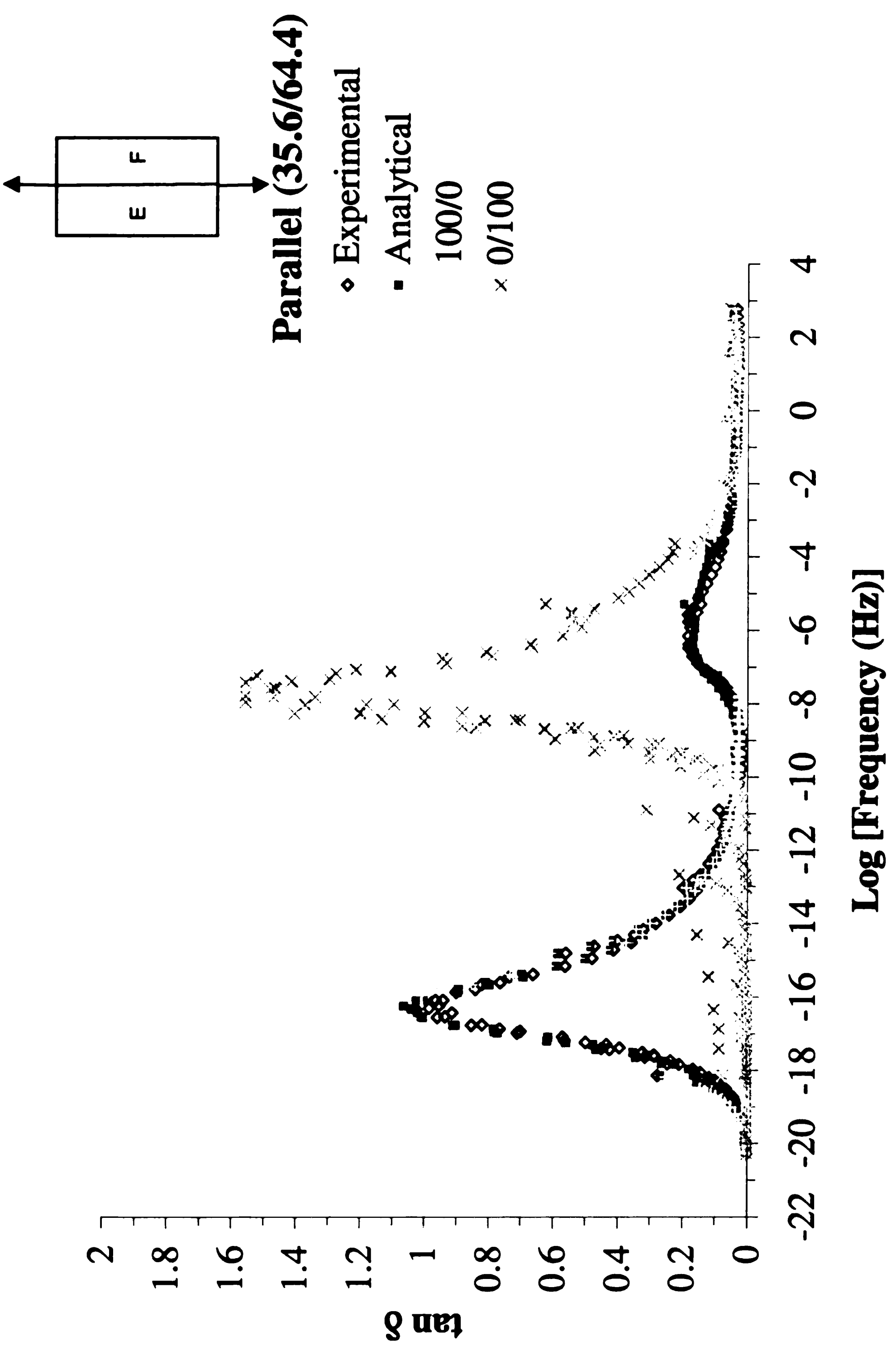

Figure 6.22 Comparison of experimental data and analytical calculation in master curve of tanδ. Specimen is in parallel loading with volume fraction (E/F)=35.6/64.4.

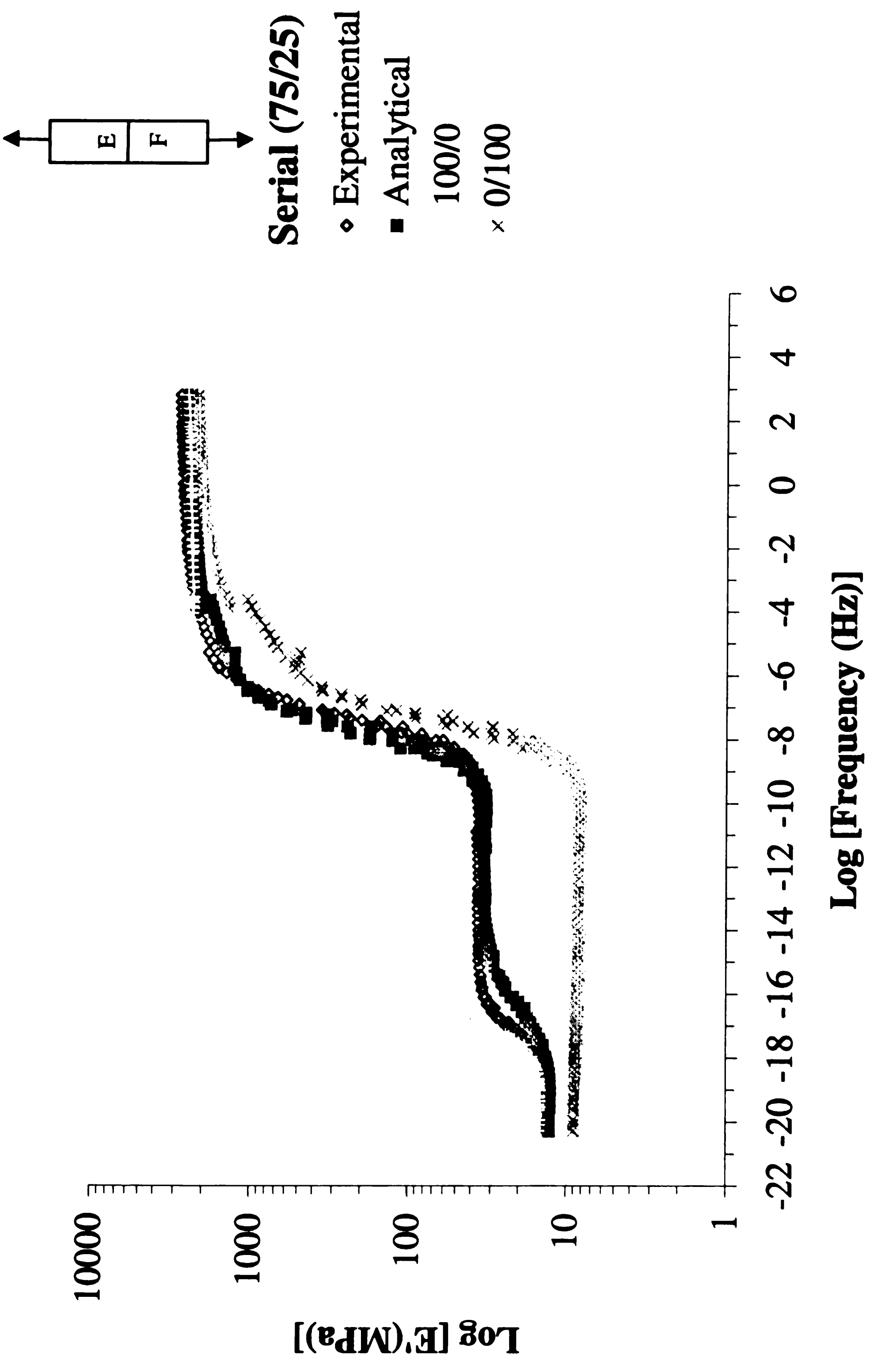

Figure 6.23 Comparison of experimental data and analytical calculation in master curve of storage modulus. Specimen is in series loading with volume fraction (E/F)=75/25.

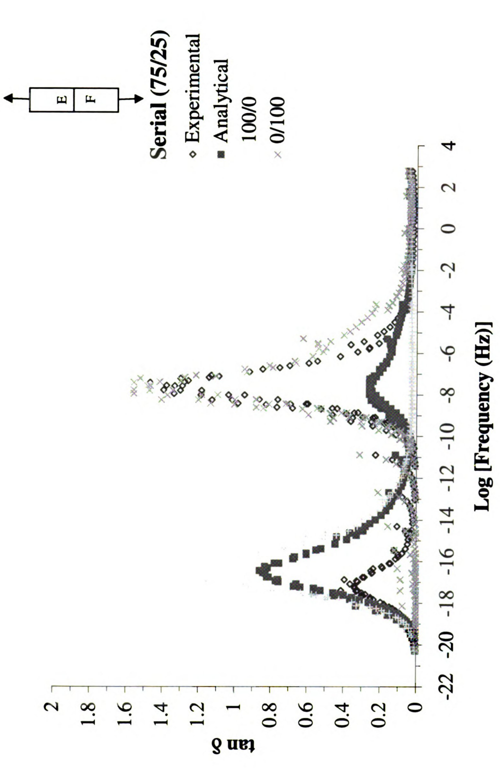

Figure 6.24 Comparison of experimental data and analytical calculation in master curve of tanδ. Specimen is in series loading with volume fraction (E/F)=75/25.

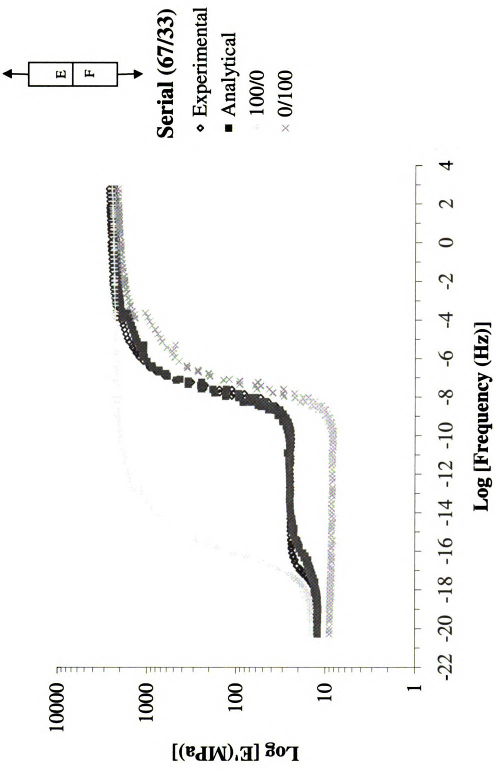

Figure 6.25 Comparison of experimental data and analytical calculation in master curve of storage modulus. Specimen is in series loading with volume fraction (E/F)=67/33.

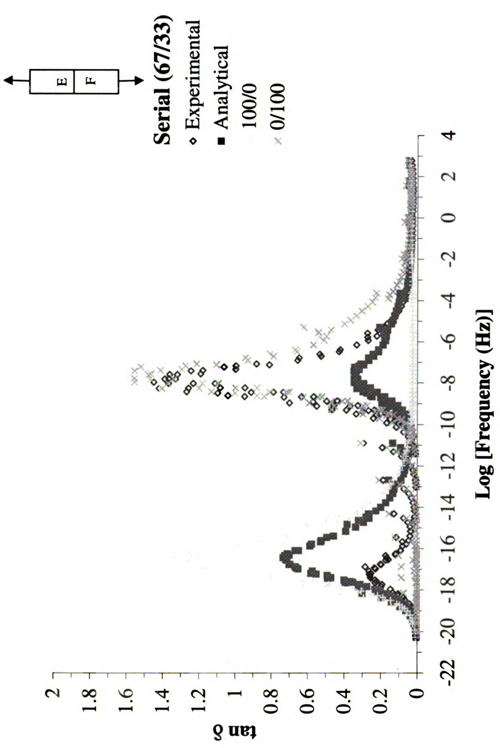

Figure 6.26 Comparison of experimental data and analytical calculation in master curve of tanδ. Specimen is in series loading with volume fraction (E/F)=67/33.

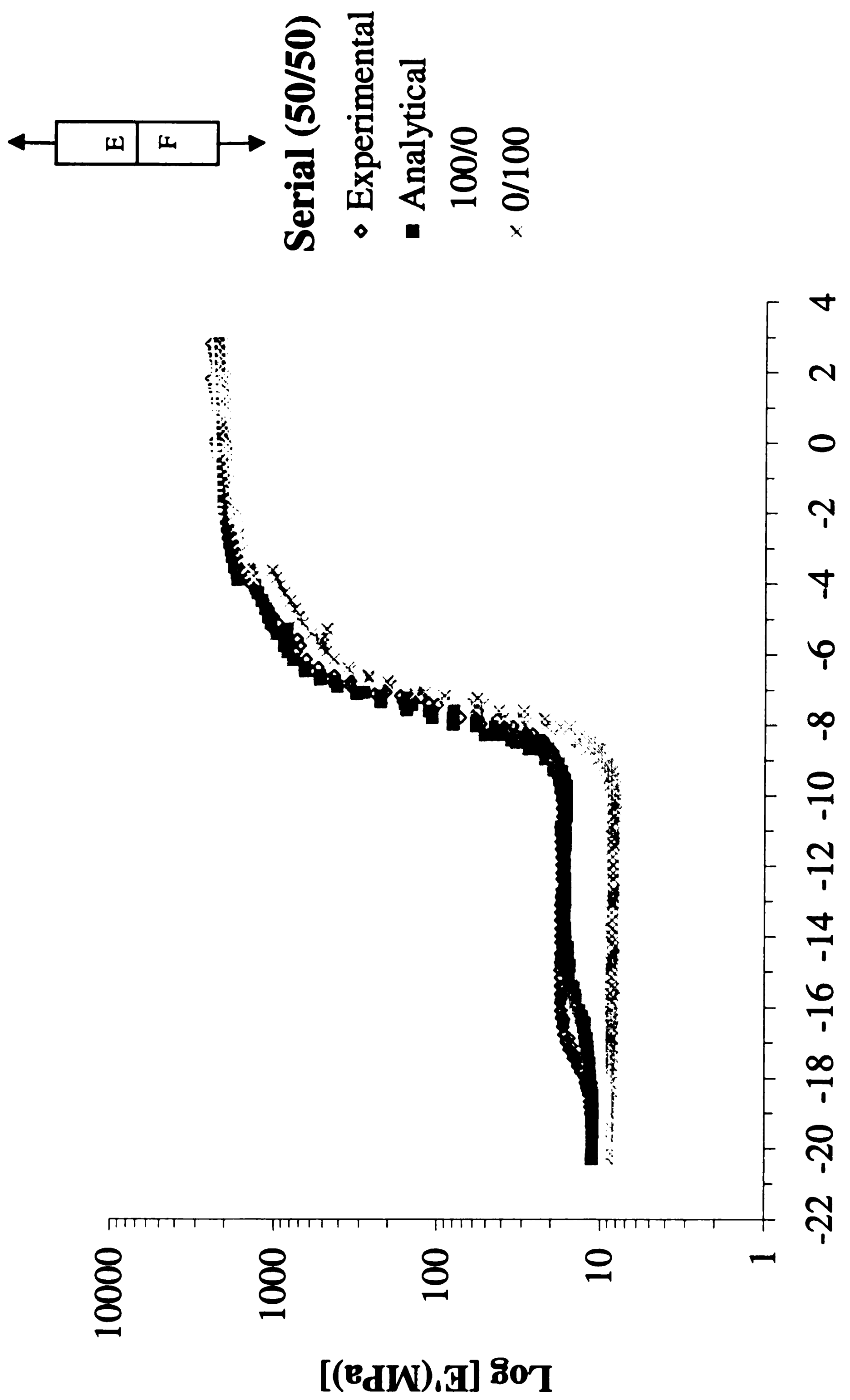

Figure 6.27 Comparison of experimental data and analytical calculation in master curve of storage modulus. Specimen is in series loading with volume fraction (E/F)=50/50.

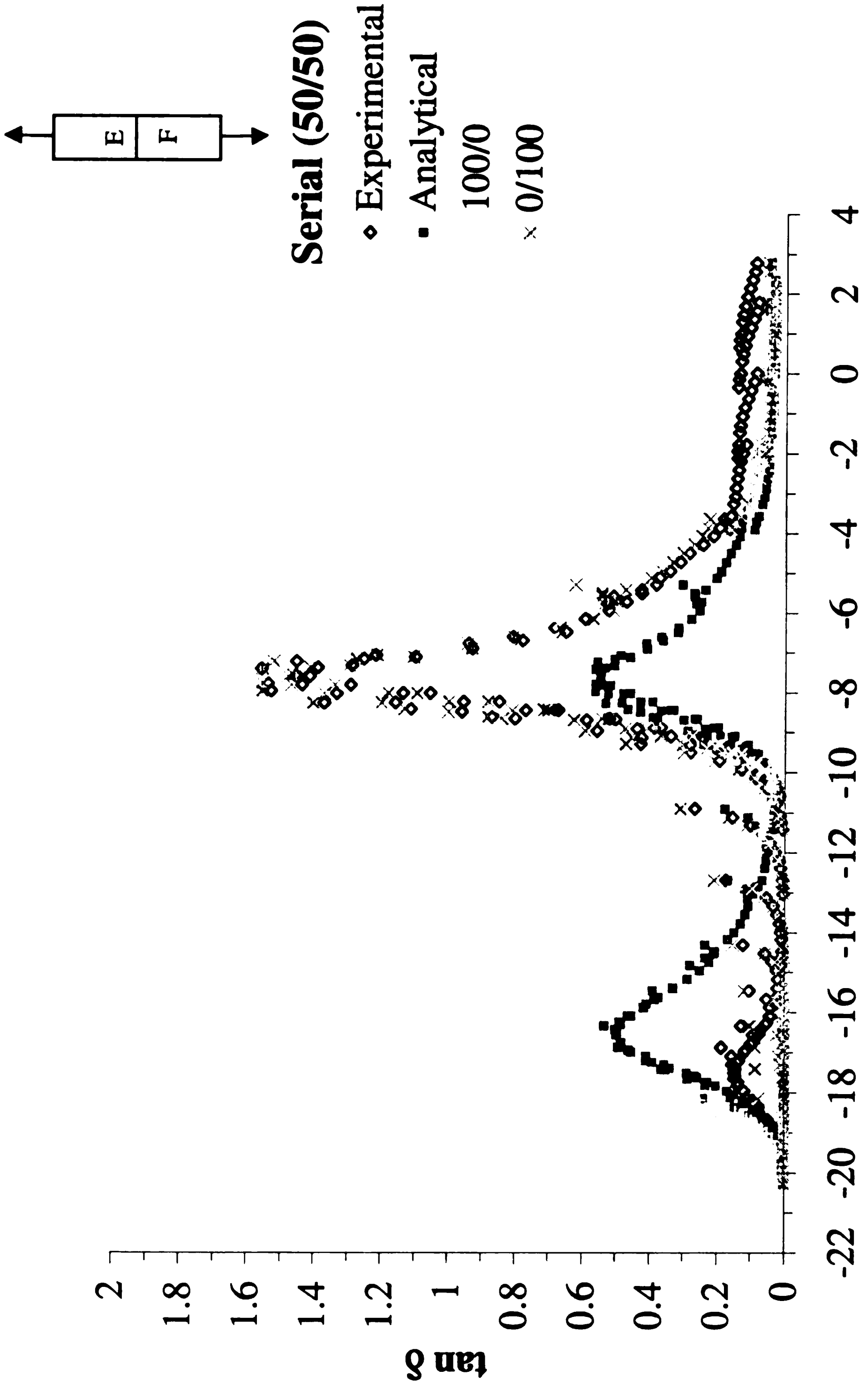

Figure 6.28 Comparison of experimental data and analytical calculation in master curve of tanδ. Specimen is in series loading with volume fraction (E/F)=50/50.

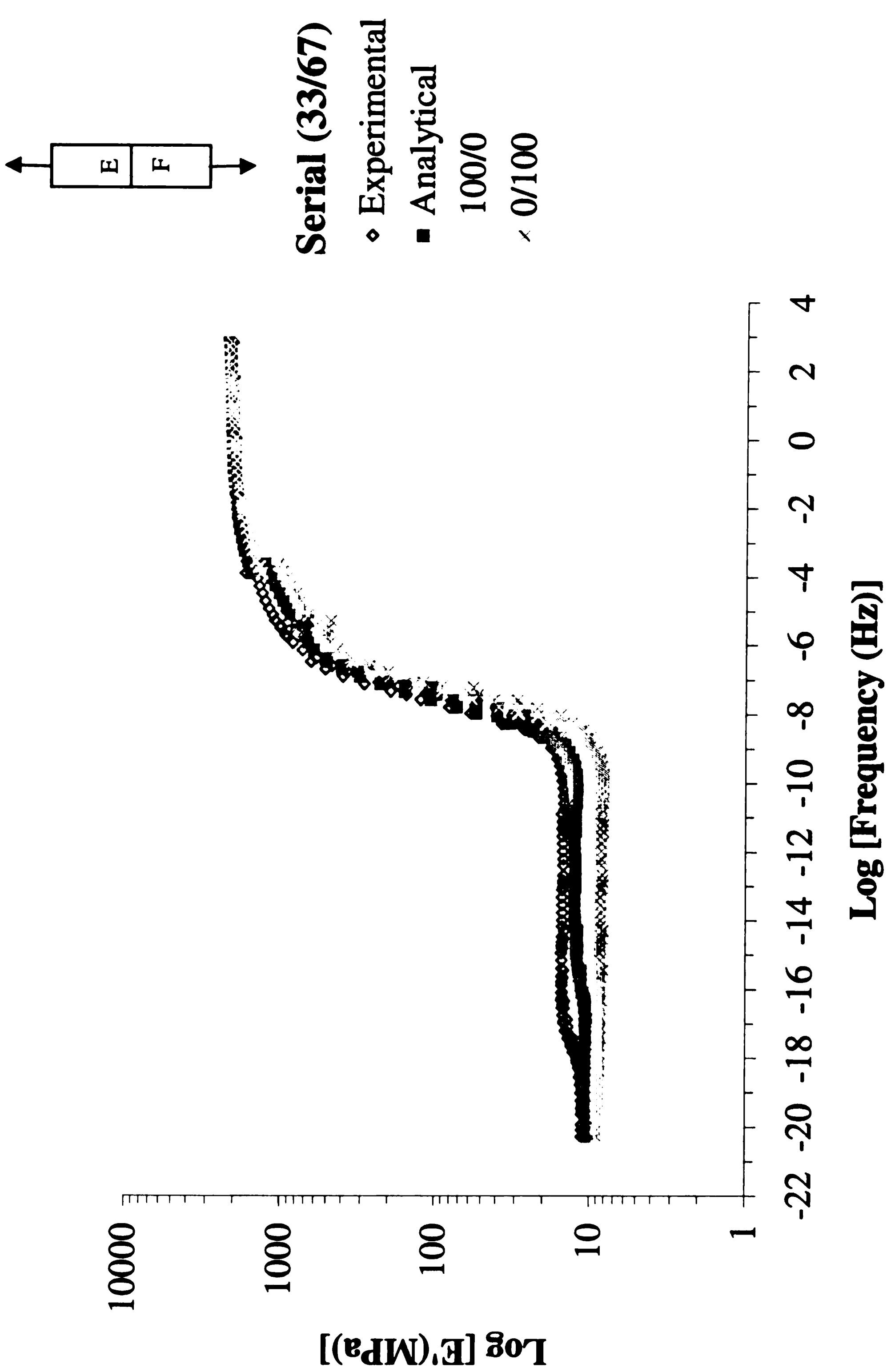

Figure 6.29 Comparison of experimental data and analytical calculation in master curve of storage modulus. Specimen is in series loading with volume fraction (E/F)=33/67.

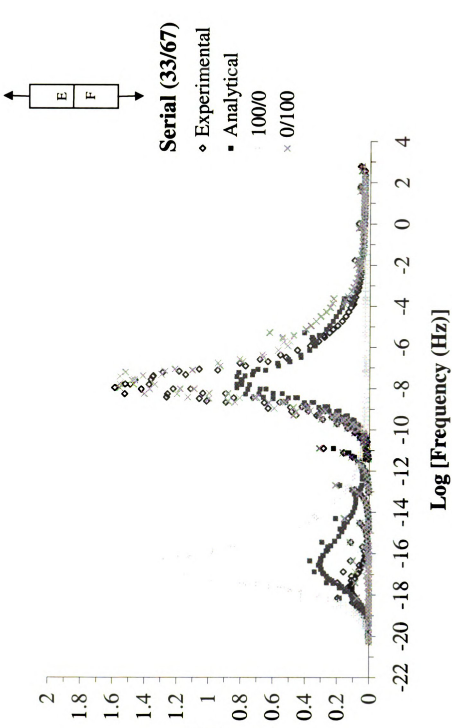

Figure 6.30 Comparison of experimental data and analytical calculation in master curve of tanδ. Specimen is in series loading with volume fraction (E/F)=33/67.

According to the strain measurement by the SEM moiré method, each component of the specimen in serial loading configuration does not undergo a constant strain experiment even though the whole specimen does. Therefore, when calculating the analytical solution for specimens in serial loading configuration, one needs to modify the rule of mixtures. Based on the previous observation from the SEM moiré method, a relaxation function must employ in the analytical calculation.

In serial loading experiments the peak position of tanδ of Material E shifts toward a lower frequency compared with that of 100 percent of Material F, which implies the viscoelastic response of Material E in two-phase polymer specimen of serial loading configuration is delayed. On the other hand, the viscoelastic response of Material F in the specimens with parallel loading configuration is accelerated.

6.5 CONCLUSIONS

The SEM moiré methods have been performed in measuring the deformation of carbon fiber reinforced composites. Based on carbonaceous grating and monitor viewing techniques (CM), a reference grating (either 2778 or 2667 lines/mm) interfered with a carbonaceous grating with a frequency of 2778 lines/mm. The angles between these two gratings were calculated from Equation 6.1 based on the measured moiré fringe angle (ϕ) and moiré fringe pitch (p_f) from observed moiré fringe patterns. A comparison of the angles measured from the SEM images taken at different angle rotations with the calculated angles from the SEM moiré CM method proves this SEM moiré CM method to be feasible. Another SEM moiré method, carbonaceous grating and total imaging (CT), also presented rotation angle measurements on composite specimens and the results were promising as shown in Figure 6.5.

The second application of the SEM moiré CM method was to measure the local strain of two-phase epoxy specimen in serial loading configuration during its stress relaxation experiment. In addition to the SEM moiré CM method, the local strain was also measured based on the SEM images of interface shifting. The measurements from these two methods were in good agreement. The shifting of the interface resulted in the changes of local strain on both Material E and F during the stress relaxation experiment, which kept the global strain constant. Some additional energy loss was expected in this two-phase polymer specimen compared with the regular 100 percent single-phase materials.

To examine this hypothesis, specimens in serial and parallel loading configurations at different volume fractions were prepared to run the frequency sweep of dynamic mechanical test at various temperatures. The experimental data were compared with the analytical calculation by the rule of mixtures. The analytical calculation in parallel loading configuration predicted the experimental data very well as shown in figures 6.17, 6.19, and 6.21. On the other hand, the experimental data from serial loading configuration was not well predicted by the rule of mixtures especially in loss modulus and tanδ. Therefore, weight functions accounting for additional energy loss due to the mismatch of viscoelastic response between Material E and F were required to employ while fitting the experimental data of specimens in serial loading configuration.

Chapter 7

CONCLUSIONS

Based on the concept of the SEM moiré, the AFM moiré method was developed. The viewing scanner of AFM as a reference grating interfered with the lithographic grating as a specimen grating resulting in moiré fringes observed in AFM. Angle rotation of two grating systems was performed to verify the feasibility of the AFM moiré method. The advantages of the AFM moiré method compared to the SEM moiré method are convenience and economy. The SEM moiré method requires a vacuum environment as well as a conductive layer to prevent charge build-up on non-conductive specimens and to avoid possible contamination to the electron gun. However, because AFM is a surface topographic technique and the target specimen is coated with lithographic grating, the AFM moiré method cannot provide microscopic measurement simultaneously with microscopic observation as can the SEM moiré method.

To simplify the grating fabrication technique and to improve the AFM moiré method, the carbonaceous grating technique was developed. Based on the contamination in SEM chamber and testing specimens, direct electron beam deposition is utilized to deposit carbonaceous grating on specimen surface as a specimen grating. This new technique reduces the multiple procedures of coating and developing in lithographic grating technique. Since the moiré fringe formation depends not only on the topographic contrast but also on the voltage contrast for this technique, the carbonaceous grating can be as thin as 4 nm. With the advantage of this reduced thickness, the AFM moiré method is able to provide microscopic measurement and observation simultaneously. Compared with the 100 nm thickness of lithographic grating, carbonaceous grating can reduce the reinforcement effect to a minimum as well.

After developing the carbonaceous grating technique and the total imaging technique, there then exist two grating-casting techniques and three fringe-viewing techniques for the SEM moiré method. With the combination of these two groups, a total of six SEM moiré methods are available. Besides the SEM moiré LM method, which is commonly used by many researchers, another five new SEM moiré methods are introduced. Based on these five new SEM moiré methods, the experimental procedures of preparing specimen grating become easier and the sensitivity of measuring deformation increases. The sensitivity of the lithographic grating and total imaging method (LT), as well as the carbonaceous grating and total imaging method (CT), truly depends on the frequency of specimen grating, which can be very high.

With these new developed techniques, the SEM moiré methods are applied to measure the deformation of carbon fiber reinforced composites and two-phase polymers. For carbon fiber reinforced composites, the carbonaceous grating and monitor viewing method (CM) as well as the carbonaceous grating and total imaging method (CT) are used to measure the angle between two gratings. The experimental measurements are in a good agreement with the analytical calculation.

For two-phase polymers, the local strain is measured by the SEM moiré CM method during the stress relaxation experiment. The interface shifting of the two-phase polymer specimen is observed under the SEM and the local strain is measured from the SEM images. The measurements from the moiré fringe patterns and the SEM images agree that the strain in each phase is not constant. Accordingly, the method to analyze the viscoelastic response of the two-phase polymer specimen requires Boltzmann superposition integral instead of quasi-elastic analysis. Based on the observation from the SEM moiré CM method, the dynamic mechanical tests are conducted to investigate the viscoelastic response of two-phase polymers. The analytical solution is derived based on the rule of mixtures. The rule of mixtures predicts the dynamic mechanical testing data of the specimens in parallel loading configuration. However, the rule of mixtures does not predict the dynamic mechanical testing data of specimens in serial loading configuration. A weight function has to be employed to allow the analytical solution to fit the experimental data in serial loading configuration.

APPENDICES

APPENDIX A

SEM SETTING PARAMETERS FOR ELECTRON BEAM LITHOGRAPHY

A CamScan 44FE scanning electron microscope was used in this study. The grating technique was based on electron beam lithography and was similar to the method presented by Attwood and Hazzledine [37]. It utilized a built-in photograph scanner with a scanning rate of 1250 lines/frame to perform a single scanning on an epoxy specimen coated with gold and PMMA. In order to achieve the desired quantity and quality for the moiré grating, the following SEM parameters were used: an acceleration voltage of 20 keV, a beam aperture of 50 μm, a spot size of 9 and a working distance of 20 mm. A potentiometer designated as C1 was set to 6.295 mV, resulting in 1.72 mA and 0.93 mA for C2 and C3 readings, respectively, to achieve an electron beam current of 1.5 nA.

The alignment and the focus of the electron beam were checked at a location away from the area of interest before performing the lithographic scanning. The electron beam was then blocked by a beam stopper before being relocated to the desired area for lithography. The specific magnification factor 360 was calculated from Equation (5.1) for the desired grating frequency, i.e. 5000 lines/mm. Based on the magnification factor, an exposure time of 21 seconds per scanning frame was found to give the right electron dosage.

APPENDIX B

COMPARISONS OF VARIOUS SEM MOIRÉ METHODS BASED ON SPECIMEN GRATING OF 5000 LINES/MM

	SEM Moiré	LM	LP	LT	CM	CP	CT
Specimen Grating (Initial and Deformed)	Scanning Rate (lines/frame)	1250	1250	1250	500	500	500
	Magnification Factor	360	360	360	900	900	900
	Scanning Area (μm x μm)	333 x 250	333 x 250	333 x 250	133 x 100	133 x 100	133 x 100
Reference Grating or Total Imaging	Scanning Rate (lines/frame)	500	1250	1250	500	1250	500
	Magnification Factor	900	360	6000*	900	360	6000*
	Viewing Area (μm x μm)	133 x 100	333 x 250	20 x 15*	133 x 100	333 x 250	20 x 15*
Minimum Strain for One Moiré Fringe		0.2%	0.08%	0.02%#	0.2%	0.08%	0.02%#

* based on a viewing magnification factor of 6000
\# based on 5000 lines/mm

APPENDIX C

LOCAL STRAIN CALCULATION OF MATERIAL E AND F IN TWO-PHASE POLYMER SPECIMEN

Here are the Symbols that used in the derivation:

σ: stress;
ε: strain;
V: volume fraction
J: creep compliance of the material
E: relaxation modulus of the material
L: Laplace transformation
superscript E and F: Material E and F
superscript p and s: parallel and serial loading configuration
subscript 0: the initial magnitude

$$\sigma^E(t) = \sigma^F(t)$$

$$\varepsilon_0^s = V^E \varepsilon^E(t) + V^F \varepsilon^F(t)$$

$$\int_0^t E^E(t-\tau)\frac{d\varepsilon^E}{d\tau}d\tau = \int_0^t E^F(t-\tau)\frac{d\varepsilon^F}{d\tau}d\tau$$

$$\varepsilon_0^s = V^E \int_0^t J^E(t-\tau)\frac{d\sigma^E}{d\tau}d\tau + V^F \int_0^t J^F(t-\tau)\frac{d\sigma^F}{d\tau}d\tau$$

$$E^E(\mathrm{s})\varepsilon^E(\mathrm{s}) = E^F(\mathrm{s})\varepsilon^F(\mathrm{s}) \Rightarrow \varepsilon^F(\mathrm{s}) = \frac{E^E(\mathrm{s})\varepsilon^E(\mathrm{s})}{E^F(\mathrm{s})}$$

$$\frac{\varepsilon_0^s}{\mathrm{s}} = V^E J^E(\mathrm{s})\sigma^E(\mathrm{s}) + V^F J^F(\mathrm{s})\sigma^F(\mathrm{s})$$

$$= V^E \varepsilon^E(\mathrm{s}) + V^F \varepsilon^F(\mathrm{s})$$

$$= V^E \varepsilon^E(\mathrm{s}) + V^F \frac{E^E(\mathrm{s})\varepsilon^E(\mathrm{s})}{E^F(\mathrm{s})}$$

$$= (V^E + V^F \frac{E^E(\mathrm{s})}{E^F(\mathrm{s})})\varepsilon^E(\mathrm{s})$$

$$\varepsilon^E(\mathrm{s}) = \frac{\varepsilon_0^s}{\mathrm{s}} * \frac{E^F(\mathrm{s})}{V^E E^F(\mathrm{s}) + V^F E^E(\mathrm{s})}$$

$$\varepsilon^E(t) = L^{-1}[\varepsilon^E(\mathrm{s})]$$

APPENDIX D

ANALYTICAL SOLUTIONS OF TWO-PHASE POLYMERS BASED ON RULE OF MIXTURE

Here are the Symbols that used in the derivation:

L: length
Δl: displacement
ε: strain
P: force
A: area
σ: stress
V: volume fraction
E^*, E', E'': complex, storage, and loss modulus of the material
superscript *E* and *F*: Material E and F
superscript *p* and *s*: parallel and serial loading configuration
subscript 0: the initial magnitude

For Material E,

$$\varepsilon^E(t) = \varepsilon_0^E e^{i\omega t}$$

$$\sigma^E(t) = \sigma_0^E e^{i(\omega t + \delta^E)}$$

$$E^{E*} = E^{E}{}' + iE^{E}{}'' = \frac{\sigma^E(t)}{\varepsilon^E(t)} = \frac{\sigma_0^E e^{i(\omega t+\delta^E)}}{\varepsilon_0^E e^{i\omega t}} = \frac{\sigma_0^E}{\varepsilon_0^E} e^{i\delta^E} = \frac{\sigma_0^E}{\varepsilon_0^E}(\cos\delta^E + i\sin\delta^E)$$

$$E^{E}{}' = \frac{\sigma_0^E}{\varepsilon_0^E}\cos\delta^E = E_0^E\cos\delta^E \Rightarrow E_0^E = \frac{E^{E}{}'}{\cos\delta^E}$$

$$E^{E}{}'' = \frac{\sigma_0^E}{\varepsilon_0^E}\sin\delta^E = E_0^E\sin\delta^E \Rightarrow E_0^E = \frac{E^{E}{}''}{\sin\delta^E}$$

For Material F,

$$\varepsilon^F(t) = \varepsilon_0^F e^{i\omega t}$$

$$\sigma^F(t) = \sigma_0^F e^{i(\omega t + \delta^F)}$$

$$E^{F*} = E^{F}{}' + iE^{F}{}'' = \frac{\sigma^F(t)}{\varepsilon^F(t)} = \frac{\sigma_0^F e^{i(\omega t+\delta^F)}}{\varepsilon_0^F e^{i\omega t}} = \frac{\sigma_0^F}{\varepsilon_0^F} e^{i\delta^F} = \frac{\sigma_0^F}{\varepsilon_0^F}(\cos\delta^F + i\sin\delta^F)$$

$$E^{F}{}' = \frac{\sigma_0^F}{\varepsilon_0^F}\cos\delta^F = E_0^F\cos\delta^F \Rightarrow E_0^F = \frac{E^{F}{}'}{\cos\delta^F}$$

$$E^{F}{}'' = \frac{\sigma_0^F}{\varepsilon_0^F}\sin\delta^F = E_0^F\sin\delta^F \Rightarrow E_0^F = \frac{E^{F}{}''}{\sin\delta^F}$$

For Material E and F in parallel configuration,

$$l_0^P = l_0^E = l_0^F, \Delta l^P e^{i\omega t} = \Delta l^E e^{i\omega t} = \Delta l^F e^{i\omega t},$$

$$\varepsilon_0^P e^{i\omega t} = \varepsilon_0^E e^{i\omega t} = \varepsilon_0^F e^{i\omega t}, \varepsilon^P(t) = \varepsilon^E(t) = \varepsilon^F(t)$$

$$P_0^E + P_0^F = P_0^P, \sigma_0^E A^E + \sigma_0^F A^F = \sigma_0^P A^P, V^E \sigma_0^E + V^F \sigma_0^F = \sigma_0^P,$$

$$\sigma^P(t) = \sigma_0^P e^{i(\omega t + \delta^P)} = (V^E \sigma_0^E + V^F \sigma_0^F) e^{i(\omega t + \delta^P)}$$

$$= V^E \sigma_0^E e^{i(\omega t + \delta^E + \delta^P - \delta^E)} + V^F \sigma_0^F e^{i(\omega t + \delta^F + \delta^P - \delta^F)}$$

$$\sigma^P(t) = V^E \sigma^E(t) e^{i(\delta^P - \delta^E)} + V^F \sigma^F(t) e^{i(\delta^P - \delta^F)}$$

$$E^{P^*} = \frac{\sigma^P(t)}{\varepsilon^P(t)} = \frac{V^E \sigma^E(t) e^{i(\delta^P - \delta^E)}}{\varepsilon^E(t)} + \frac{V^F \sigma^F(t) e^{i(\delta^P - \delta^F)}}{\varepsilon^F(t)}$$

$$= V^E [E^{E^*} e^{i(\delta^P - \delta^E)}] + V^F [E^{F^*} e^{i(\delta^P - \delta^F)}]$$

$$E^{P^*} e^{-i\delta^P} = V^E [E^{E^*} e^{-i\delta^E}] + V^F [E^{F^*} e^{-i\delta^F}],$$

$$(E^{P\prime} + iE^{P\prime\prime})(\cos\delta^P - i\sin\delta^P) = V^E (E^{E\prime} + iE^{E\prime\prime})(\cos\delta^E - i\sin\delta^E)$$

$$+ V^F (E^{F\prime} + iE^{F\prime\prime})(\cos\delta^F - i\sin\delta^F)$$

$$E^{P\prime}\cos\delta^P + E^{P\prime\prime}\sin\delta^P = V^E (E^{E\prime}\cos\delta^E + E^{E\prime\prime}\sin\delta^E)$$

$$+ V^F (E^{F\prime}\cos\delta^F + E^{F\prime\prime}\sin\delta^F)$$

$$E^{P\prime\prime}\cos\delta^P - E^{P\prime}\sin\delta^P = V^E (E^{E\prime\prime}\cos\delta^E - E^{E\prime}\sin\delta^E)$$

$$+ V^F (E^{F\prime\prime}\cos\delta^F - E^{F\prime}\sin\delta^F)$$

$$E^{P\prime} = V^E E^{E\prime} + V^F E^{F\prime}$$

$$E^{P\prime\prime} = V^E E^{E\prime\prime} + V^F E^{F\prime\prime}$$

$$\tan\delta^P = \frac{V^E E^{E\prime\prime} + V^F E^{F\prime\prime}}{V^E E^{E\prime} + V^F E^{F\prime}}$$

For Material E and F in serial loading configuration,

$$P_0^E = P_0^F = P_0^S, \sigma_0^E = \sigma_0^F = \sigma_0^S$$

$$l_0^S = l_0^E + l_0^F, \Delta l^S e^{i\omega t} = \Delta l^E e^{i\omega t} + \Delta l^F e^{i\omega t},$$

$$\varepsilon_0^S e^{i\omega t} = V^E \varepsilon_0^E e^{i\omega t} + V^F \varepsilon_0^F e^{i\omega t}, \varepsilon^S(t) = V^E \varepsilon^E(t) + V^F \varepsilon^F(t)$$

$$\sigma_0^E = \sigma_0^F = \sigma_0^S \Rightarrow \sigma_0^E e^{i(\omega t+\delta^S)} = \sigma_0^F e^{i(\omega t+\delta^S)} = \sigma_0^S e^{i(\omega t+\delta^S)}$$

$$\sigma^S(t) = \sigma_0^S e^{i(\omega t+\delta^S)} = \sigma^E(t) e^{i(\delta^S-\delta^E)} = \sigma^F(t) e^{i(\delta^S-\delta^F)}$$

$$\frac{\sigma^S(t)}{E^{S^*}} = \frac{V^E \sigma^E(t)}{E^{E*}} + \frac{V^F \sigma^F(t)}{E^{F*}},$$

$$\frac{1}{E^{S^*}} = \frac{V^E}{E^{E*} e^{i(\delta^S-\delta^E)}} + \frac{V^F}{E^{F*} e^{i(\delta^S-\delta^F)}} \Rightarrow \frac{1}{\left|E^{S^*}\right|} = \frac{V^E}{\left|E^{E*}\right|} + \frac{V^F}{\left|E^{F*}\right|}$$

$$\frac{(E^{S\prime} - iE^{S\prime\prime})(\cos\delta^S + i\sin\delta^S)}{\left|E^{S^*}\right|} = V^E \frac{(E^{E\prime} - iE^{E\prime\prime})(\cos\delta^E + i\sin\delta^E)}{\left|E^{E^*}\right|}$$

$$+ V^F \frac{(E^{F\prime} - iE^{F\prime\prime})(\cos\delta^F + i\sin\delta^F)}{\left|E^{F^*}\right|}$$

$$\frac{E^{S\prime}\cos\delta^S + E^{S\prime\prime}\sin\delta^S}{\left|E^{S^*}\right|} = V^E \frac{E^{E\prime}\cos\delta^E + E^{E\prime\prime}\sin\delta^E}{\left|E^{E^*}\right|} + V^F \frac{E^{F\prime}\cos\delta^F + E^{F\prime\prime}\sin\delta^F}{\left|E^{F^*}\right|}$$

$$\frac{E^{S\prime}\sin\delta^S - E^{S\prime\prime}\cos\delta^S}{\left|E^{S^*}\right|} = V^E \frac{E^{E\prime}\sin\delta^E - E^{E\prime\prime}\cos\delta^E}{\left|E^{E^*}\right|} + V^F \frac{E^{F\prime}\sin\delta^F - E^{F\prime\prime}\cos\delta^F}{\left|E^{F^*}\right|}$$

$$\frac{E^{S\prime}}{\left|E^{S^*}\right|} = V^E \frac{E^{E\prime}}{\left|E^{E^*}\right|} + V^F \frac{E^{F\prime}}{\left|E^{F^*}\right|}, \quad \frac{E^{S\prime\prime}}{\left|E^{S^*}\right|} = V^E \frac{E^{E\prime\prime}}{\left|E^{E^*}\right|} + V^F \frac{E^{F\prime\prime}}{\left|E^{F^*}\right|}$$

$$\tan\delta^S = \frac{E^{S\prime\prime}}{E^{S\prime}} = \frac{V^E \dfrac{E^{E\prime\prime}}{\left|E^{E^*}\right|} + V^F \dfrac{E^{F\prime\prime}}{\left|E^{F^*}\right|}}{V^E \dfrac{E^{E\prime}}{\left|E^{E^*}\right|} + V^F \dfrac{E^{F\prime}}{\left|E^{F^*}\right|}}$$

E/F-p and E/F-s in serial:

$$\frac{E^{C}{}'}{\left|E^{C^*}\right|}=V^{P}\frac{E^{P}{}'}{\left|E^{P^*}\right|}+V^{S}\frac{E^{S}{}'}{\left|E^{S^*}\right|}$$

$$\frac{E^{C}{}''}{\left|E^{C^*}\right|}=V^{P}\frac{E^{P}{}''}{\left|E^{P^*}\right|}+V^{S}\frac{E^{S}{}''}{\left|E^{S^*}\right|}$$

$$\tan\delta^{C}=\frac{E^{C}{}''}{E^{C}{}'}=\frac{V^{P}\frac{E^{P}{}''}{\left|E^{P^*}\right|}+V^{S}\frac{E^{S}{}''}{\left|E^{S^*}\right|}}{V^{P}\frac{E^{P}{}'}{\left|E^{P^*}\right|}+V^{S}\frac{E^{S}{}'}{\left|E^{S^*}\right|}}$$

E/F-p and E/F-s in parallel:

$$E^{C}{}'=V^{P}E^{P}{}'+V^{S}E^{S}{}'$$

$$E^{C}{}''=V^{P}E^{P}{}''+V^{S}E^{S}{}''$$

$$\tan\delta^{C}=\frac{V^{P}E^{P}{}''+V^{S}E^{S}{}''}{V^{P}E^{P}{}'+V^{S}E^{S}{}'}$$

REFERENCES

1. Sirkis, J. S. and Lim, T. J., "Displacement and Strain-Measurement With Automated Grid Methods," Experimental Mechanics, 31(4), 382-388, 1991.

2. Yongqi, S., Corletto, C., Bradley, W. L., and Tian, J., "Direct Measurement of Microscopic Strain Distribution Near a Crack Tip," Experimental Mechanics, 36(3), 193-198, 1996.

3. Stock, S. R., "X-ray Methods for Mapping Deformation and Damage," *Micromechanics: Experimental Techniques,* AMD-Vol. 102, ed. W. N. Sharpe, Jr., ASME, 147-162, 1989.

4. Bass, S. J., Barnett, S. J., Brown, G. T., Chew, N. G., Cullis, A. G., Pitt, A. D., and Skolnick, M. S., "Effect of Growth Temperature On the Optical, Electrical and Crystallographic Properties of Epitaxial Indium Gallium- Arsenide Grown By MOCVD in an Atmospheric-Pressure Reactor," Journal of Crystal Growth, 79(1-3), 378-385, 1986.

5. Stock, S. R., Chen, H., and Birnbaum, H. K., "The Measurement of Strain Fields by X-Ray Topographic Contour Mapping," Philosophical Magazine A: Physics of Condensed Matter Structure Defects and Mechanical Properties, 53(1), 73-86, 1986.

6. Hmelo, A. B., Bilello, J. C., Davies, S. T., and Bowen, D. K., "Micromechanisms of Cleavage Behavior for Mo, Nb, and Mo-Nb Alloy Crystals as Probed by Synchrotron Radiation Topography," *Applications of x-ray topographic methods to materials science,* ed. S. Weissmann, F. Balibar, J.-F. Petroff, , Plenum Press, 343-357, 1984.

7. Stock, S. R., Guvenilir, A., Starr, T. L., Boakes, R., Elliott, J. C., Dover, S. D., and Bowen, D. K., "Microtomography of Silicon-Nitride Silicon-Carbide Composites," Journal of Metals, 40(7), A87, 1988.

8. Elliott, J. C., Bowen, D. K., Dover, S. D., and Davies, S. T., "X-Ray Microtomography of Biological Tissues Using Laboratory and Synchrotron Sources," Biological Trace Element Research, 13, 219-227, 1987.

9. Elliott, J. C. and Dover, S. D., "X-Ray Microtomography of Bone," Metabolic Bone Disease & Related Research, 5(1), 50, 1984.

10. Elliott, J. C. and Dover, S. D., "Three-Dimensional Distribution of Mineral in Bone At a Resolution of 15 $m\mu$ Determined By X-Ray Microtomography," Metabolic Bone Disease & Related Research, 5(5), 219-221, 1984.

11. Franke, E. A., Wenzel, D. J., and Davidson, D. L., "Measurement of Microdisplacements By Machine Vision Photogrammetry (DISMAP)," Review of Scientific Instruments, 62(5), 1270-1279, 1991.

12. Davidson, S. L., Chan, K. S., and Page, R. A., "Automated High-Resolution Displacement Measurements for Deformation and Fracture Research," *Micromechanics: Experimental Techniques*, AMD; Vol. 102, ed. W. N. Sharpe, ASME, 73-87, 1989.

13. Han, B. and Post, D., "Immersion Interferometer For Microscopic moiré Interferometry," Experimental Mechanics, 32(1), 38-41, 1992.

14. Han, B., Guo, Y., Lim, C. K., and Caletka, D., "Verification of Numerical Models Used in Microelectronics Packaging Design by Interferometric Displacement Measurement Methods," Journal of Electronic Packaging, 118(3), 157-163, 1996.

15. Han, B. and Guo, Y., "Thermal Deformation Analysis of Various Electronic Packaging Products by Moiré and Microscopic Moiré Interferometry," Journal of Electronic Packaging, 117(3), 185-191, 1995.

16. Post, D., Han, B., and Ifju, P., "*High Sensitivity Moiré - Experimental Analysis for Mechanics and Materials*", Springer-Verlag, 1994.

17. Chiang, F. P., "Speckle Method With Electron-Microscopes," Experimental Mechanics, 22(5), N46-N46, 1982.

18. Chiang, F.-P., Wang, Q., and Lehman, F., "New Developments in Full Field Strain Measurements Using Speckles," *Nontraditional Methods of Sensing Stress, Strain and Damage in Materials and Structures*, STP 1318, ed. G. F. Lucas and D. A. Stubbs, ASTM, 156-169, 1997.

19. Wang, Q. and Chiang, F. P., "Experimental Characterization of Interphase Mechanical Properties of Composites," Composites Part B-Engineering, 27(2), 123-128, 1996.

20. Wang, Q. and Chiang, F.-P., "Experimental Study on Mechanical Behavior of a Single Fiber," Proceedings of Materials Research Society, Fall Meeting, Boston, MA, Nov. 27-Dec. 2, 1994.

21. Yan, X. T., Wang, Q., and Chiang, F.-P., "On Stress Singularity at the Interfacial Crack Tip - An Experimental Study," Proceedings of the American Society of Composite, 9th Technical Conference, Newark, DE, Sept. 20-22, 1036-1041, 1994.

22. Wang, Q. and Chiang, F.-P., "Micro-mechanical Behavior of Polymer Interface Reinforced with Copolymers," Proceedings of Materials Research Society, Fall Meeting, Symposium Q, Boston, MA, Nov. 27-Dec. 2, 1995.

23. Wang, Y. Y., Wang, Q., and Chiang, F.-P., "Study of Effect of Thickness on Mechanical Properties of Adhesive Materials by SIEM," Proceedings of the 18th Annual Meeting of Adhesive Society, Hilton Head, SC, Feb. 19-22, 325-327, 1995.

24. Wang, Q. and Chiang, F.-P., "Micro-buckling Behavior of Graphite/PEEK Composite," The 32nd Annual Technical Meeting of Society of Engineering Science, New Orleans, LA, Oct. 29-Nov. 2, 1995.

25. Weller, R. and Shepard, B. M., "Displacement Measurement by Mechanical Interferometry," Proceedings of Society for Experimental Stress Analysis, 6 (1), 35-38, 1948.

26. Post, D., "Optical Interference for Deformation Measurements, Classical Holographic and Moiré Interferometry," *Mechanics of Nondestructive Testing,* ed. W. W. Stinchcomb Plenum Press, 1-53, 1980.

27. McDonach, A., McKelvie, J., and Walker, C. A., "Stress-Analysis of Fibrous Composites Using Moiré Interferometry," Optics and Lasers in Engineering, 1(2), 85-105, 1980.

28. Carolan, R. A., Egashira, M., Kishimoto, S., and Shinya, N., "Effect of Grain-Boundary Sliding On the Creep Micro-Deformation of Copper," Materials Transactions, JIM, 32(1), 67-73, 1991.

29. Morimoto, Y. and Hayashi, T., "Deformation Measurement During Powder Compaction by a Scanning- Moiré Method," Experimental Mechanics, 24(2), 112-116, 1984.

30. Dally, J. W. and Read, D. T., "Electron-Beam Moiré," Experimental Mechanics, 33(4), 270-277, 1993.

31. Read, D. T. and Dally, J. W., "Local Strain Measurement by Electron Beam Moiré," Advances in Electronic Packaging, ASME, 4(1), 163-169, 1993.

32. Dally, J. W. and Read, D. T., "Micromechanics Study of The Effects of Damage on Interface Strains," Novel Experimental Techniques in Fracture Mechanics, ASME, 17(6), 1-11, 1993.

33. Read, D. T. and Dally, J. W., "Theory of Electron Beam Moiré," Journal of Research of the National Institute of Standards and Technology, 101(1), 47-61, 1996.

34. Everhart, T. E., Herzog, R.F., Chang, M.S., and DeVore, W. J., Proceedings of the 6th International Conference on X-Ray Optics and Microanalysis, eds. G. Shinoda, K. Kohra, and T. Ichinokawa, University of Tokyo Press, Toykyo, 81, 1972.

35. Morse, S., Durelli, A. J., and Sciammarella, C. A., "Geometry of Moiré Fringes in Strain Analysis," Journal of Engineering Mechanics Division, Proceedings of the American Society of Civil Engineering, 86(EM4), 105-126, 1960.

36. Cloud, G., "*Optical Methods of Engineering Analysis*", Cambridge University Press, 1994.

37. Attwood, D. G. and Hazzledine, P. M., "A Fiducial Grid for High-Resolution Metallography," Metallography, 9, 483-501, 1976.

38. Han, B., "Extension of Moiré Interferometry into the Ultra-High Sensitivity Domain," Ph. D. Dissertation Thesis, Virginia Polytechnic Institute and State University, 1991.

39. Liu, D. and Shakour, E., "Moiré Method for Simultaneous Microscopic Measurement and Observation," Proceedings of the 1999 SEM Spring Conference, Cincinnati, OH, June 7-9, 1999.

40. Smith, H. I., Chinn, S. R., and DeGraff, P. D., "Application of Moiré Techniques in Scanning-electron-beam Lithography and Microscopy," Journal of Vacuum Science Technology, 12(6), 1262-1265, 1975.

41. McCord, M. A. and Rooks, M. J., "Electron Beam Lithography," *Handbook of Microlithography, Micromachining and Microfabrication*; Vol.I, ed. P. Rai-Choudhury, SPIE, 1997.

42. Chen, H., Liu, D., and Lee, A., "Moiré in Atomic Force Microscope," Experimental Techniques, 24(1), 31-32, 2000.

43. Goldstein, J. I., Newbury, D. E., Echlin, P., Joy, D. C., Romig, A. D. J., Lyman, C. E., Fiori, C., and Lifshin, E., "*Scanning Electron Microscopy and X-ray Microanalysis*", Plenum Press, 1992.

44. Hren, J. J., "Specimen Contamination in Analytical Electron-Microscopy - Sources and Solutions," Ultramicroscopy, 3(4), 375-380, 1978.

45. Bance, U. R., Drummond, I. W., Finbow, D., Harden, E. H., and Kenway, P., "Hydrocarbon Contamination in Vacuum Dependent Scientific Instruments," Vacuum, 28(10-1), 489-496, 1978.

46. Love, G., Scott, V. D., Dennis, N. M. T., and Laurenson, L., "Sources of Contamination in Electron-Optical Equipment," Scanning, 4(1), 32-39, 1981.

47. Hirsch, P., Kassens, M., Puttmann, M., and Reimer, L., "Contamination in A Scanning Electron Microscope and the Influence of Specimen Cooling," Scanning, 16(2), 101-110, 1994.

48. Postek, M. T., "An Approach to The Reduction of Hydrocarbon Contamination in The Scanning Electron Microscope," Scanning, 18(4), 269-274, 1996.

49. Nshaninan, T., Dove, R., and Rajan, K., "In-situ Strain Analysis with High Spatial Resolution: A new Failure Inspection Tool for Integrated Circuit Applications," Engineering Failure Analysis, 3(2), 109-113, 1996.

50. Folch, A., Servat, J., Esteve, J., Tejada, J., and Seco, M., "High-vacuum Versus "Environmental" Electron Beam Deposition," Journal of Vacuum Science & Technology B, 14(4), 2609-2614, 1996.

51. Kreuzer, P., "Formation and Examination of Self-Supporting Contamination Filaments," Optik, 78(4), 158-164, 1988.

52. Parks, V. J., “Geometric Moiré,” *Handbook on Experimental Mechanics,* ed. A. S. Kobayashi, Prentice-Hall, 282-313,1987.

53. Morimoto, Y., Hayashi, T., and Wada, K., "High-Sensitivity Measurement of Strain By Moiré Interferometry," JSME International Journal Series I-Solid Mechanics Strength of Materials, 32(1), 122-127, 1989.

54. Post, D., "Moiré Interferometry - Advances and Applications," Experimental Mechanics, 31(3), 276-280, 1991.

55. Kishimoto, S., Egashira, M., Shinya, N., and Carolan, R. A., "Local Micro-Deformation Analysis by Means of Microgrid and Electron Beam Moiré Fringe Method," Proceedings of 6th International Conference on Mechanical Behavior of Materials, IV, Kyoto, Japan, 29, July - 2, August, 661-666, 1991.

56. Read, D. T. and Dally, J. W., "Electron-Beam Moiré Study of Fracture of a Glass-Fiber- Reinforced Plastic Composite," Journal of Applied Mechanics-Transactions of the ASME, 61(2), 402-409, 1994.

57. Read, D. T. and Dally, J. W., "Fatigue of Microlithographically-Patterned Freestanding Aluminum Thin-Film Under Axial Stresses," Journal of Electronic Packaging, 117(1), 1-6, 1995.

58. Read, D. T., Drexler, E., Bernard, E., Grosse, I., Benoit, J., DiTomasso, J., Holzhauer, D., P., R., and Stoklosa, M., "Thermomechanical Behavior of a High Density Polymer Overlay MCM Interconnect Structure: Experiments and Analysis," Application of Fracture Mechanics in Electronic Packaging and Materials, ASME, EEP-11/MD-64, 251-261, 1995.

59. Drexler, E. S. and Berger, J. R., "Mechanical Deformation in Conductive Adhesives As Measured with Electron-beam Moiré," Journal of Electronic Packaging, 121(2), 69-74, 1999.

60. Drexler, E. S., "Reliability of a Flip-chip Package Thermally Loaded Between-55 degrees C and 125 degrees C," Journal of Electronic Materials, 28(11), 1150-1157, 1999.

61. Bradshaw, R. D. and Brinson, L.C., "A Sign Control Method For Fitting and Intercoverting Material Functions For Linearly Viscoelastic Solids," Mechanics of Time Dependent Materials, 1, 185-108, 1997.